Durham E-Theses

Laser cooling and loading of Rb into a large period, quasi-electrostatic, optical lattice

Griffin, Paul F.

How to cite:

Use policy

Laser Cooling and Loading of Rb into A Large Period, Quasi–Electrostatic, Optical Lattice

Paul F. Griffin

A thesis submitted in partial fulfilment
of the requirements for the degree of
Doctor of Philosophy

Durham
University

Department of Physics
Durham University

October 12, 2005

Laser Cooling and Loading of Rb into A Large Period, Quasi–Electrostatic, Optical Lattice

Paul F. Griffin

Abstract

This thesis reports on the design and construction of, and results from, an optical–dipole trapping apparatus developed to confine ultracold rubidium atoms in a conservative, large period, optical–dipole trap.

An ultra–high vacuum system was designed and constructed to create a very low background pressure. A new technique of viewport construction was developed, allowing for the fabrication of economical, high–quality windows for transmission of mid–infra–red laser radiation. The construction of a magneto–optical trap (MOT) and an optical molasses, and the subsequent characterisation, are discussed.

A theory for the ac–Stark shift of atoms in a far–detuned laser field was developed. The nature of the scalar and tensorial light–shifts of the ground and first excited states of alkali atoms - the $5s^2S_{1/2}$ and $5p^2P_{3/2}$ states of Rb - has been examined. The effect of the differential light–shifts between these states on the operation of efficient laser cooling is discussed.

A quasi–electrostatic dipole trap (QUEST) was formed from 50 W of CO_2 laser power ($\lambda = 10.6~\mu$m), focussed to $< 100~\mu$m. The transfer of ultra–cold atoms from the MOT and optical molasses to the QUEST have been examined. Single beam and standing wave geometries of the QUEST have been implemented, with lifetimes of many seconds.

The theory for the ac–Stark effect due to a single laser field has been further developed to consider orthogonally polarised fields with independent wavelengths. The use of an auxiliary laser field, a Nd:YAG laser at $\lambda = 1.064~\mu$m, to enhance the number and density of atoms loaded into the QUEST has been proposed and realised.

Declaration

I confirm that no part of the material offered has previously been submitted by myself for a degree in this or any other University. Where material has been generated through joint work, the work of others has been indicated.

Paul F. Griffin
Durham, October 12, 2005

Acknowledgements

I'd like take this opportunity to recognise the the people who really helped get this project and thesis completed.

Firstly I want to thank Charles Adams, my supervisor/advisor for the opportunity to do this work, for his support and advice, for having ambitious ideas for the experiments and for giving me a lot of freedom to plan and run the experiment.

The experiment was designed and built with Simon Cox/Macleod, who I shared a lab with for 3 years. He passed on a lot of experimental experience, played some good music and a lot of bad music and has been a good friend through out. Thanks also to Kevin Weatherill who built the diode lasers for the experiments and was always available to help in the lab and for the amber fizziness of special coffee. Ifan Hughes has been a fount of experimental and theoretical knowledge and was always willing to advise and help.

Thanks too to Dave who's PhD work ran parallel to my own and so was often in the same situation as I was. Matt, for building the shutters for the diode and Nd:YAG lasers. Simon Cornish arrived in Durham just in time to give us his excellent LabVIEW code and then helped adapt it to our experiment. He also gave us the design of the digital level boxes which have become indispensable in the lab. Thanks to Robert Potvliege, for taking an interest in our experiments, for doing the polarizability calculations and for giving me an understanding of the theory of light-shifts.

Thanks to Nick and Claire for being very good friends and sharing house and home with me.

I'd really like to thank my Mom and Dad who have always supported me and are the most generous people I know.

Agus an meall is mó ar deireadh, do Jean; le grá gach lá.

Contents

List of Figures

Chapter 1

Introduction

Cold Atoms

The experimental investigation of neutral atoms has been accelerated and enhanced dramatically by the development of laser cooling techniques [1, 2, 3, 4]. The preparation of cold atomic clouds with well defined energies and spatial distributions has contributed to research in the fields of atom optics [5, 6], optical lattices [7], quantum information [8], atomic clocks [9], Bose–Einstein condensation [10, 11, 12] and degenerate–Fermi gasses [13].

Laser cooling and trapping of atoms makes use of the mechanical effects of light on atoms. Cooling arises from the absorption and spontaneous emission of light from laser beams, as was first shown in 1985 by Chu *et al.* in an optical molasses [14]. By including an inhomogeneous magnetic field trapping as well as cooling can occur, as was demonstrated in the magneto–optical trap (MOT) [15]. The MOT is the starting point for most experiments as it can provide large numbers of atoms, (10^{10}) with densities on the order of 10^{11} atoms/cm^3 and temperatures on the order of 100 μK.

Optical Dipole Traps

The optical dipole force comes from the coherent interaction of an inhomogeneous laser field with the induced atomic electric dipole moment [16, 17, 18]. This force is conservative as it does not involve spontaneous emission of light. It is the result of coherent scattering by the absorption and stimulated emission of photons in an inhomogeneous light field. The atomic energy levels are shifted by this process, a phenomenon known as the ac–Stark effect [19]. In a

semi-classical picture the laser field induces a dipole moment within the atom which results in an associated energy. The potential can be shown to be related to the atomic polarizability, α, and the electric field strength, $\mathcal{E}$ by [20]

$$V_{\text{dipole}} = -\frac{1}{2}\alpha\mathcal{E}^2 \ . \tag{1.1}$$

The polarizability is dependent on the frequency of the driving electric field and its form is dispersive, changing sign about an atomic resonance [21].

The dipole potential can be related to the experimental parameters of laser intensity, I and detuning from atomic resonance, $\Delta = \omega - \omega_0$, where ω is the laser frequency and ω_0 is the atomic resonance frequency, by approximately [18]

$$U_0 \propto \frac{I}{\Delta} \ . \tag{1.2}$$

Furthermore, the scattering of trapping lights, which ultimately results in heating of trapped atoms, scales approximately as [18]

$$\Gamma_{\text{sc}} \propto \frac{I}{\Delta^2} \ . \tag{1.3}$$

From these equations it can be seen that atoms can be trapped by a focussed, red-detuned laser beam. To have a trap of significant depth with negligible heating it is necessary to increase the intensity of the trapping laser beam and also the detuning from resonance. The first experiment on dipole trapping used a laser that was detuned by several hundred GHz to the red of the $D1$ line in Na [14]. At this detuning radiation pressure forces were still observed and scattering rates of 2600 photons/s were estimated. The first "far–off–resonance" optical dipole trap (FORT) was demonstrated in 1993 using a laser that was detuned by 63 nm from resonance [22]. Scattering rates of 10^3 photons/s were measured, resulting in heating rates of 600 μK/s. To get significant trap depths the laser had to be focussed to a spotsize of < 10 μm, limiting the number of trapped atoms to 1300 Rb atoms.

A major advancement of optical dipole trapping came about with the proposal of a CO_2 laser at $\lambda = 10.6$ μm to trap cold atoms [23]. Shortly after this proposal the same group trapped more than 10^6 Cs atoms in such a trap with estimated scattering rates of one photon per atom per 1400 s (~ 0.2 mHz) [24]. This trap used a 20 W CO_2 laser focussed to 100 μm to create a trap of volume 1.5×10^{-4} cm^3, more than five times larger than the volume in the original dipole

trapping experiment [14]. The CO_2 wavelength is so far detuned from ground state atomic transitions that such a trap has been dubbed a quasi–electrostatic trap (QUEST) [23].

In the push for lower temperatures and higher atomic densities, magnetic traps were the tool of choice in the race for Bose–Einstein condensation (BEC). However, optical dipole traps have many advantages over magnetic traps. The sample can be trapped in the absence of magnetic fields, or fields can be applied to investigate Feshbach resonances [25]. The ground state dipole potential in this regime is very similar to the static limit and does not depend on the the hyperfine states of atoms. This allows for simultaneous trapping of different states of an atom and of different atomic species [26, 27]

A feature of CO_2 optical lattices is the large lattice spacing, 5.3 μm. This has allowed observation and addressing of individual sites in such an optical lattice [28].

We have used a CO_2 laser as the basis of our trapping experiments because of the negligible heating rates due to spontaneous scattering and also due to the large lattice spacing. Such a system will be the basis for 3D lattice experiments, which will allow 3D arrays of atomic samples. Each lattice site will be independent of other sites and will be addressable in 3D, providing a possible quantum register.

The experiments in this thesis were devised to examine the loading of ultra–cold Rb atoms into a 1D lattice. Due to the ac–Stark effect the atomic energy states used for laser cooling are shifted down in energy. The polarizability of the upper laser cooling state is 2.6 times larger than that of the ground state, resulting in reduced efficiency in loading of the optical lattice. A theoretical understanding of these differential light–shifts was developed from time–dependent perturbation theory.

By using an auxiliary laser field at a different wavelength the differential light–shifts of the ground and excited states can be tuned, as a result to the frequency dependence of the atomic polarizability. Using this 'light–shift engineering' we have demonstrated enhanced loading of an optical lattice. Furthermore, using this technique we have selectively loaded specific regions of an optical molasses. We have developed the theoretical basis of the ac–Stark effect to include the tensor components of the polarizability [29].

1.1 Thesis Layout

As will be made clear in this thesis, in order to trap atoms in a CO_2 laser, optical dipole trap either laser intensities on the order of 10^{11} W cm^{-2} are required or the atoms must first be pre–cooled to the μK regime. In the experiments described here we have gone for the latter option. In this thesis the design and construction of an experiment to examine the loading of atoms cooled to the micro–Kelvin regime into a CO_2 laser, optical dipole trap will be outlined. Some of the techniques used have been further developed during the course of this project, and will be presented in some detail. In the course of these experiments the ac–Stark effect of the states involved in laser cooling was examined. A technique was developed to control the relative light–shifts of the ground and excited states.

The design and operation of efficient extended cavity diode lasers (ECDLs) is discussed in Chapter 2. This section will also cover the stabilisation of the laser frequency to ~ 1 MHz.

In Chapter 3 the ultra high vacuum (UHV) apparatus will be described. The design and development of novel vacuum viewports will be examined in detail.

A MOT was created from the tools characterised in the previous chapters. The techniques of laser cooling are briefly examined and the experimental implementation outlined in Chapter 4 as will the development of a new method of providing a vapour of alkali metal atoms for the experiment.

The interfacing with the experiment is described in Chapter 5. This chapter details the computer control of the experiment and acquisition of CCD camera images.

In Chapter 6 the theory of the ac–Stark shift is developed via time–dependent perturbation methods. The experimental considerations and realisation are described in Chapters 7 and 8.

The situation of perturbing laser fields of different wavelengths is developed in Chapter 9 and the experimental results are presented in Chapter 10.

Finally, some conclusions and future directions of CO_2 optical lattice experiments are discussed in Chapter 11.

Chapter 2

Lasers and Laser Stabilisation

2.1 Introduction

The use of diode lasers has become commonplace in atomic physics [30, 31, 32]. As the field has advanced rapidly, [4], it has become more important to have laser systems that are highly stable and capable of remaining 'locked' to a particular spectral line for long periods. A general requirement is to stabilise the lasers to less than the atomic linewidths, Γ [33], which for the alkalis is of the order of 10 MHz (6 MHz for ^{85}Rb). Although an extended cavity diode laser (ECDL) can have a short-term stability of less than 1 MHz, it can drift over 100 MHz in a few minutes due to thermal fluctuations [34]. To prevent this drift the lasers can be stabilised by referencing to a narrow spectroscopy signal, e.g. saturation absorption spectroscopy [30, 35].

Chen *et al.*, [36] examined the number of atoms trapped, and optimal trapping conditions of ^{87}Rb with lasers of linewidth 10 MHz and 1 MHz. The overall effect of the increase of the linewidth by an order of magnitude was a reduction in the trapped number by 40 percent, while still trapping more than 10^7 atoms. This shows that by careful frequency stabilisation of the laser the number of trapped atoms can be significantly increased and fluctuations in the number of trapped atoms supressed. A further argument for frequency stabilisation is to keep the lasers on the desired frequency for as long as possible. This means that there can be confidence in the repeatability of experiments and reduces the amount of time spent tuning lasers.

2.2 Extended Cavity Diode Lasers (ECDLs)

Free running diode lasers have linewidths of up to 100 MHz and drift in frequency due to thermal vibrations and changes in the operating parameters of the diode, such as noise in the driving current. Tuning of the frequency is achieved mainly through the temperature of the diode, and to a lesser degree the driving current. However this tuning is a hit–an–miss affair that varies very much between different laser diodes. The output wavelength shows discrete jumps, on the order of 0.35 nm ($\sim$ 100 GHz at 780 nm) with varying temperature due to mode hops in the laser cavity. See Wieman *et al.* for an excellent review of the use of diode lasers in atomic physics [37].

Diode lasers are very susceptible to optical feedback, a technique that can be used to create a tunable, narrow–linewidth laser source. A frequency dependent reflector - e.g. a diffraction grating - provides such a method of feedback while still coupling out a significant amount of laser power. In the 'Littrow' geometry a blazed grating diffracts the low power first order laser beam back into the laser diode cavity, with the zeroth order being outcoupled. This, and similar schemes are what are know as ECDLs. The external cavity allows the selection of a single mode of the diode chip. This simple set–up causes narrowing of the laser linewidth by two orders of magnitude and also allows tuning of the operating wavelength [30, 31].

To counteract the effect of mechanical vibrations and temperature fluctuations some kind of active stabilisation is required. In the ECDL scheme a grating is used to select a frequency, through the first diffracted order, and to feed this back into the diode laser cavity. This technique reduces the linewidth of the laser to <1 MHz. The zeroth order diffracted beam is then used as the laser output. The increased cavity length is a factor in the reduction of the linewidth. Adjustment of the angle of the grating with a piezo–electric actuator provides a mechanism for the feedback to the laser - if the laser frequency is lower than required, the angle of the grating can be increased or correspondingly opposite.

The temperature control of the laser and extended cavity determines the quality of the long term stability of the laser, i.e., how repeatable the performance of the laser is over the days, weeks and months that a experiment is in use. Temperature changes will cause changes in the cavity lengths of the diode and

the ECDL, which drastically affect the mode. For this reason the diode and external cavity must be actively temperature stabilised.

Experimentalists using Rb have the lucky advantage of having the cooling transition at 780 nm being virtually the same as the wavelength used in CD players [38]. Consequently considerable research has been conducted into the development of low cost and high power laser diodes in this spectral region. For example, it is now possible to buy a single 120 mW diode (Sharp GH0781JA2C) for less than £14 [39], or equivalent to less than £155/Watt.

2.3 Details of ECDLs

The lasers used in Durham atomic labs are based on the Littrow configuration [30, 31]. The laser diode (Sharp GH0781JA2C) and a collimating lens (f = 4.5 mm) are contained within a collimating tube (Thorlabs LT230P-B), giving good alignment of these optical components. The collimation tube is clamped into an aluminium mount which acts as a thermal reservoir for the laser diode. A gold–coated, holographic diffraction grating with 1800 lines/mm is used for frequency selective feedback. These gratings, from Richardson Grating Laboratory are used as they diffract less from the zeroth order and so can out–couple up to 85% of power out from the diode. The grating is mounted at 45° relative to the laser beam upon two piezo-electric actuators (Thorlabs AE0203D04) which are glued to another aluminium mount which is clamped in an adjustable mirror mount (Thorlabs KC1). The mirror mount allows for accurate alignment of the feedback into the laser diode. The entire external cavity is mounted inside an aluminium insulating box which is screwed to the brass base plate. The box is then mounted upon a heavy foam base to reduce vibration and then placed inside a second larger box. Anti-reflection coated windows are glued into both boxes to allow the laser beam to exit. The two boxes isolate the laser and extended cavity from air movement and temperature changes in the lab.

A Peltier cooler is in thermal contact with the collimating tube clamp. A second, larger cooler situated beneath the base plate to control the cavity temperature. Two 10 kΩ thermistors, mounted above the laser diode and between the Peltier

coolers, are connected to separate temperature controllers (Wavelength electronics TEC5000). By this arrangement the temperature of the laser diode and the cavity are actively controlled to 25°C and 24°C respectively. Previously we had kept the coolers at 19°C, approximately room temperature, but found that changes in the temperature of the lab above the set-point temperature of the laser diode caused run-away heating of the diode. This was due to the trapping of the heat generated by the Peltiers in keeping the laser diode cool within the two insulating boxes. Keeping the laser diode and cavity above the temperature range of the lab has proved to eliminate the problem.

2.4   Spectroscopy and Laser Stabilisation

In a history of hydrogen, Rigden writes, "The experiments themselves – saturation spectroscopy, polarization spectroscopy ... – were magnificent in their design and execution." [40].

2.4.1   Introduction

A considerable amount of time has been spent within the Durham group in stabilising the lasers used in our cold atom experiments. The goals of these stabilisation experiments were to have an accuracy as high as possible on an atomic transition line centre, to increase the precision and reduce the linewidth as much as possible (generally sub MHz), to have a very stable 'lock', and to have a repeatable response to the previous points. Another feature that is very desirable is ease of use when the technique is used in a full, cold atom experiment. Various methods of stabilising diode lasers to a frequency have been examined: dither locking through current modulation, dither locking through AOM modulation, level locking against Doppler broadened hyperfine features, dichroic atomic vapour laser locking (DAVLL) [41] and polarisation spectroscopy [42]. Only the latter was used in these experiments so only this will be described in detail here. However, for interest we compare the methods in terms of the goals listed above and also experimental complexity.

Comparison of Locking Methods

All of the methods for locking lasers have advantages in one of optical simplicity, electronic simplicity, accuracy, precision or robustness. Firstly we compare the methods as regards accuracy, precision and the recapture range - the frequency range over which the laser will return to the lock point if the laser is disturbed.

Name	Accuracy	Precision	Recapture Range
Dither Locking	< 1 MHz	≤ 1 MHz	Small, ≈ 50 MHz
DAVLL	≈ 250 MHz	≈ 1 MHz	Very large, ≈ 1 GHz
Level Locking	≈ 100 MHz	≈ 1 MHz	< 10 MHz
Polarisation Spectroscopy	≈ 2 MHz	< 1 MHz	≈ 100 MHz

Table 2.1: Comparison of the most common laser locking methods in terms of the accuracy and precision of the locking frequency and also the recapture range.

The values in Table. 2.1 have been measured within the group. The table shows that polarisation spectroscopy is a precise technique that does not appear to compromise on other desirable characteristics.

The other consideration to be looked at is ease of implementation, and optical and electronic complexity. The main optical component required is the reference vapour cell, which is essential for all locking schemes. However a setup such as DAVLL requires an additional vapour cell for saturation absorption spectroscopy as the features it measures are GHz wide and the accuracy is low, as indicated in Table 2.2. The techniques all require essentially identical circuitry for feedback to the laser.

2.4.2 Basic Principles of Polarisation Spectroscopy

Polarisation spectroscopy was proposed and demonstrated by Wieman and Hänsch as an advancement on saturation absorption spectroscopy. The use of polarisation spectroscopy to stabilise an ECDL has been described previously [43]. This work has been further advanced to create a technique for frequency stabilising ECDLs on a zero–crossing of an error signal without modulation of the laser frequency [42].

Name	Optics Required	Electronics Required
Dither Locking (Current)	1× Vapour cell	1 × Photodiode Lock-in amplifier Current modulator
Dither Locking (AOM)	1× Vapour cell AOM	1 × Photodiode Lock-in amplifier
DAVLL	2× Vapour cell Magnets	2 × Photodiodes Differencing circuit
Level Locking	1× Vapour cell	1 × Photodiode
Polarisation Spectroscopy	1× Vapour cell	2 × Photodiodes Differencing circuit

Table 2.2: Comparison of the additional optical and electronic components, aside from standard mirrors and lenses, required for standard laser locking methods.

Polarisation spectroscopy is method of high resolution spectroscopy, similar to saturation absorption spectroscopy [30, 35] in many ways. The medium is pumped and probed with two beams created from the same laser, with the pump beam more intense than the probe. See Fig. 2.1 for experimental setup. The differences between the spectroscopic methods are in the pumping and probing mechanisms. The theory concerning polarisation spectroscopy is examined in depth in [35, 42, 44, 45]
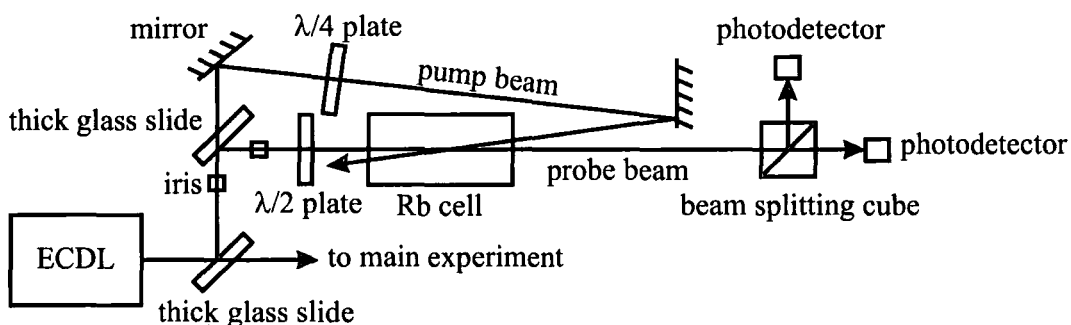
Figure 2.1: Schematic for polarisation spectroscopy based spectrometer.

2.4.3 Model of Polarisation Spectroscopy

Consider a circularly polarised, σ^+ laser beam passing through an atomic gas sample. If the beam is resonant with a particular transition of the atom then the atoms will be optically pumped towards increasing m_F, following from the selection rule that $\sigma^\pm$ light causes $\Delta m_F = \pm 1$ transitions. This pumping will cause a nonuniform population of different Zeeman levels. A linearly polarised probe beam will observe any anisotropy of the medium as a birefringence, due to differential absorption of orthogonal components of the probe beam. This birefringence will be observed in a rotation of the plane of polarisation.

2.4.4 Experimental Implementation

The probe and pump beams are taken from the same laser with intensities of $1.2 \ \mathrm{mW/cm^2}$ and $3.6 \ \mathrm{mW/cm^2}$, respectively, typically used. The probe beam is arranged so that it is linearly polarised, if necessary using a linear polariser. In general this is not required as the beam emitted by the ECDL is already linearly polarised. We arrange that the plane of polarisation is at $\pi/4$ to the horizontal using a half-wave plate. The probe beam is analysed by passing it through a polarising beam splitting (PBS) cube which separates the beam into its linear horizontal and vertical components. Each of these components is detected by a separate photodiode. A good check that the angle of the polarisation is at $\pi/4$ is to ensure that the intensities coming from the PBS are identical. It is to be noted that linearly polarised light can be considered as a combination of left- and right-circularly polarised light, with the angle of the plane of linear polarisation being a function of the relative phases of the circular components. The pump beam is passed through a $\lambda/4$ waveplate so that it is circularly polarised when it pumps the medium.

The circularly polarised light will induce σ^- or σ^+ transitions in the absorbing atoms; i.e., it will cause changes in the magnetic sub-levels of the atom of $\Delta m_F = -1$ and $\Delta m_F = +1$ respectively. The type of transition caused will depend on the polarisation of the beam relative to external magnetic fields. The circularly polarised light will cause saturation of some transitions within the atoms, and can pump some of the atoms into states that are dark to the pumping

light if these states are available. The net result is that the medium now has a non-uniform population in the different magnetic sub-levels. The medium will now absorb the σ^+ and the σ^- components of the probe beam differently. Thus one of the components will emerge retarded and with a different relative phase to the other circular component as it had when it entered the medium. The effect is for the plane of polarisation of the probe beam to be rotated. This will be observed by an increase of intensity in one of the photodiodes analysing the resolved components of the probe beam and a corresponding decrease in the other. The differential absorption of the orthogonal circularly polarised components of the probe beam is observed by inserting a $\lambda/4$ waveplate before the analysing PBS. The result can be seen in Fig. 2.2, which clearly shows the significant enhancement and decrease of absorption about the closed transition.

Fig. 2.3 (top and middle) show saturated absorption and polarisation spectra recorded simultaneously on a single frequency scan for ^{87}Rb and ^{85}Rb cooling transitions. The signal produced for Fig. 2.3 (middle) used the set-up show in Fig. 2.1 with an angle of 5.5 mrad between the pump and probe beams. In our set-up this requires a distance of over half a metre between the vapour
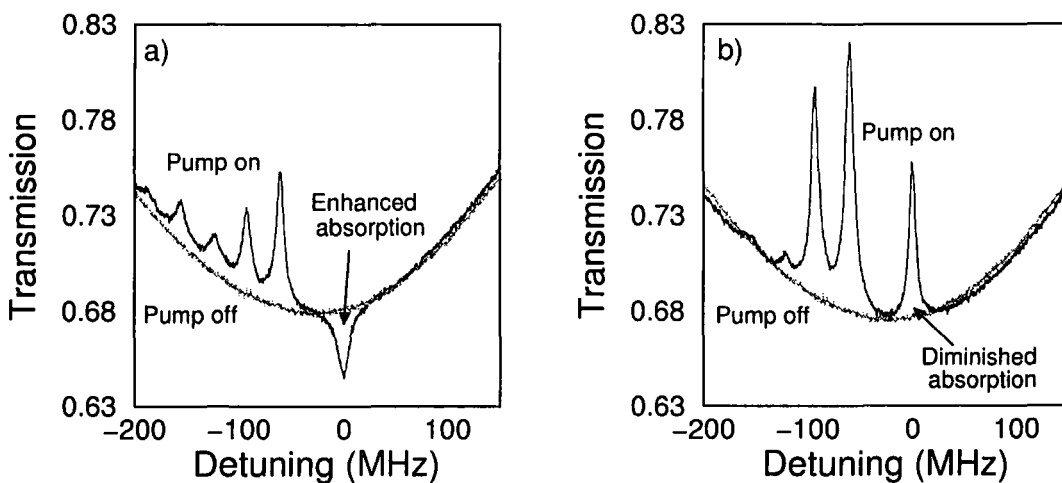
Figure 2.2: Polarisation spectra with a quarter-wave plate before the analysing PBS. (a) Absorption profile for the component of the probe driving σ^- transitions, showing a enhanced absorption in the region of the closed transition.(b) Absorption profile for the component of the probe driving σ^+ transitions, showing a decreased absorption in the region of the closed transition.
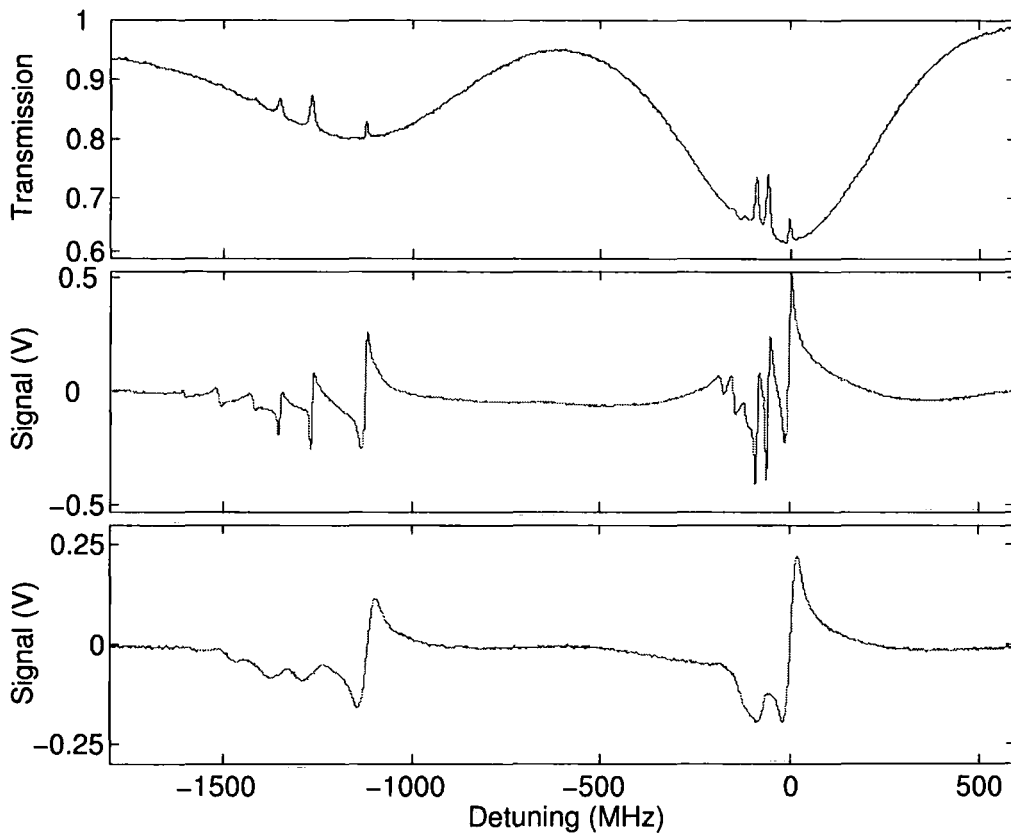
Figure 2.3: Saturated absorption (**top**) and polarisation (**middle, bottom**) spectra of, from left to right, the ^{87}Rb, $F = 2 \rightarrow F'$ and the ^{85}Rb, $F = 3 \rightarrow F'$ features recorded on a single frequency scan. **top**) and **middle**): Pump and probe were counter-propagating at an angle of ≈ 5 mrad and with intensities of 3.6 mW/cm^2 and 1.2 mW/cm^2 respectively. **bottom**) Same setup but with pump and probe were counter-propagating at an angle of 72.5 mrad.

cell and the mirror to reflect the pump beam through the vapour cell. This is not an ideal experimental situation. Furthermore, the signal produced has a number of zero crossings in the region of the transitions indicated. Further signals were taken using a larger angle of 72.5 mrad. which has the effect of Doppler broadening the signals, as can be observed in Fig. 2.3 (bottom). The signals produced have much fewer zero crossings than with the small angle set-up or than from error signals produced with from a dither and a phase sensitive detector. The effect of increasing the angle between pump and probe beams is illustrated in Fig. 2.4 as the angle is increased by a factor of two. The reduced resolution of features can be seen in in both this figure and Fig. 2.3, as is the

decrease in signal height.

2.4.5 Magnetic Sensitivity of Polarisation Spectroscopy

The effect of a cancelling magnetic fields about the vapour cell was examined by placing the cell within a Mu–metal shield. Careful positioning of the cell within the shield was found to remove a non–linear background offset, Fig. 2.5. The figure shows that the magnetic shield decreases the size of the observed signals, whereas previously Pearman had measured increased signals with a shield [44]. In general it was found that slight changes in the Mu–metal shield position caused the observed signal to change. Also, the shield is inconvenient to use as it is bulky.

A pair of coils were used to produce a bias field along the vapour cell. The coils were approximately 5 cm in diameter and separated by approximately 8 cm. The coils produced a maximum B–field of 1.3 G at the centre of the vapour cell. This longitudinal bias field caused the polarisation spectroscopy
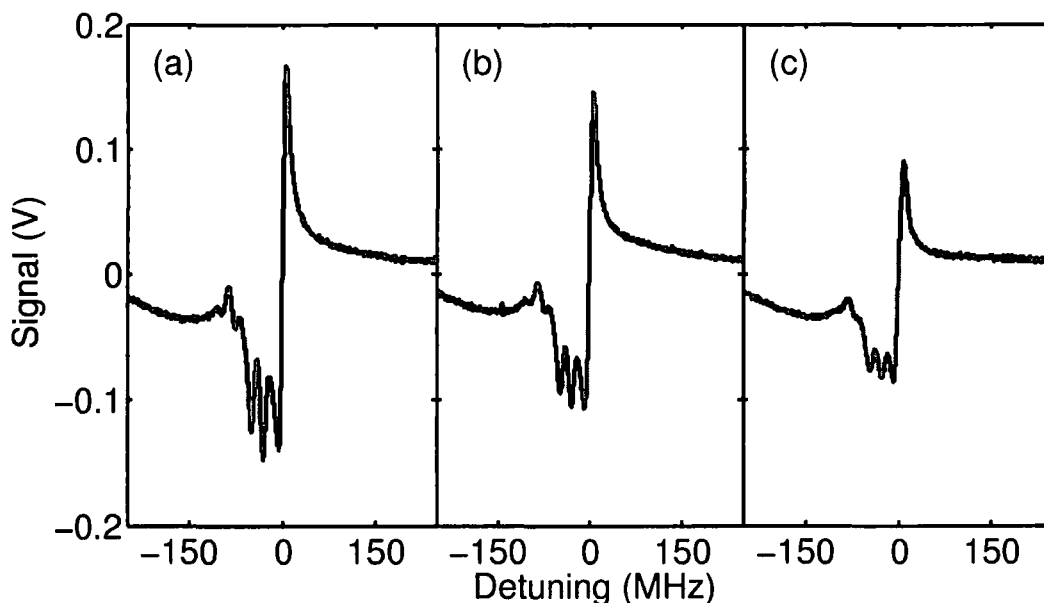
Figure 2.4: Effect of increasing the pump–probe angle in the polarisation spectroscopy setup. The spectrum is that of the ^{85}Rb $F = 3 \rightarrow F'$ transition. The angles and peak–to–peak signals are, **a)** 37 mrad, 320 mV, **b)** 58 mrad, 262 mV, **c)** 80 mrad, 170 mV.
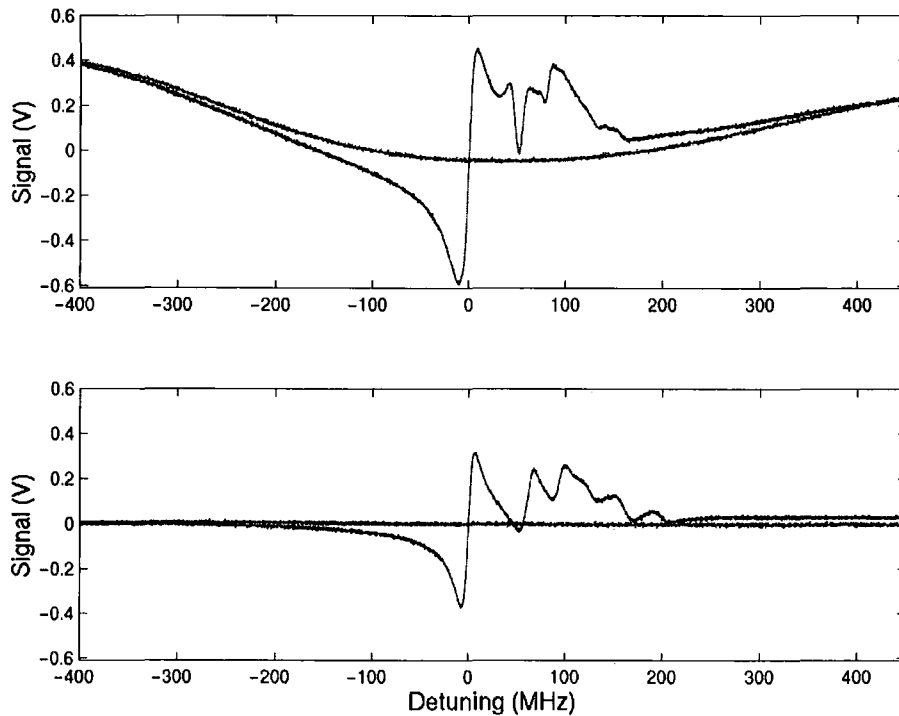
Figure 2.5: Spectra taken with (**bottom**) and without (**top**) a Mu–metal magnetic shield about the vapour cell in polarisation spectroscopy. The figures show spectra with and without the pump beam.

features to increase in size. Fig. 2.6 shows this increase as observed on the ^{85}Rb $F = 3 \rightarrow F' = 4$ feature.

For laser locking it is essential to know to what frequency the laser is being locked. Increasing the bias B-field also changs the position of the features. To monitor this effect a separate saturation absorption spectroscopy setup was added to monitor the position of the features that were to be locked to. The position of the zero–crossing initially varies quickly with varying bias B-field up to approximately 0.2 G, as shown in Fig. 2.7. The offset from 'true' line centre is actually decreased up to this point. These results agree with measured spectra of calcium taken over a greater B–field range [46].

In the setup the position of the bias coils was well defined by the vapour cell. Small changes in the position of the coils were not observed to have an effect on the spectroscopy signals produced. The offset of the zero crossing was monitored
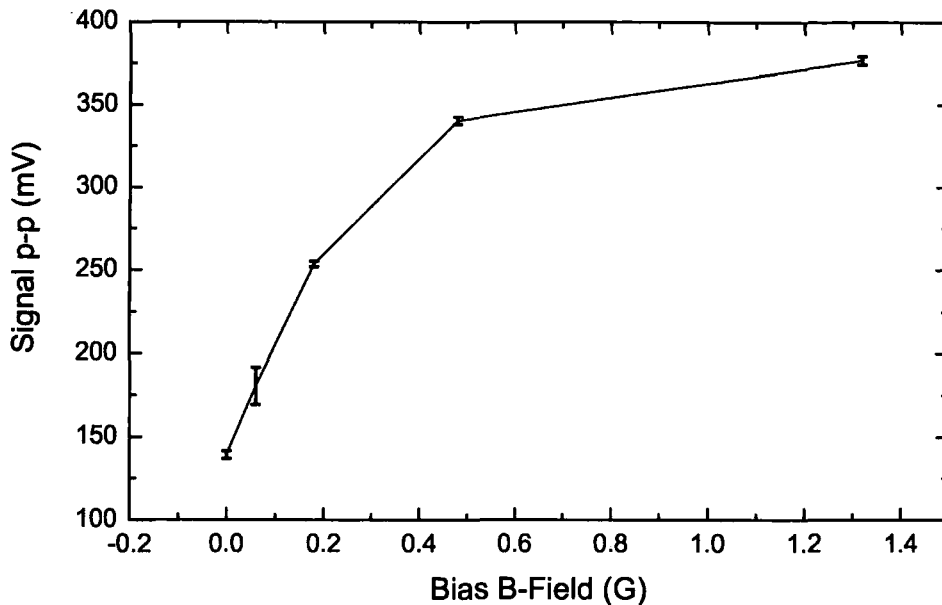
Figure 2.6: Plot of the variation of the peak–to–peak signal on the ^{85}Rb $F = 3 \rightarrow F' = 4$ polarisation spectroscopy feature with increasing longitudinal, bias B-field. A field of 1.3 G causes a signal increase by a factor of 2.7

regularly but was not found to drift over days or months.

2.4.6 Locking with Polarisation Spectroscopy

An integrator circuit based on that of Rovera *et al.* [47] was used, Fig. 2.8. Following the integrator section a DC bias voltage was added. This was to bring the voltage on a gross scale to the voltage corresponding to the required locking point. The output from the adder was connected to the piezo and also to the oscilloscope to monitor the feedback signal.

The laser was locked as follows: the laser current and the piezo scan were adjusted until the required transitions were observed in the saturation absorption spectrum. The zero-crossing of the polarisation spectroscopy difference signal was observed and the corresponding piezo voltage was recorded. The piezo was disconnected from the signal generator and connected to the output of the locking circuit, ensuring that the 'Lock' was set so that the integrator acted as a
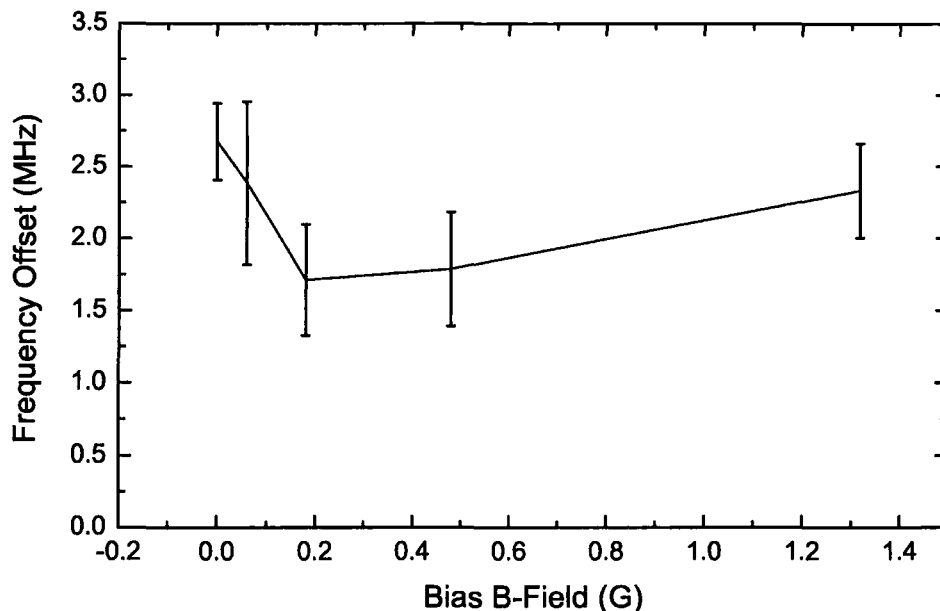
Figure 2.7: Plot of the variation of the zero crossing of the ^{85}Rb $F = 3 \rightarrow F' = 4$ polarisation spectroscopy feature with increasing longitudinal, bias B–field. The error bars are due to uncertainty in defining the line center in the reference saturation spectroscopy.

voltage follower. The recorded piezo voltage was added on at the DC bias stage and was fine tuned so that the saturation spectroscopy signal was observed to follow the pattern of the hyperfine transitions in the region required and the difference signal was seen to move as expected and to move to its zero crossing. The 'Lock' switch was then used and the gain adjusted until oscillation was observed. The gain was then reduced, indicating a lock with a large gain but below the oscillation threshold. External disturbances, such as loud noise (provided by a radio that was tuned to the noise between stations) and striking of the table caused oscillations in the feedback signal which died quickly when the disturbance was removed. The laser was then observed to remain on resonance.
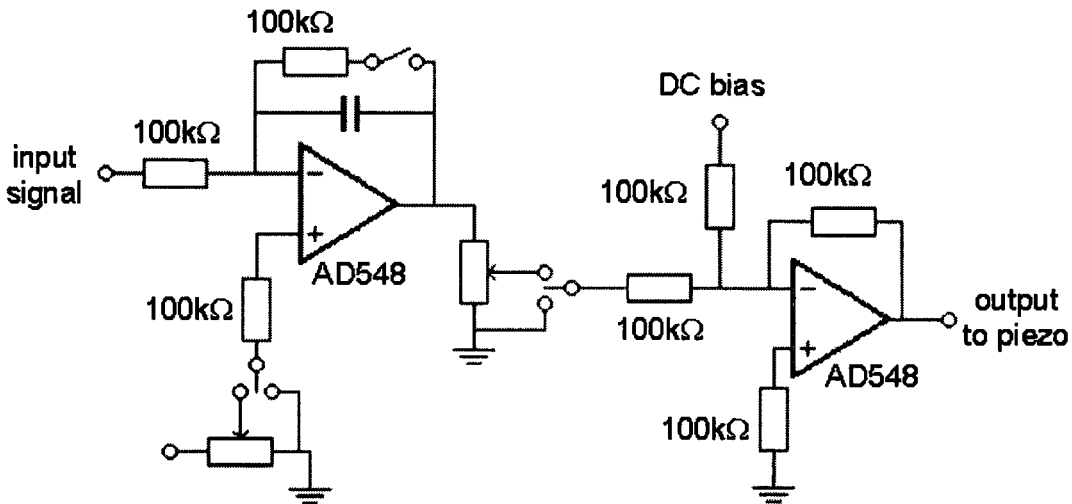
Figure 2.8: Circuit used to lock the laser. All resistors used are 100 kΩ. The capacitor used is 0.1 μF. The op-amps are AD-548. The trimmers are 1kΩ. The switches across the integrator and linking the integrator and adder are synchronous.

2.5 Frequency Stability and Beat Measurements

The trapping and hyperfine repumping lasers have been locked without interruption for days using polarisation spectroscopy, limited only by the lifetime of the batteries in the photodiode circuits.

To monitor the frequency stability of the locking scheme, the trapping and repumping lasers were both locked to the ^{85}Rb, $F = 3 \rightarrow F' = 4$ feature using polarisation spectroscopy and feedback to the grating piezo. A frequency offset of ~ 5 MHz was introduced between the lasers by using the $\lambda/2$ waveplate (see Fig. 2.1) to shift the zero of the error signal on one of the lasers. The beams were combined on a 50/50 beam–splitter and then focussed onto a photodiode. The photodiode, a Siemens BPX-65, has a quoted frequency response of up to 100 MHz when used with a 50 Ω resistor. The data were recorded on an 300 MHz bandwidth oscilloscope, terminated at 50 Ω for impedance matching.

If each laser is well described by a Lorentzian frequency line shape then the combined line shape should be also be described as a Lorentzian. The FFT of the beat signal was fitted with back–to–back exponentials as the Fourier

transform of a Lorentzian is an exponential, Fig. 2.9. The full–width–half–maximum (FWHM) was estimated as 625 kHz. If we assume that both lasers have similar, though un–correlated linewidths we then estimate the individual laser linewidths as $\sim$ 310 kHz.
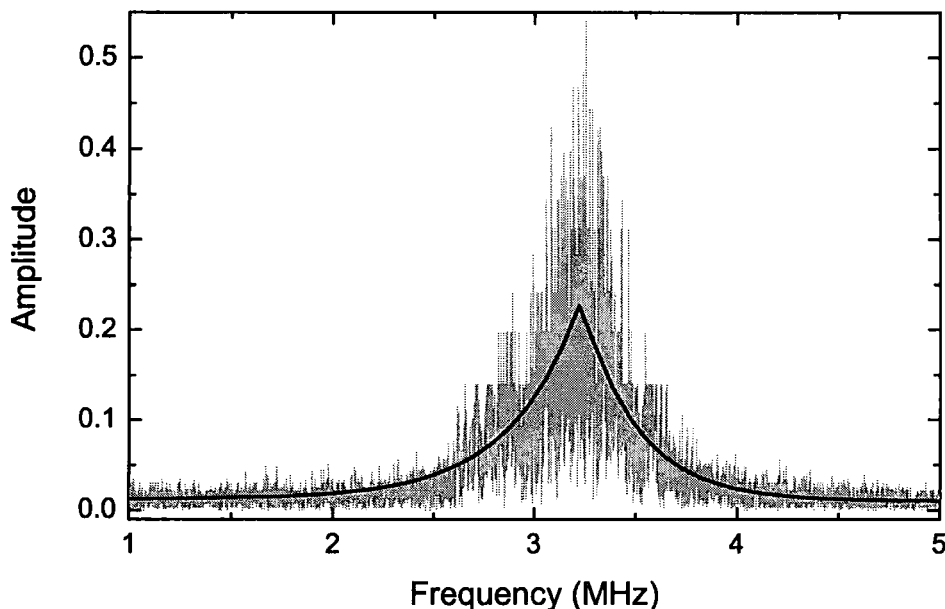
Figure 2.9: FFT of measured beat spectrum between two lasers frequency stabilised using polarisation spectroscopy (grey) with a back–to–back exponential fit. The FWHM is measured to be 625 kHz.

If the lasers drift in a correlated way, say due to temperature changes in the lab, this would not be evident from the measurement described above. We have monitored the individual error signals feedback to the piezo while the error is in lock and observe that the RMS value of this signal, typically 300 kHz, agrees with the beat measurements.

It has also been shown that the 'recapture' range of the polarisation spectroscopy signal is at least a factor of 3 larger than that of the saturation spectroscopy method. The saturation spectroscopy error signal has zero crossings separated by 60 MHz, giving a range of $\sim$ ± 30 MHz on the locking point. This is due to the fact that each peak in the spectrum has a zero crossing. The polarisation spectroscopy signal gives of a range of $\sim$ -50 MHz $\sim$ $+300$ MHz

on the lock point, see Fig. 2.3. This value was found by direct measurement of results. With a larger angle between the pump and probe beams the details of the polarisation spectrum were reduced. This increased the range on the lower frequency side of the lock point.

Fig. 2.10 shows the increased captured range and simpler error signal produced by polarisation spectroscopy when compared to dither locking, for the ^{85}Rb, $F = 2 \rightarrow F'$ transitions. Using polarisation spectroscopy gives zero crossings at -520 MHz and at $+60$ MHz, relative to the lock point, with the lower limit being off the scale of the figure. The dither method gives zeros at ≈ 10 MHz on either side of the desired lock point.
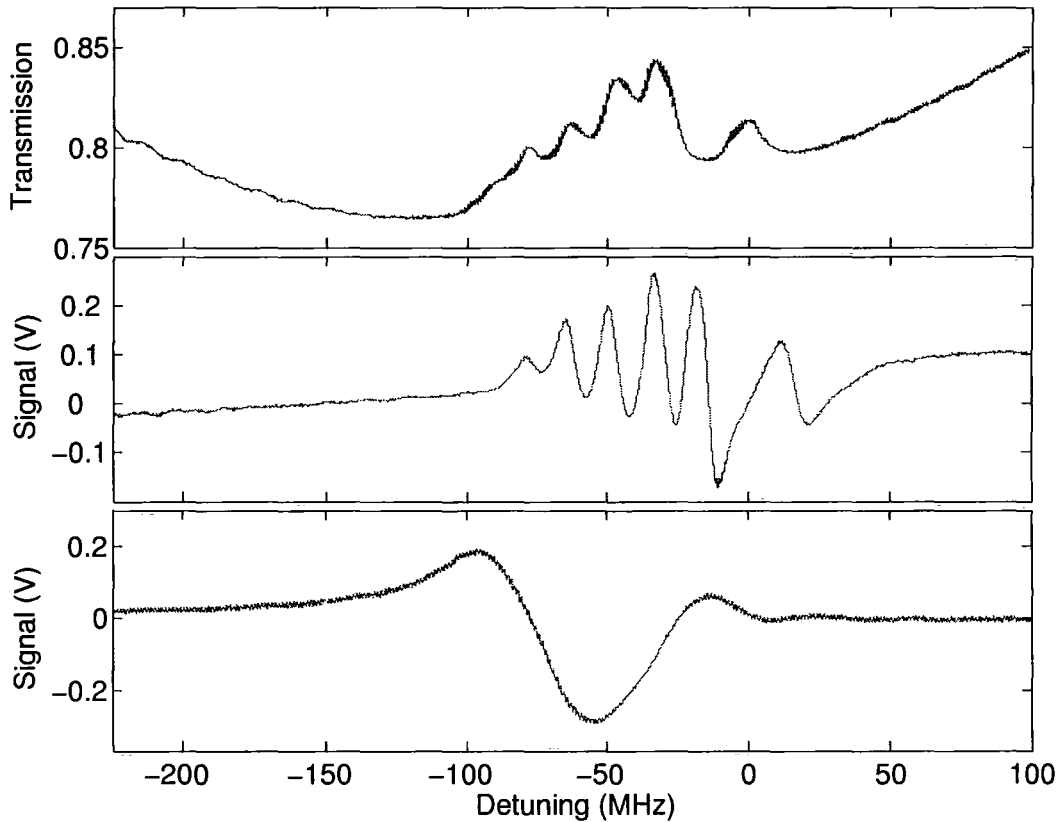
Figure 2.10: Saturated absorption spectrum **top)**, the corresponding error signal produced by a dither on the laser drive current **middle)**, and polarisation spectrum **(bottom)** of the ^{85}Rb, $F = 2 \rightarrow F'$ hyperfine features. The polarisation spectrum has fewer zero–crossings and a greater capture range than the dither–produced error signal. The zero crossing is close to the ^{85}Rb, $F = 2 \rightarrow F' = 1/2$ crossover feature, -78.1 MHz detuned from the repumping transition, $F = 2 \rightarrow F' = 3$ which is referenced as 0 MHz. For the polarisation spectrum the same setup as Fig. 2.3, **bottom)** is used.

Chapter 3

The Vacuum System

The cooling and manipulation of atoms with light is conducted within a vacuum as collisions between the cold atoms and the background gas results in the heating of the cooled atoms and their subsequent loss from the trapped system. The rate of these collisions is

$$R_{\text{loss}} = n_b \, \bar{v}_b \, \sigma \ , \tag{3.1}$$

or the product of the background density, the background gas velocity and the collisional cross section. An ideal solution to this problem is to conduct the experiments in the absence of a background gas or, the nearest experimental equivalent, an ultra-high-vacuum (UHV). The original BEC experiments required trap lifetimes at least on the order of a minute in order to complete rf-induced evaporative cooling to quantum degeneracy which in turn required background pressures on the order of 10^{-11} Torr [48]. By using optical dipole traps [49, 50] and atom-chips [51], BECs and Fermi–gasses can be achieved in a few seconds, which then lessens the requirements of UHV. However, in the case of vacuums, less is generally better.

3.1 Design

The vacuum system was designed with the aims of having maximum optical access at 780 nm and 10.6 μm, for cooling and dipole trapping beams, respectively, while minimising volume and surface area. The optical requirements are for cooling and trapping beams, and for observation. The second design goal
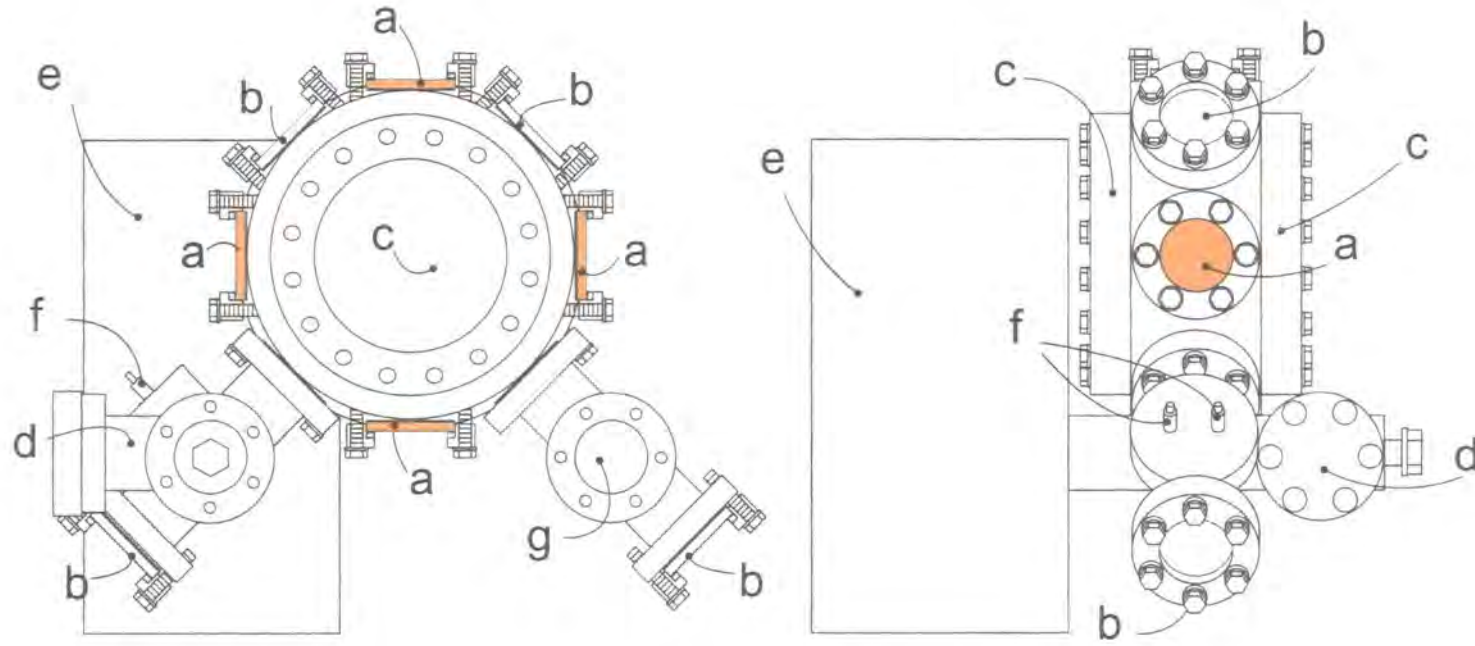
Figure 3.1: Front (left) and endwiew (right) of the vacuum chamber. The components labelled are: a) DN40, AR coated (10.6 μm), ZnSe, homemade viewports, b) DN40, AR coated (780 nm), commercial, BK7 viewports, c) large (DN100), AR coated (780 nm) commercial BK7 viewports, d) all metal valve, e) 40 ℓ/s Varian diode ion pump with Mu-metal shield, f) 10 A electrical feedthroughs, g) ion gauge.

was to optimise the final pressure reached in the chamber, which was achieved by keeping the volume to be pumped low and also keeping the area over which contaminants can degas to a minimum.

The vacuum system used in the experiments was based about a commercially available, stainless steel, Kimball (TM) spherical octagon. This is a ring cut parallel to a great circle on a hollow sphere of internal diameter 8.25 inches. Eight DN40 flanges are equally spaced about the diameter with a DN100 flange on each face. Optical access is required through all flanges, so a six–way–cross and four–way–cross are attached to provide provide access for an ion-pump, electrical feed-throughs for a rubidium dispenser and an ion-gauge, see Fig. 3.1. Fig. 3.2 shows a photograph of the chamber during initial testing of the quality of the vacuum attainable in the chamber.
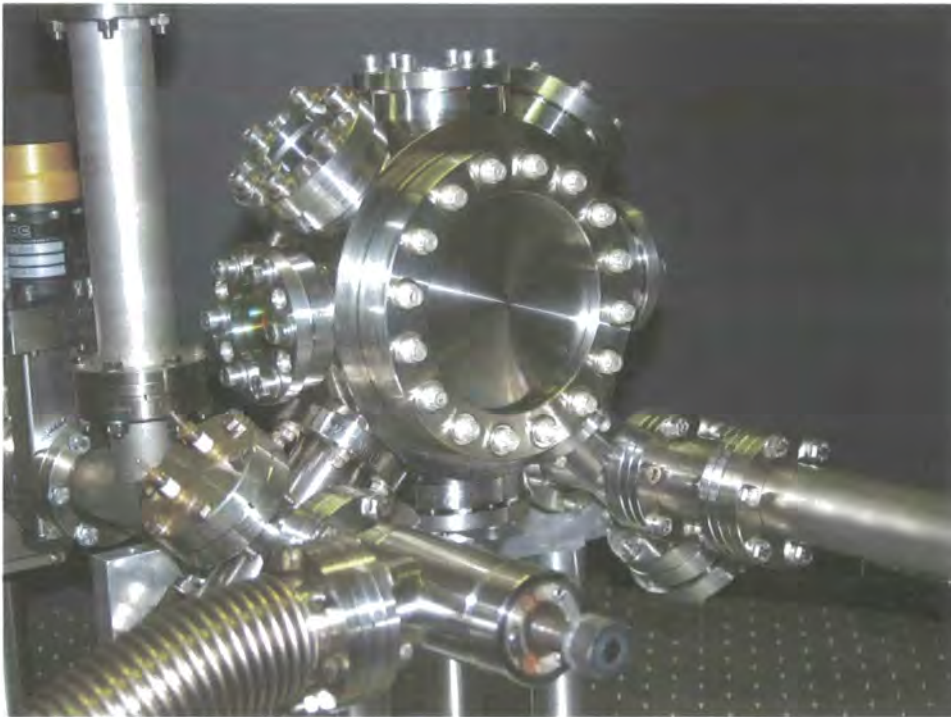
Figure 3.2: Photo of the vacuum chamber during testing of viewports. The large viewports are not attached in this figure.

3.2 Vacuum Pumps & Pressure Measurement

During normal operation, the experiment was pumped by a 40 ℓ/s Varian Vacion Plus 40 Diode ion pump [52], with an ultimate pressure attainable quoted at $< 10^{-11}$ Torr. Before the ion pump can be activated the pressure in the chamber needs to be reduced to below 10^{-5} Torr. This 'roughing' [53] was achieved with a Pfeiffer, PM033 759-T turbomolecular pump, pumping at 56 ℓ/s, backed by a Pfeiffer DUO 2.5A rotary pump, pumping at 2.5 m^3/s. An all–metal valve on the chamber provides access for these roughing pumps, allowing them to be removed when the ion pump is active.

The pressure in the chamber was measured with a Varian UHV ionisation gauge, positioned at approximately the same distance from the centre of the chamber as the ion pump, with no direct line–of–sight to the centre of the chamber, Fig. 3.1. The gauge was mainly used in the initial vacuum formation and occasionally as a diagnostic of the pressure. The lifetime of atoms in the optical dipole trap, Section 8.3.1, provides a very accurate estimate of the pressure in the chamber, Eqn. 3.1 [24, 54]. The gauge typically reads 1.2×10^{-10} Torr. Initial measurements of our trap of gave a trap lifetime of ~ 6 s (1/e). Based on empirical results of other groups [54] this confirms a pressure on the order of 10^{-10} Torr.

During a vacuum break in 2003, a titanium sublimation pump was added to the setup, positioned between the ion pump and the main vacuum chamber. It was found that this pump in fact increased the absolute pressure in the chamber, most probably due to contaminants. The addition of the titanium sublimation pump also moved the ion–pump further from the centre of the chamber, decreasing the effective pumping speed. This is due to the conductivity of a tube being inversely proportional to its length. The pump was removed during a later vacuum break.

3.3 Optical Access

For optical access at 780 nm BK7 viewports were used. These are available 'off-the-shelf' from Caburn. As these are a standard vacuum component they

can be obtained at high quality and not very high cost. The BK7 viewports were anti-reflection coated for 780 nm by CVI Optics to give a transmission coefficient of > 99.9%. BK7 glass, however is poor at transmitting radiation at 10.6 μm. To this end zinc selenide (ZnSe) is used as it has transmits well throughout the infrared. Commercial viewports with ZnSe are not so readily available and those that are of high cost with little option of optical quality. Based on these considerations we took a suggestion from David DeMille for a method of creating our own viewports, as described in the next section.

3.4 Reusable UHV Viewports

A number of groups have published designs for creating viewports, which could be used with any optical substrate. Man–made materials, such as Viton, elastomer O rings and Vacseal resin have been used to create seals [55, 56]. These suffer the draw back of only allowing low bakeout temperatures and limit the attainable pressure due to outgassing.

A soft metal would have the advantage of forming a good seal between a window and a vacuum chamber. Indium provides such a seal [57] but has the drawback of having a melting point of 157 °C, making it difficult to achieve UHV. A harder metal, such as copper, can also be used by forming a knife–edge in the metal [58]. However this technique requires a large pressure to be applied to create the seal which risks damaging the optical material. A compromise between these metals would be lead, which has a Young's modulus of approximately 18 GPA, similar to that of indium, 10 GPa. Lead has the advantage of a relatively high melting point of 327 °C and has been used to create seals with a low outgassing rate [59]. However, lead quickly forms a porus oxide layer which can absorb water and other outgassing contaminants.

Our design works on using a solder–seal with a modified rotatable vacuum blank [60]. Schematics of the seal are shown in Fig. 3.3 below. A seal is formed between an outer clamping flange, a solder cushion ring, the ZnSe window, a solder ring and the modified blank. The solder used is a flux–free solder, Indalloy 165, of diameter 0.76 mm commercially available from Indium Corp. The alloy is composed of 97.5% Pb, 1.5% Ag, and 1% Sn. The key details of the solder are
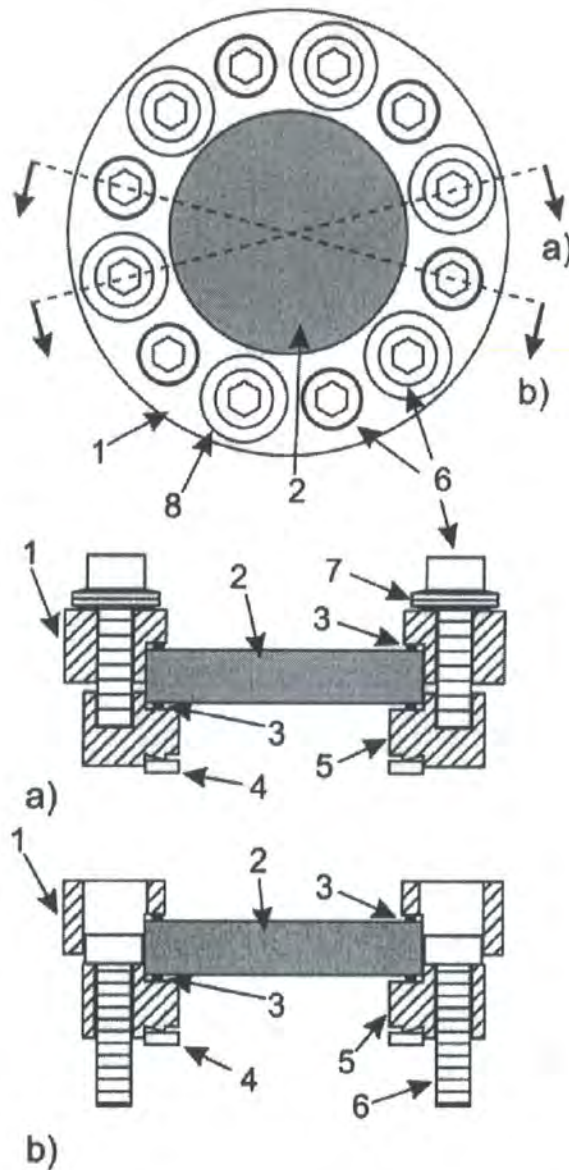
Figure 3.3: Schematic of the window design. (Top) From above and showing cross sections. (Middle and Bottom) Different cross-sections through the viewport, indicated by (a) and (b). The viewport consists of: (1) clamping flange, (2) window, (3) preflattened solder seal/cushion, (4) OFHC copper gasket, (5) modified Conflat blank flange, (6) socket–head screw, and (7) Belleville disk spring washers.

its high melting point, 309 °C, which allows for baking of the vacuum chamber to high temperatures, its Young's modulus which allows a good seal to form and the absence of outgassing materials in the solder itself. The solder used

does not appear to form an oxide layer and remains shiny indefinitely when cut. The solder is harder than either lead or indium but is still soft enough to form a seal.

The clamping flange was created in house from stainless steel. We have found that the main concern with this flange was to have the inner diameter of the lip at least 2 mm smaller than that of the cushioning ring, to prevent the cushioning ring coming out during baking. The flange has 12 holes cut into it; 6 with clearance for the threads of M6 bolts to couple the clamping and vacuum flanges, and 6 with clearance completely through for M6 socket–head bolts to connect the window to the vacuum chamber.

A circular solder seal was formed around a former and the end joined with a soldering iron. A good seal is a perfect torus with a constant radius of the ring. The roundness and evenness of the seal are very important and take some practice to create. Protuberances must be removed with a file. The seal was squashed to a thickness of ~ 0.2 mm with a compression jig to maximise surface contact between the seal and surfaces. Two of these seals were formed for each window; one to provide the vacuum seal between the vacuum flange and the ZnSe and the other ring acts as a cushioning seal to prevent an uneven load on the window causing cracking of the window. The viewport was constructed from the flange, window and solder rings, as shown in Fig. 3.3 and clamped to the chamber with M6 bolts.

Figure 3.4: Photo of viewports before being attached to chamber.

3.5 Assembly of the Vacuum Chamber

The ultimate pressure attainable in a vacuum chamber depends on the flux of gasses into the chamber and the pumping rate. In a stainless steel vacuum chamber, such as ours, essentially no gasses, except small amounts of helium and hydrogen, can leak into the chamber. The main source of contaminating gas is from out–gassing from chamber walls. To achieve a vacuum of 10^{-10} Torr great care must be taken to ensure that the vacuum components are clean.

Prior to assembly the vacuum parts were cleaned in the following way:

1. Parts were placed in a ultrasonic bath of Decon solution (a vacuum compatible detergent) for 5 hours.

2. Each part rinsed in and then soaked over night in distilled water.

3. Parts were placed in an ultrasonic bath of spectroscopic grade methanol for 2 hours.

4. Parts were placed in ultrasonic bath of distilled water for 5 hours.

5. Parts were dried with a hot air gun.

6. Parts were wrapped in layers of clean aluminium foil until use.

The vacuum components were assembled to the design described above, Fig. 3.1. Seals between components were made with Conflat knife-edges and annealed OFHC (oxygen-free, high conductivity) copper gaskets. Imperial sized, silver platted bolts were used on the Kimball ring and M6 nuts and bolts elsewhere. Silver plated bolts have good resistance to seizing and were used on the blind, tapped holes.

3.6 The Oven and Baking of the Chamber

The out–gassing of impurities from the interior surface of the chamber and within the metal itself greatly increases at increased temperature. To assist in baking of our vacuum chamber an oven was constructed. The design goals of the oven were that it have sufficient volume for the baking of a variety of vacuum

chamber, that it allow the baking to 250 °C, that it be well insulated to prevent heating the lab and to minimise energy used, and that it have external access for the backing pumps, the ion gauge cable, the ion pump cable and thermocouples. The oven would also be a permanent fixture. Previously within the group, vacuum chambers had been baked with heat tape which has the disadvantages of uneven heating across chamber leading to cold spots and difficult to insulate surrounding bench and optical components.

In our design, good insulation was achieved by using a multi layer design. The inner layer of the oven was formed from sheets of Alanod [61], which is a highly reflective metal sheeting. This formed a case with the front being removable for access. The outer insulating surface was made from Monolux [62], which is a rigid insulator similar to asbestos but without the health risks. The Monolux also covered on all sides with a front door for access and was painted with sodium silicate solution [63] as a sealant, as the material can be dusty. Between the Alanod and Monolux were many layers of aluminium foil with airgaps between. A frame for the whole system was made in house. Access for pumps and cables is provided through two holes in the base of the oven.

The heating power was provided by 5 heating elements within the oven - 4×400 W ceramic elements (RS part number 196-6462) and 1×1 kW heating element (RS part number 200-1229). The heating was controlled by a Chino DB 1000 Temperature Controller which, when used with a thermocouple, gives easily controllable heating.

The chamber was placed in the oven and attached to the roughing pumps and a RGA. The chamber was covered in many layers of aluminium foil to allow for even heating of the chamber. Using a turbo–pump backed by a rotary–pump, Section 3.2, the pressure within the chamber was brought down to less than 10^{-6} Torr. The oven was sealed up and the temperature was brought up to 200 °C at a rate of 1 °C/minute. The backing pumps and external vacuum pipes were heated to 160 °C with heating jackets to ensure that this section of the whole system also did not outgas into the chamber. Thermocouples positioned on the chamber, underneath the foil layers, measured the chamber temperature and was fed back to the temperature controller to allow the chamber to be maintained at a constant temperature. During baking the vacuum was monitored by recording the pressure at the ion gauge and also by taking mass

spectra with the RGA. The presence of contaminants; water, nitrogen, oxygen, hydrogen, carbon dioxide and carbon monoxide were continually measured in this way, giving a precise measure of the outgassing within the chamber. The chamber was baked for 2 weeks at 200 °C, when the pressure measured to be $\sim 10^{-7}$ Torr. The oven temperature was reduced to room temperature over the course of a day when a final pressure of 4×10^{-10} Torr was measured. The chamber was then valved off from the turbo pump. Over a period of a few months the pressure reduced to its final level of 1.2×10^{-10} Torr, pumping with the ion pump alone.

Over its lifetime the vacuum chamber has undergone at least 3 vacuum breaks.

3.6.1 Effect of Baking on Homemade Viewports

During the baking of the vacuum system the solder would soften causing gaps in the vacuum seal. To maintain constant pressure on the solder seal two Belleville conical disc springs were used with each of the M6 clamping bolts. These bolts were tightened with a torque wrench to 2.3 Nm when forming the window. It was found after baking that the ultimate pressure achieved was 1.1×10^{-9} Torr. Also, the torque on each bolt had decreased due to the softening and spreading of the solder during baking. This caused small leaks to form however these were small and easily remedied by increasing the torque on each bolt to 2.5 Nm and re–baking the chamber. During the cool down cycle a torque of 2.5 Nm was reapplied at about 70 °C. Evidence of the leaks and the effectiveness of the tightening can be seen in Fig. 3.5. A helium leak check around the seals revealed no change in the helium partial pressure within the chamber at the level of 10^{-14} Torr, the limit of the Stanford Instruments, residual gas analyser (RGA). The windows have been re-baked many times with no further leaks, even up to 275 °C.

3.7 Magnetic Shielding

In this experiment we employed two different methods to keep the experimental region free from external magnetic fields.
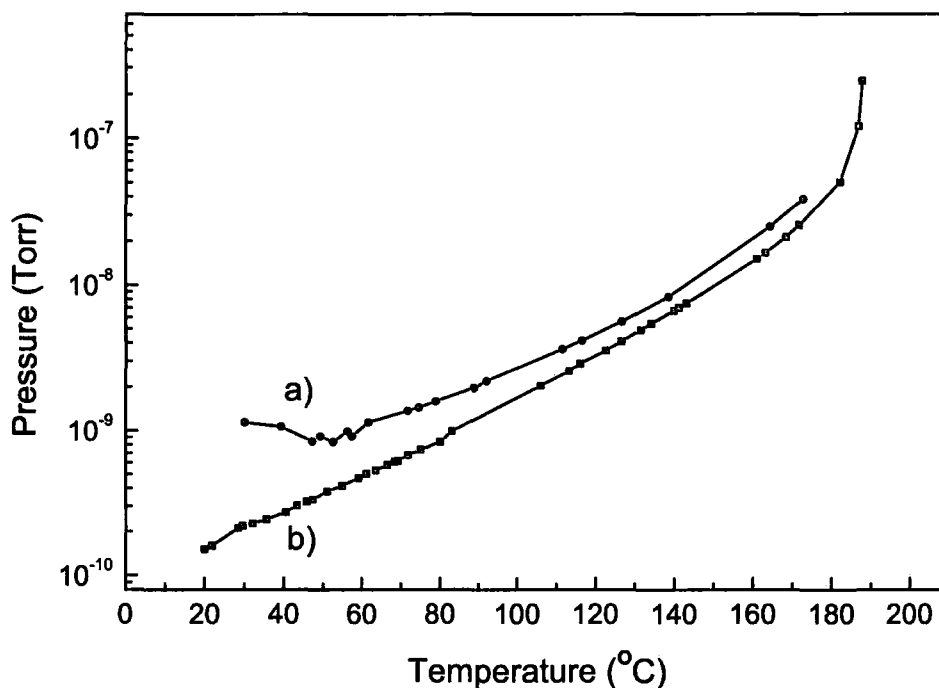
Figure 3.5: Cooling curves for the vacuum chamber, after baking at 180 °C for 16 hours. (a) With each socket-head screw on clamping flange tightened to 2.3 Nm and (b) with each socket-head screw on clamping flange retightened to 2.5 Nm.

3.7.1 Earth's Magnetic Field

It has been shown that a square Helmholtz coil produces a uniform magnetic field over a greater volume than a comparable circular coil [64, 65]. Also, square coils are more convenient to mount around an experiment.

To counteract the Earth's magnetic field a cubic frame, of side 0.55 m, was built about the experiment. Mounted to this were 3 pairs of coils in Helmholtz-type arrangements in the North-South, East-West and Up-Down directions. The current to each set of coils was controlled independently. This setup allowed for the independent application of B-fields of magnitude up to 0.6 G in three orthogonal directions, with a resolution of better than 0.01 G estimated from the resolution of the current supplies used.

3.7.2 Stray Field from Ion Pump

The ion pump used in the experiment has a large magnet attached to it which creates a large B-field gradient across the region of the MOT. This gradient will obviously affect the MOT performance due to an asymmetry in the magnetic field and trapping forces across the MOT. It is also necessary to have a zero B–field for good optical molasses. It is not trivial to compensate for B-field gradients with electromagnetic coils and would create gradients in the other directions.

To remove this problem a shield of Mu-metal was designed to enclose the ion pump. Mu-metal is a nickel-iron alloy (77% nickel, 15% iron, plus copper and molybdenum) of high magnetic permeability which strongly attracts magnetic fields in the region around. In this way it prevents fields passing through, thereby trapping the field of the ion pump within the shield. Three holes in the shield had to be allowed for to connect to the experiment, to allow electric access and for mounting. The size of these holes were all minimised. The shield reduced the magnetic field gradient across the chamber due to the ion pump magnet from 0.6 G/cm, with a field of $\approx$ 3 G at the MOT region, down to less than 0.03 G/cm, with a field of $\approx$ 0.1 G at the MOT. Fields of this level can be compensated with the magnetic–field cancelling coils.

Chapter 4

Laser Cooling of Alkali Atoms

Laser cooling [4] has become a very important tool of atomic physics research, a fact that was recognised by the awarding of the Nobel prize in 1997 for its discovery and advancement [1, 2, 3]. The techniques of optical molasses and magneto–optical trapping have allowed ultra–cold temperatures of μKs to be reached with arguably much greater ease than the cryogenic methods used by the hydrogen community and other fields. It has opened the way for almost routine production of quantum degenerate gasses [10, 11, 12, 66]. The fields of atomic spectroscopy and atom clocks have surged ahead due to hugely reduced Doppler shifts and very long interaction times [9]. Laser cooling also allows excellent access to the cold atomic sample for further manipulation or interrogation [48].

In this chapter the theoretical principles and experimental implementation of laser cooling will be briefly examined. The experimental methods to obtain clouds of $> 10^7$ Rb atoms at 20 μK in 3 s will be discussed as will the effect of different operating parameters on the loading of the MOT from a background vapour of thermal atoms.

Two of the Nobel lectures from 1997 begin with "in 1978" [1, 3]. Since the experimental field is then as old as I am (also, laser cooling of ions was first demonstrated in 1978 [67, 68]) only a brief discussion will be taken.

4.1 General Introduction

In order to localize an object to a point a position–dependent force is required, for example, $\mathbf{F_x} \propto -\mathbf{x}$. Similarly, to reduce the velocity spread of a group of atoms - i.e., to trap them in momentum space - a velocity dependent force is needed; $\mathbf{F_v} \propto -\mathbf{v}$. In laser cooling these forces arise from the interaction

Figure 4.1: An example of a position dependent force.

of an atomic ensemble with near resonant laser light. The laser linewidth is typically stabilised to less than that of the linewidth of the atomic transition, $\Gamma = (2\pi)6$ MHz. The laser detunings are typically $< 3\Gamma$, considerable less the hyperfine splittings of the excited atomic states, which are typically on the order of 100 MHz. The atomic system can then be well approximated by a two level system.

Each absorption of a photon results in the atom acquiring a recoil velocity of $\mathbf{v}_{\text{recoil}} = \hbar \mathbf{k}/M$ (M = mass of atom) over the time of the transition to an excited atomic state. The atom decays back to the ground state by spontaneous emission of a photon of energy $\hbar k_0$, where k_0 is the wave number corresponding to a resonant photon, in a random direction. The time averaged impulse on an atom due to many such spontaneous emissions is zero. The force on an atom due to a single laser beam is then given by the product of the photon momentum and the rate of photon absorption,

$$\mathbf{F}_{\text{scatt}} = \hbar \mathbf{k} \cdot \frac{\Gamma}{2} \frac{I/I_{\text{sat}}}{1 + I/I_{\text{sat}} + (2\Delta/\Gamma)^2} \,, \tag{4.1}$$

where I is the total intensity of light at the atom, I_{sat} is the saturation intensity, $\Gamma = 1/\tau$ is the linewidth of the excited state, τ is the lifetime of the excited state and $\Delta = \omega - \omega_0$ where ω_0 is the resonant frequency of the EM transition between the two atomic levels.

4.1.1 Doppler Cooling

Doppler cooling, as proposed in 1975 [69], provides frictional cooling for atoms, i.e. a velocity dependent force. Doppler cooling makes use of the atomic velocity distributions and the narrow linewidths and frequency tuning available with lasers. It can be assumed that if the force does go as $\mathbf{F} \propto -\mathbf{v}$ then it should be possible to reduce the velocity of atoms down to zero. However, the stochastic nature of the cooling mechanism means that atoms undergo a random walk, which acts as heating. The threshold of Doppler cooling comes about by balancing of the cooling and heating through the spontaneous emissions, which gives the limiting Doppler temperature of [4, 70],

$$T_{\mathrm{D}} = \frac{\hbar \Gamma}{2 \, k_B} \; . \tag{4.2}$$

For the D_2 line in ^{85}Rb and ^{87}Rb, $T_{\mathrm{D}} = 145 \ \mu\mathrm{K}$, and is the same order of magnitude for the other alkalis [4, 71].

4.1.2 Sub–Doppler Cooling

Soon after the observation of temperatures close to the Doppler limit [14] temperatures six times lower than T_{D} were observed in Na [72]. It was after this experimental observation that it was realised that the multi–level nature of atoms could allow cooling to much lower levels [73, 74]. Spatial variations in the polarisations of the combined laser fields cause spatially varying light–shifts of the magnetic sub–levels. The additional frictional force due to the presence of the wells, along with spontaneous emission mean it is possible to cool within these wells, a mechanism that was called Sisyphus cooling [73]. The theories predicted that the minimum attainable temperature is limited by the depth of the potential wells caused by these light–shifts,

$$T_{\mathrm{min}} \propto \frac{\Omega^2}{\Delta} \tag{4.3}$$

$$\propto \frac{I}{\Delta} \; , \tag{4.4}$$

where Ω is the Rabi frequency and

$$\Omega = \Gamma \sqrt{\frac{I}{2 \, I_{\mathrm{sat}}}} \; . \tag{4.5}$$

Again, following from Eqn. 4.4 we could presume that for $I \to 0$ or $\Delta \to \infty$ then $T_{\min} \to 0$. This presumption fails when the energy gained from a photon recoil is equivalent to the depth of the spatial potentials. A further reason is that in the μK regime the atomic de Broglie wavelength,

$$\lambda_{\mathrm{dB}} = \frac{h}{p}$$
$$\approx \frac{h}{\sqrt{2\,M\,k_B\,T}} \,, \tag{4.6}$$

becomes comparable to the wavelength of the cooling light and the extent of the potentials. It then is not possible to localise the atomic wavepacket to the potential wells. This new minimum temperature, the recoil limit is,

$$k_B\,T_{\mathrm{recoil}} = \frac{\hbar^2 k^2}{M}$$
$$= 2\hbar\,\omega_0$$
$$= 2\,E_{\mathrm{recoil}} \,. \tag{4.7}$$

The experimentally realised minimum temperatures are approximately $10\,T_{\mathrm{recoil}}$.

4.1.3 Magneto–Optical Traps

Optical molasses [75] provide cooling in momentum space but do not provide the position dependent force to spatially trap atoms. Such a tool is the magneto–optical trap (MOT), suggested by Dalibard and experimentally realised by Raab *et al.* in 1987 [76]. The essential operation is most clearly seen in a 1D scheme which can be extended to 3D. Here we consider transitions $F = 0 \to F' = 1$, but the technique is applicable to any transitions of the form $F \to F' = F + 1$. A linear magnetic field with a zero at $z = 0$ creates the energy level shifts shown in Fig. 4.2. We take the B–field as the quantisation axis, allowing this axis to change direction about $z = 0$. The Zeeman shift of a transition energy is

$$\Delta_z = (g_{F'}m_{F'} - g_F m_F)\,\frac{\mu_B|B|}{h} \tag{4.8}$$
$$= \frac{\mu'|B|}{h} \,,$$

where g_F, m_F are the Landé g–factor and magnetic quantum number, μ_B is the Bohr magneton and μ' has absorbed the magnetic factors.
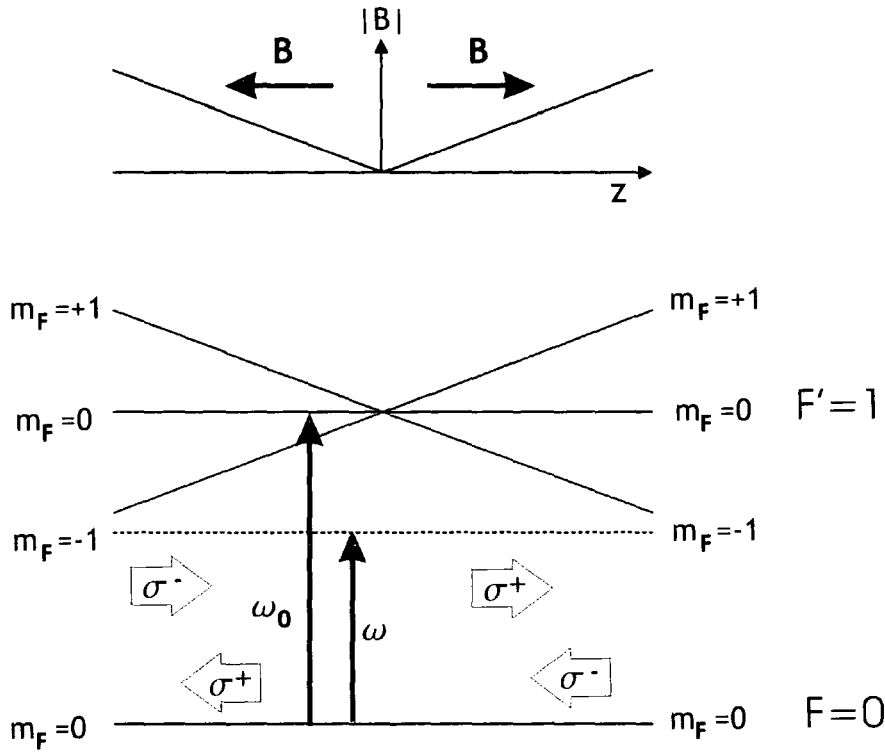
Figure 4.2: A 1D model for the operation of a MOT on a $F = 0 \to F = 1$ transition.

We now introduce a pair of counter–propagating, red–detuned laser beams. Both lasers are right–hand circularly polarized. A laser directed towards $z = 0$, i.e., against the quantisation axis, drives σ^- transitions, $m_F \to m_{F'} = m_F - 1$ in the atoms. A laser in the direction pointing away from $z = 0$, i.e., with the quantisation axis, excites σ^+ transitions, $m_F \to m_{F'} = m_F + 1$. Because of the Zeeman shift the $m_F = -1$ level is always closest to resonance for the B–fields we use. The 'inward' propagating beam, exciting σ^- transitions, is scattered more than the σ^+ beam and the atom is always being pushed towards $z = 0$. From this model, it should be clear that each individual laser beam is both σ^- and σ^+.

Raab *et al.* show that the force in the MOT is given by [15]

$$F_{\text{scatt}} = -\alpha\, v - \kappa\, z \;, \tag{4.9}$$

which provides the desired position and velocity dependent forces. The frequency for such a trap is $\sqrt{\kappa/M}$, whereas the dampening rate is α/M. The

capture range for the MOT is limited by the requirement that $\Delta_z < \Delta$.

The MOT can be extending into 3D using a laser arrangement of three, orthogonal sets of counter–propagating beams and a quadrupole field generated by a pair of coils running in an anti–Helmholtz type configuration.

4.2 Loading of a Magneto–Optical Trap

The cliche of low temperature AMO physics must be "the MOT is the workhorse of atomic physics". Like Boxer in Animal Farm [77] the MOT, when setup, works in almost all conditions and tolerates many of the errors of the experimentalist/farmer/pigs. To optimise the loading rate and number of atoms trapped the alignment, polarisations and intensities of the laser beams, the magnetic field gradient and the Rb vapour pressure must be set exactly, but the MOT still works if any, or all of these is slightly wrong. However, in this section the correct operation of the MOT will be discussed.

4.2.1 Experimental Setup

To create a MOT a good vacuum (Chapter 3), stabilised lasers (Chapter 2) and a source of the element to be trapped (Section 4.3) are required.

The laser setup, prior to the experimental chamber is shown in Fig. 4.3. The output beam from the trap laser has e^{-2} radii of 0.7 mm vertically and 1.4 mm horizontally. The beam is passed through an expanding anamorphic prism pair to give a beam which is has a circular cross section ($\pm5\%$). The beam is passed through an optical isolator to prevent undesired optical feedback into the laser. A reference beam is split off from the trap laser on a polarising beam splitter (PBS). This low power beam, typically 1 mW, is double passed through a 80 MHz acusto–optic modulator (AOM) before being used for polarisation spectroscopy, as described in Section 2.4. This means that the laser light output from the laser is -160 MHz detuned from the lock frequency. The main beam is then double passed through another AOM, the frequency of which can be varied between 55 MHz to 100 MHz. This AOM thus allows changing of the cooling laser beam frequency between -50 MHz and $+40$ MHz of the lock point.

To experiment chamber
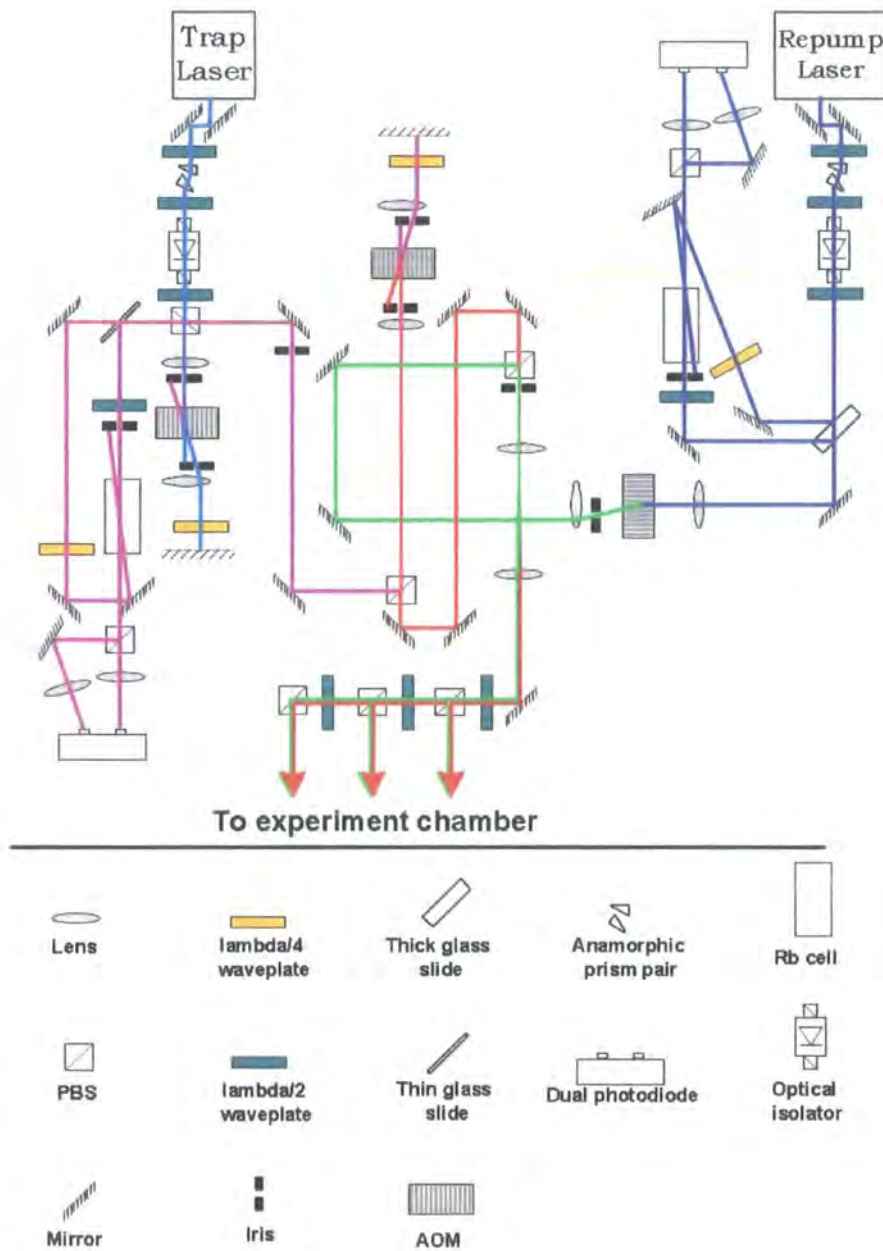
Figure 4.3: Setup of the trapping/cooling laser and the repumping laser.

The hyperfine repumping laser has a more simple setup than the trapping laser. The beam is similarly conditioned by passing through an anamorphic prism pair and optical isolator. Approximately 1 mW of power is picked off by a thick glass slide to provide two beams - pump and probe - for polarisation spectroscopy.

Due to the form of the polarisation spectroscopy spectrum the repumper is locked to the $F = 2 \rightarrow F' = 1; 2$ crossover. The main beam is sent single–pass through an AOM to shift the frequency by the 78.1 MHz required to have the laser resonant with the $F = 2 \rightarrow F' = 3$ transition. This AOM also allows fast switching of the laser power. A shutter was added after the AOM as up to 600 μW was found to 'leak' into the first order beam when the driver was set to zero. The increased extinction of the repumper allows for increased loading of the optical dipole trap and reduced trap loss [78].

The cooling and repumper lasers were combined on a PBS. The beams were then expanded with a 5:1 telescope. Using a setup of $\lambda/2$ waveplates and PBSs (Fig. 4.3) three beams with equal intensities of cooling light were obtained. Due to the orthogonal polarisations of the cooling and repumping lasers unequal amounts of repumper pumper went into each beam. This effect was due to combining the beams on a PBS but was not expected to affect the MOT operation.

The MOT is formed from three orthogonal laser beams, which are retro–reflected. The cooling beams were measured to have a radius of 7.5 mm ($1/e^2$) before the chamber and a peak intensity of 9 (± 0.2) mW cm^{-2}. Two of the beams are in a vertical plane, each at 45° to the vertical, and one in the horizontal plane. Prior to entering the chamber each beam is passed through a $\lambda/4$ plate to create the circular polarisation required of the cooling beams. On exiting the chamber the beams are passed through another $\lambda/4$ waveplate and then retro–reflected along the beam path to create the light field configuration described in the previous section. For alignment purposes a variable aperture is centred on each beam before the chamber. Using small beams allows for precise alignment of the beams on the magnetic field zero. The retro–reflected beams were aligned by aligning the returning beam on the back of the aperture.

Acousto–Optic Modulators (AOMS)

Three AOMs were used in the experimental setup. These are used to provide frequency shifts of the laser beams and also to control the laser power to the experiment in the cooling and repumping lasers. Concerns were raised by others within the Durham AtMol group about the stability of the Isle Optics (TM)
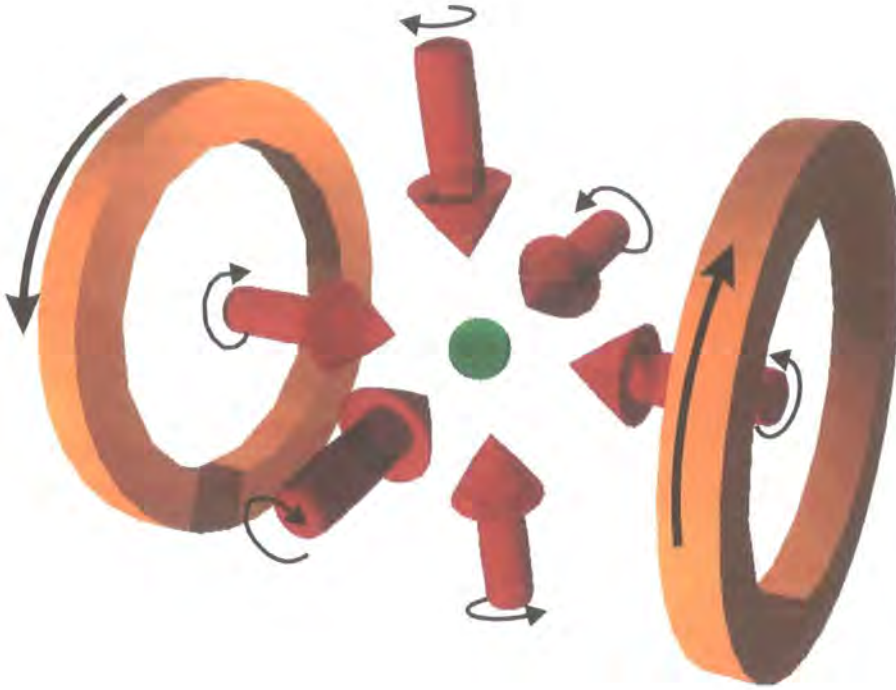
Figure 4.4: Setup of the MOT lasers and magnetic coils. The direction of the currents in the coils and the handedness of the polarisation of the beams are indicated.

AOMs and drivers. However, the power to the experiment was measured to be constant to better than 1% and was not observed to require time to stabilise, apart from rise/fall time, after switching from on to off, or vice versa. The frequency shift of the laser was more difficult to measure but the frequency from the driver was monitored over 30 minutes after a frequency shift of 10 MHz, which is typical of the shifts that are used during an experiment. The shifts are measured with a frequency counter and hence could not be measured on timescales shorter than required to take a reading. The results, shown in Fig. 4.5 show that there is a drift in the frequency over a time scale of 10 minutes, but on a scale of only 10 kHz which is much smaller than the estimated laser linewidth of 1 MHz and thus insignificant.
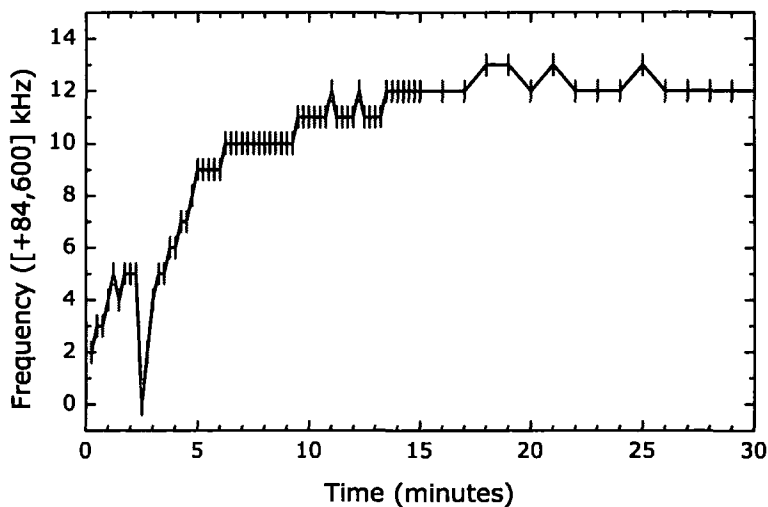
Figure 4.5: Frequency output of the AOM driver measured over 30 minutes after a frequency shift of 10 MHz. The errors indicated are reading errors.

4.3 Atomic Source – Rb Dispensers

The source of Rb in the experiments are two SAES getter-dispensers, located in the chamber as shown in Fig. 4.6. The active region of the dispenser is 1.2 cm long and contains a compound of rubidium chromate along with a reducing agent, see Fig. 4.7. Rb is released in a chemical reaction when the dispensers are heated to the threshold reaction temperature of a few hundred °C. The exact threshold temperature of this reaction hasn't been found in the literature or from SAES themselves, but has been estimated as $\sim 500\,$°C. This heating is usually provided by passing a current to Ohmically heat the dispensers. The dispensers are mounted on a Macor base to thermally and electrically isolate from the vacuum chamber. They are connected in series and connected to the 'outside' through 10 A vacuum feed–throughs. Kapton-coated copper wire provides all connections within the vacuum chamber.

When first installed the dispensers must be run in. Existing literature [79, 80] prescribes slowly increasing the current to heat the dispensers and evaporate off contaminants while ensuring the pressure within the chamber does not increase by more than an order of magnitude. We performed this procedure while baking our chamber, see Section 3.5. The pressure and composition of gasses in the chamber were carefully monitored with an ion–gauge and residual gas analyser

Figure 4.6: Photograph showing the position of the dispensers in the vacuum system. The dispensers are the silver strips in the lower left of the large viewport. The wires over the dispensers are to prevent a direct line of light from the thermal source to the MOT.

(RGA) as the current was increased up to 4.5 A. The pressure was not allowed to rise above $\sim 10^{-6}$ Torr. The process took almost 24 hours.

During typically operation of experiments the dispensers were turned on at 2.5 A first thing in the morning. Over 30 minutes the steady–state number of atoms captured in the MOT increased to a final value of 5×10^7. The current was then reduced to 2.3 A. The steady–state number captured in a MOT was not observed to decrease. The current to the dispensers was turned off at the end of each day. The ion gauge registered an increase of $\sim 0.2 \times 10^{-10}$ Torr, from
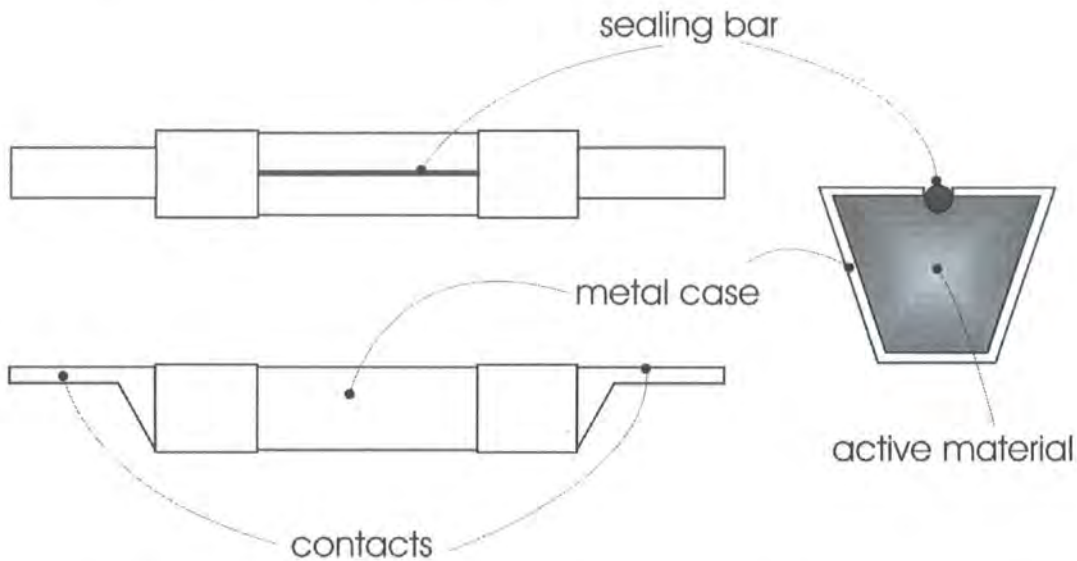
Figure 4.7: Left) schematic of the SAES dispensers used in the experiment. The metal case, contacts and sealing bar are made from stainless steel. Right) cross section through a dispenser, showing the active material, which is a mixture of rubidium chromate with a reducing agent.

1.2×10^{-10} Torr, when the dispensers were initially turned on, but recovered within a minute.

Whenever there was a vacuum break we installed new dispensers, in the hope that the chamber would never have to be opened again. After these vacuum breaks running in was performed more quickly by increasing the current in steps of approximately 0.2 A and then allowing the pressure to recover. This procedure took about 4 hours. There was no observable difference in the dispenser operation after using this method.

4.4   MOT Magnetic Field Coils

To provide a magnetic field with a zero in the centre and a linear gradient through the central region two coils were arranged in an anti–Helmholtz type configuration. These MOT coils were formed from hollow wire with an external square cross section of length 4.25 mm and a circular inner cross section of diameter 2.25 mm. The large Ohmic cross–section lowers the resistance of the coil, while the large surface area of the bore allows for cooling of the coils.

Cooling is provided by water, chilled to 14 °C, pumped through the inner bore of the coils. To protect against failure of water supply leading to the coils over-heating a flow switch is positioned after the MOT coils. Tripping of this switch, due to the flow rate of the cooling water going below a set value, shuts off current to the MOT coils. The coils were wound on a mount made of Perspex made to fit over the large windows on the vacuum chamber, Fig. 3.1. The coils were of inner radius 75 mm, had 7 turns and were separated by 78 mm. The gradient of the B-field through the centre was measured to be 0.0816 ± 0.002 G cm^{-1}A^{-1}. The current to the coils is supplied by a Hewlett Packard 6671A power supply
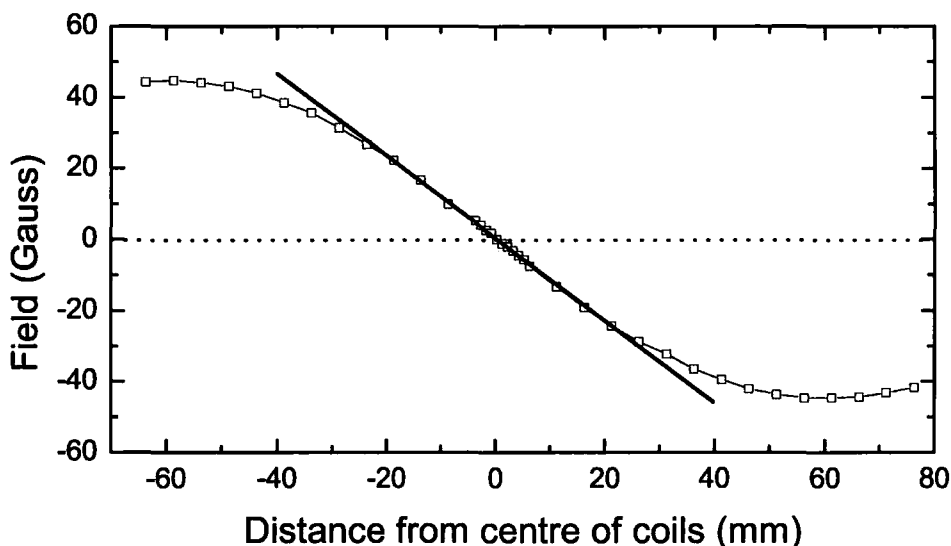
Figure 4.8: B–field along the axis between the MOT magnetic coils for a current of 150 A. The gradient in the centre of the coil is 12.33 ± 0.22 G cm^{-1}. The thick line is an aid to show that this linear region is ~ 2 cm on either side of the centre.

capable of providing 150 A, giving a maximum B–field gradient of 12.25 G/cm. A plot of magnetic field along the axis of the coils is shown in Fig. 4.8. Switching of the current is with a bank of three MOSFETs in parallel with gates linked. The MOSFETs are used as a digital switch. The drain of the MOSFET bank was connected to the power supply and the source to the MOT coils, see Fig. 4.9. A Schottky diode (International Rectifier 203CNQ100R) was placed across the MOT coils to prevent oscillations in the MOT coil current during switching.
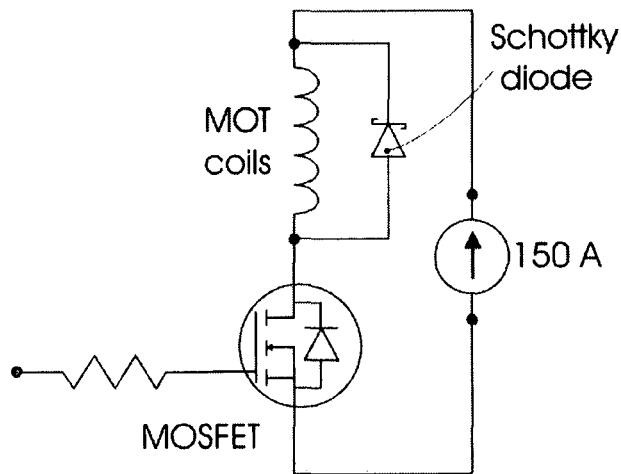
Figure 4.9: The MOT coil electronic setup. The resistor on the MOSFET gate ensures the gate draws a current to fully open. The diode across the MOT coils prevents voltage spikes during switching of the inductive load which could damage the MOSFET.

Without a diode the coils can be switched off completely in a timescale of 100 μs but the current direction changes sign a number of times. The diode slows the switching time down to 2 ms (from constant current to 0 A) but provides a smooth, almost exponential decay of the current in the coils, as shown in Fig. 4.10.

4.5 Loading Rates into the MOT

The number of atoms trapped in a MOT is a balance between the rate at which atoms are captured R and the loss rate from the trap. The number of trapped atoms over time is given by Monroe *et al.* as [81],

$$N(t) = N_{\mathrm{s}} \left(1 - e^{-\frac{t}{\tau}}\right) , \qquad (4.10)$$

where N_{s} is the steady state number of atoms and $1/\tau$ is the loss rate due to background collisions and is assumed to be independent of N.

In the experiment the partial pressure of the thermal vapour of Rb atoms is determined by the current through the dispensers. Fig. 4.11 shows the variation in the number of atoms in the MOT with time for increasing dispenser current. We see that the trapped atom number is negligible up to a threshold current
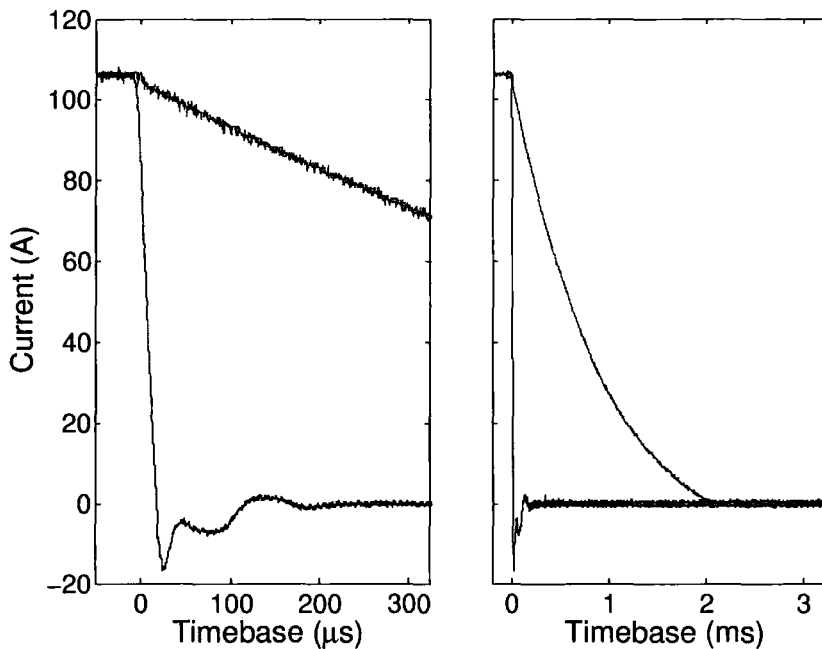
Figure 4.10: Effect of a diode across the MOT coils during switching off of the current. Without the diode (bottom line), the current switches off completely in 200 μs, but shows transient oscillations that could cause heating of trapped atoms or could damage the MOSFET switches. With the diode (upper line) the switch off takes 2 ms, but with a much smother turn off.

of approximately 3 A. The steady state atom number and loading rate then increase rapidly up to a dispenser current of $\sim$ 4.25 A when the steady state number begins to saturate. At the highest currents, corresponding to the highest background pressure of Rb, the steady state atom number peaks due to the increased trap losses from collisions with hot thermal atoms. The loading rate of atoms is shown explicitly in Fig. 4.12.

4.6 Optical Molasses

To achieve good molasses cooling the intensities of the laser beams need to be balanced and the magnetic field in the molasses region has to be reduced to zero. The intensities of the molasses beams were measured before the chamber and were matched to better than 5%. The Earth's B–field cancelling coils allowed bias fields of up to 0.6 G to be applied in orthogonal directions with a resolution
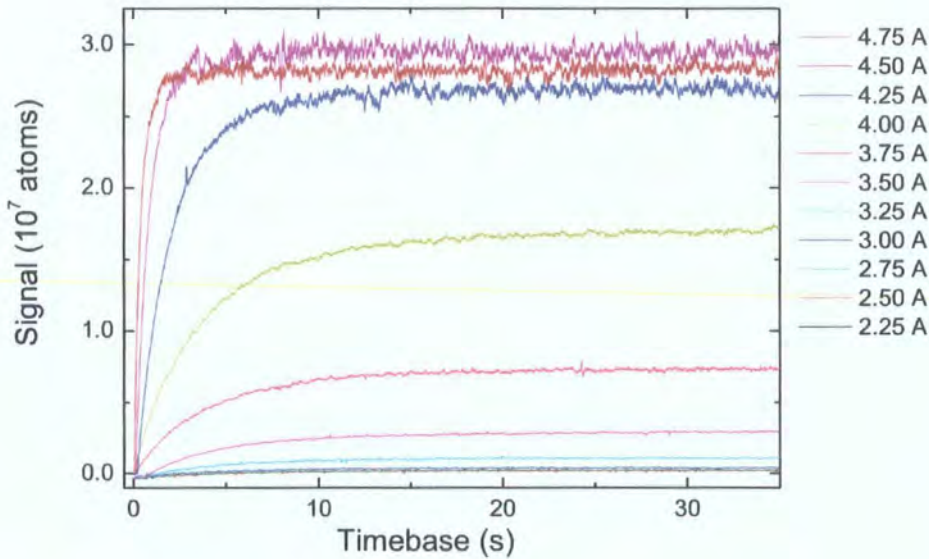
Figure 4.11: The variation of atom number in the MOT with time for varying heating currents through the dispensers. For larger currents the steady atom number reaches a maximum and then begins to decrease at the highest currents as a result of increased losses due to the increased background pressure.

of 5 mG. The cancelling coils were optimised by reducing the B–field gradient of the MOT coils and adjusting the cancelling coils until the MOT position was observed to not move with varying MOT B–field gradient. This indicates that the MOT centre corresponds to a B–field zero. In practice the individual fields were adjusted until the cold atom cloud showed slow, isotropic expansion when the MOT magnetic fields were suddenly switched off while leaving the lasers fields on.

It was found that a molasses duration of ≥ 10 ms was required to achieve the lowest temperatures in the optical molasses. For shorter and longer durations, the shot–to–shot temperature was found to vary up up to $\pm 10\%$, Fig. 4.13.
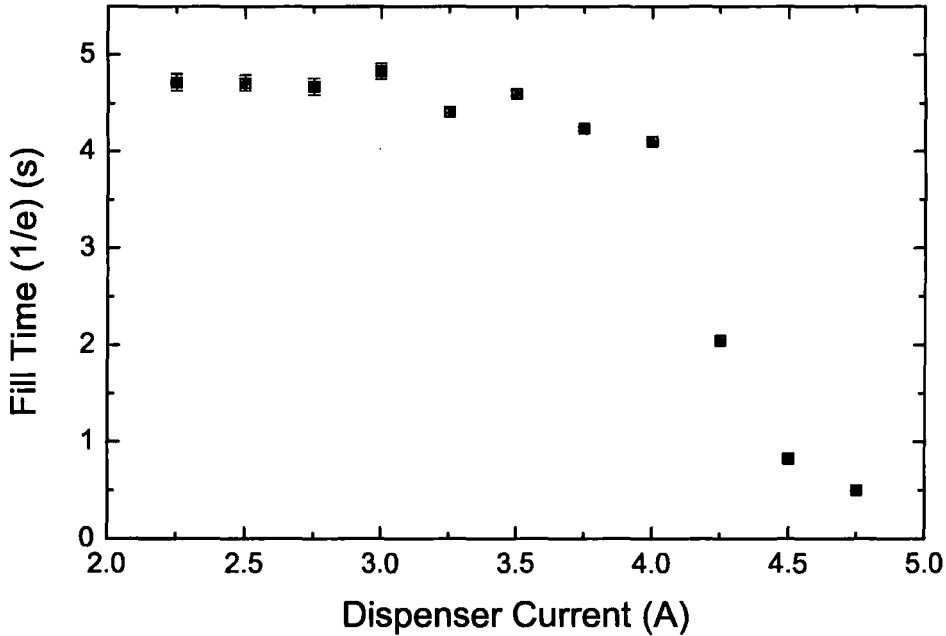
Figure 4.12: Loading time, τ (Eqn. 4.10) of the MOT as a function of dispenser current.

4.7 MOT Diagnostics

4.7.1 Atom Number

A knowledge of the number of atoms trapped is desired. Also, the fill rate of the MOT is a good diagnostic of the MOT operation and optimisation. Both these properties, can be measured by monitoring the scattered fluorescence from the MOT region over time with a sensitive photodiode. The total power measured at the photodiode will be give by the product of the energy per scattered photon, the solid angle over which photons are measured, the number of photons measured and the rate photons are scattered,

$$P_{\mathrm{pd}} = \frac{h\,c}{\lambda} \cdot \frac{\Omega}{4\pi} \cdot N \cdot \Gamma_{\mathrm{sc}} \;. \tag{4.11}$$

The fractional solid angle can be approximated by

$$\frac{\Omega}{4\pi} \approx \frac{\pi\,r^2}{4\,\pi\,R^2} \;, \tag{4.12}$$
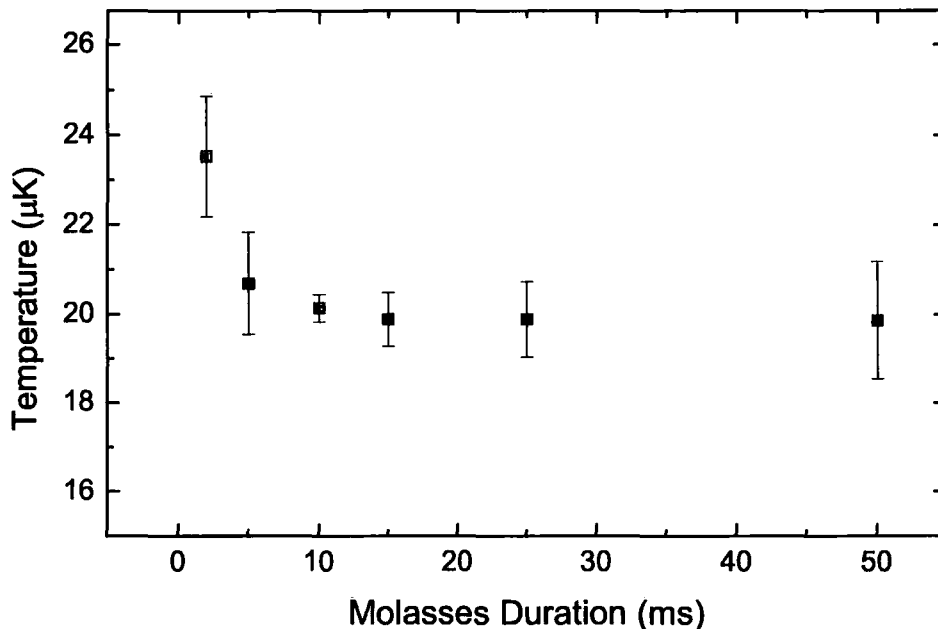
Figure 4.13: Variation of temperature with molasses duration. Data were taken for 10^7 atoms at a molasses detuning of $\Delta = -5\,\Gamma$ and single beam intensities of 4 mW/cm^2. Note that the temperature before molasses was measured as 190 μK.

where r is the radius of the lens collecting the scattered light and R is the distance from the MOT to the lens. By using a large area lens close to the MOT and focussing the collected light on the photodiode the percentage of scattered light collected will be greatly increased. The scattering rate can be calculated from

$$\Gamma_{\rm sc} = \frac{\Gamma}{2} \frac{I/I_{\rm sat}}{1 + I/I_{\rm sat} + (2\Gamma/\Delta)^2} \ . \tag{4.13}$$

In this equation it is unwise to use the value of $I_{\rm sat} = 1.6$ mW/cm^2, the saturation intensity for the closed $m_F = 3 \rightarrow m'_F = 4$ transition. During imagining all polarisations will be excited and $I_{\rm sat}$ will be larger for all transitions other than the closed transition. The guide, *BEC For Everyone* [66] suggests using a value of $I_{\rm sat} = 4.1$ mW/cm^2.

In the experiment a $f = 10$ cm lens, with an open aperture of 4.8 cm, 20 cm from the MOT was used to collect light scattered by the cold atoms. For
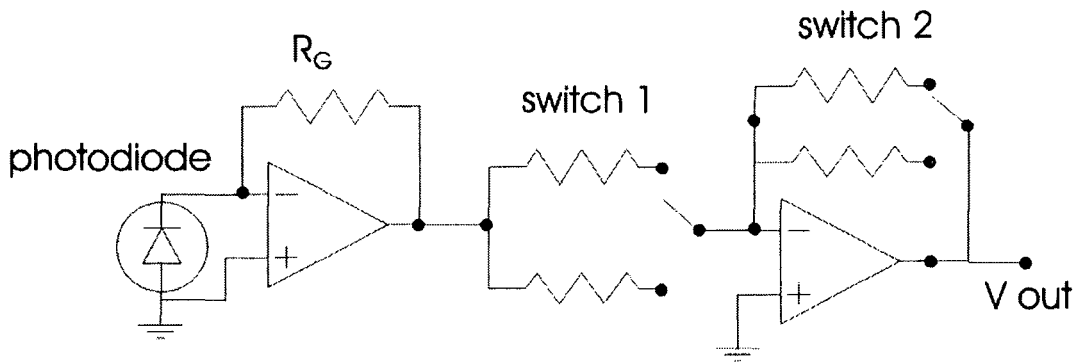
Figure 4.14: Photodiode circuit used to collect scattered fluorescence. R_G = 1 MΩ converts the current signal from the photodiode into a voltage. The two switches allow for four levels of gain.

MOT parameters of 9.2 mW/cm^2 per beam at a detuning of -2Γ then Γ_{sc} = $(2\pi)1.2$ MHz. The power estimated at the photodiode, from Eqn. 4.12, is 6.7×10^{-15} W/atom. For enhanced signal–to–noise, the photodiode was mounted in a light proof box with a narrow band filter which was measured to transmit only 65 % at 780 nm. The photodiode used, (IPL10050 CW) has a sensitivity of 0.45 A/W which then corresponds to a signal of 1.9×10^{-15} A/atom. Using a two stage gain of 10^6, Fig. 4.14, we have a measurable signal of 5.3×10^{-6} atoms/V. To measure larger clouds the gain after the photodiode stage can be reduced by $\times 10$.

4.7.2 Temperature

Due to the magnetic field gradient of the MOT coils being a factor of two higher in one direction the cloud has a pancake shape with a ratio of the widths of 2:1. Technical issues, such as the laser beams being not perfectly Gaussian and noise in the laser frequency and intensity, mean that the cold atom cloud has an irregular shape. Arnold *et al.* indicate that the temperature and density vary across a MOT but do indicate that a Gaussian density distribution is valid [82].

The temperature of the cloud of atoms was measured using a time–of–flight (TOF) technique, as introduced by Lett *et al.* [75]. The atomic cloud is released from the trapping fields and the spatial distribution is monitored over time. By comparing this distribution to a Maxwell–Boltzmann distribution the
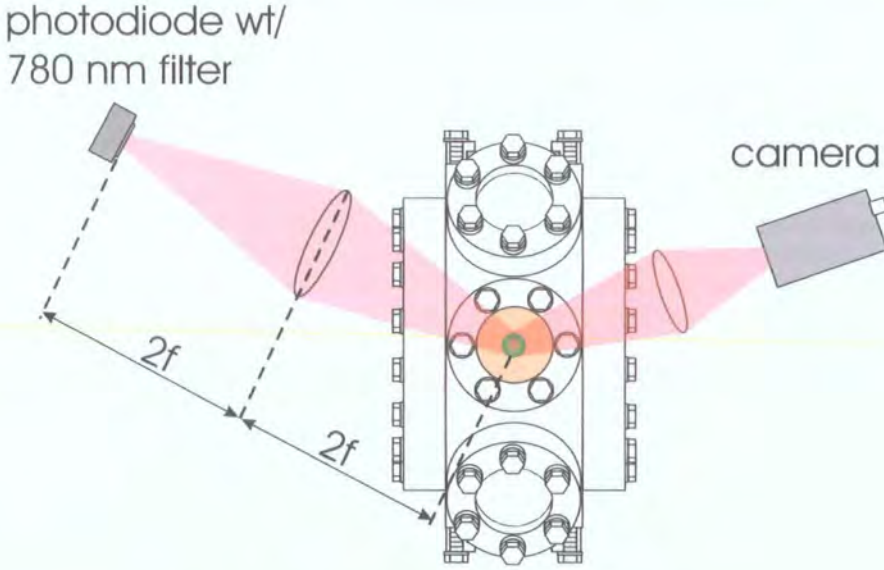
Figure 4.15: Set up of the imaging optics.

temperature can be found [83].

We assume that density of atoms has a Gaussian dependence,

$$g(x) = \frac{1}{\sqrt{2\pi\sigma_x^2}}\, e^{-\frac{x^2}{2\sigma_x^2}} , \tag{4.14}$$

and similarly for velocity, assuming a Maxwell–Boltzmann distribution

$$
\begin{aligned}
f(v_x) &= \sqrt{\frac{m}{2\pi\, k_B\, T_x}}\, e^{-\frac{m\, v_x^2}{2\, k_B\, T_x}} \\
&= \sqrt{\frac{m}{2\pi\, k_B\, T_x}}\, e^{-\frac{m(x_f - x_i)^2}{2\, k_B\, T_x\, t^2}} ,
\end{aligned} \tag{4.15}
$$

where we make use of

$$x_f = x_i + v_x\, t . \tag{4.16}$$

The final position distribution is also a Gaussian and can then be found by a convolution of Eqns. 4.14 and 4.15. The expansion of the MOT cloud is then of the form,

$$\sigma_x(t) = \sqrt{\sigma_x^2(0) + \frac{k_B T_x}{m} t^2} . \tag{4.17}$$

By measuring σ_x, the Gaussian width of the cloud along the x (or equivalently the y or z directions) for different release times, the temperature is

$$T_x = \frac{m}{k_B} \frac{\sigma_{xf}^2 - \sigma_{xi}^2}{t_f^2 - t_i^2} . \tag{4.18}$$

Alternately, plotting t^2 against σ_x^2 gives a graph of slope $T_x \cdot k_B/m$ and intercept $\sigma_x^2(0)$ from which the temperature is easily extracted.

Experimentally we observe that the observed time–of–flight data follows the behaviour predicted above. We have not used any other methods for temperature measurement but as the method described here is the standard method in the cold atom community we have some faith in the results.

4.8 Laser Heating of Dispensers

In December 2004 electrical continuity across the vacuum feed–throughs was found to have been lost; in other words the resistance across the feed–throughs went from 0.4 Ω to open circuit with no warning or sign. No cause could be discovered and all connections appeared, to the eye, to be okay.

It is not important to the emission of a Rb vapour how the dispenser is heated, as long as the active material is heated above the threshold temperature. The experiment has a 10 W, Lightwave Electronics 220 Nd:YAG laser ($\lambda = 1.064$ μm) as part of the setup that was used in the previous generation dipole trapping experiments [84]. It was attempted to use this laser to heat the dispensers.

4.8.1 Coupling of Laser Radiation to Metals

The theory of coupling energy from a laser beam to a metal has been mainly examined for laser cutting applications, where a focussed laser beam moves relative to a metal surface and melts the material [85, 86]. The situation looked at here is for heating of a metal bar in thermal contact with thin sheets of the same metal and also with a complex chemical compound. We will only look briefly at the theory as a detailed examination would be time consuming and quite possibly fruitless. The question that we wish to answer is whether we can heat a piece of stainless steel to > 500°C with less than 10 W of Nd:YAG laser power. To do this we need to know about the thermal and optical properties of stainless steel and the coupling of laser radiation at 1.064 μm to stainless steel.

The heat flow problem for a homogenous and isotropic solid is [87]

$$\nabla^2 T - \frac{1}{\kappa}\frac{\partial T}{\partial t} = -\frac{A}{K}, \tag{4.19}$$

where T is the temperature, A the rate at which heat is supplied per unit time per unit volume, K is the thermal conductivity and κ is the thermal diffusivity. κ is given by other known quantities as

$$\kappa = \frac{K}{\rho C},\tag{4.20}$$

with ρ the material density and C the heat capacity. For a CW Gaussian beam of power P focussed to a $1/e^2$ radius w_0 Bass gives a solution for the temperature at the laser centre on the surface as [87],

$$T(t) = \frac{4\sqrt{2}\,\alpha\,P}{K\,\pi^{3/2}\,w_0}\,\tan^{-1}\left(\frac{8\,\kappa\,t}{w_0^2}\right)^{1/2}.\tag{4.21}$$

This clearly implies a limiting temperature of

$$T|_{t\to\infty} \to \frac{2\sqrt{2}\,\alpha\,P}{K\,\pi^{1/2}\,w_0}.\tag{4.22}$$

Using the data provided by Bass [87] for stainless steel,

$$
\begin{aligned}
K &= 0.26 && (\text{W/cm}\,^\circ\text{C}) \\
C &= 0.6 && (\text{J/g}\,^\circ\text{C}) \\
\rho &= 8 && (\text{g/cm}^3) \\
\kappa &= 0.054 && (\text{cm}^2/\text{s}) \\
\alpha &= \sim 0.1
\end{aligned}
$$

implies, for a power of 2.5 W, a limiting temperature of 440°C. However it also implies that this temperature is reached very quickly, on the order of 10 ms. However this assumption is for a solid, isotropic amount of stainless steel. The dispenser has a thin wall of steel and is then in contact with the chemicals within. The thermal conductivity and correspondingly, the thermal diffusivity are sure to be lower (no data is available) so it can be postulated that the maximum temperature achieved will be higher and the rate of temperature increase slower than predicted for solid stainless steel due to the lower values of κ and K.

4.8.2 Laser Induced Emission of Rb from a Dispenser

The examination above would appear to give lower estimates of the limiting temperatures and time taken to achieve these. Even with these considerations

we still had no feeling of the result that could be obtained, so we took a conservative, systematic approach. The Nd:YAG laser was passed through a $\lambda/2$ waveplate and a PBS, in order to control the power. The laser was then focussed onto the dispenser, through the large viewports, with a $f = 10$ cm lens, Fig. 4.16. The peak intensity at the laser focus is given by,

$$I_0 = \frac{2P}{\pi \omega_0^2} .$$

(4.23)

Due to the construction and orientation of the dispensers the Nd:YAG beam had to be focussed at an angle through the 6 mm thick viewports. This caused significant astigmatism of the beam, with the vertical and horizontal foci being separated by 7.8 mm. The minimum spot sizes in each direction were 21 μm vertically and 24 μm horizontally. The minimum area of the focus, the 'circle of least confusion' had a $1/e^2$ radius of 35 μm. From Eqn. 4.23 the peak intensity at the focus is then, $I_0 = 5.2 \times 10^4$ W/cm^2 per W of laser power. A CCD camera, with a 780 nm filter to block out scattered $\lambda = 1.064$ μm light, was positioned to monitor the position the Nd:YAG laser was focussed to and also to estimate the efficiency of the heating due to the thermal glow, Fig. 4.17. The fluorescence from the MOT was recorded to monitor the efficiency of the Rb emission. It was quickly found that if the laser was focussed with a power of
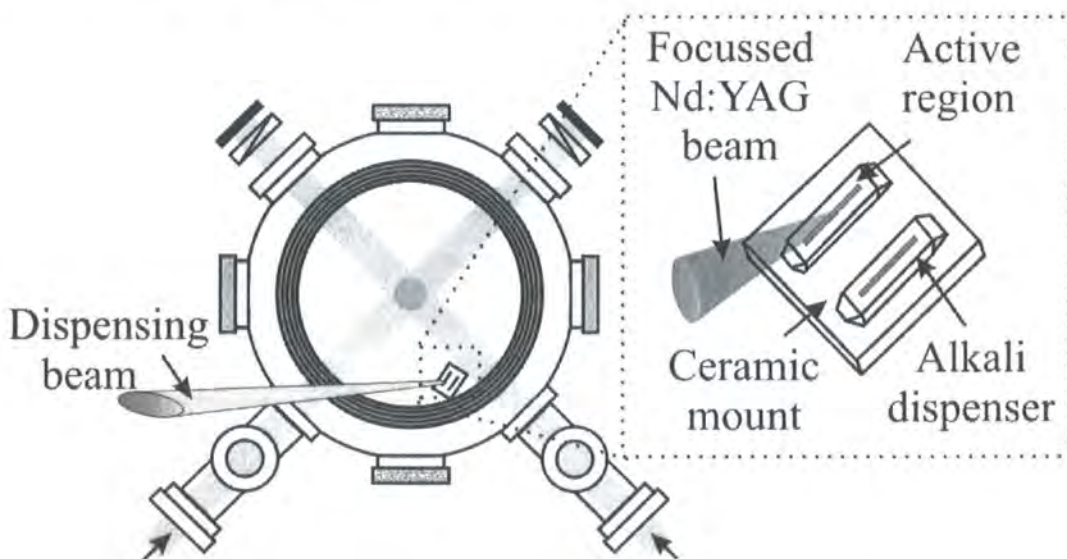
Figure 4.16: Schematic of focussing of the Nd:YAG beam onto a dispenser. The intense laser beam produces a thermal atom source that loads a MOT in the centre of the chamber. A magnified view of the dispensers is shown inset.

Figure 4.17: CCD images of alkali dispensers without (left) and with (right) the heating beam. The beam spot lies on the bar above the active region, see Fig. 4.7.

1 W on the bar that protects the active material within the dispenser then the MOT fluorescence was observed to increase. Increasing the laser power to 2 W showed a rapid increase in the MOT fluorescence.

Experiments were conducted to examine the potential of the technique for our loading experiments [88]. Loading of the MOT was performed by turning on the dispensing laser for 5 s and turning on the MOT at a variable delay relative to the end of the heating pulse. Fig. 4.18 shows the collected fluorescence from the MOT for delays of a) +10 ms, b) −2.5 s and c) −5.0 s. A dramatic reduction in collected fluorescence was observed when the MOT was turned on 10 ms after the dispensing laser was extinguished. Based on the signal–to–noise ratio of the photodiode signal we would place a conservative upper limit of 100 ms on the switch off time of the atom source.

Increasing the dispensing beam power increased the number of atoms trapped. For example, for a pulse time of 2.7 s, increasing the power from 2 W to 3 W increased the number of trapped atoms by a factor of 2.6 to 4.2×10^7. Further increasing the power to 4 W increased the number of trapped atoms to 7.5×10^7. However, at higher powers the recovery time of the background pressure also increased to many seconds, measured by increased loss from the optical dipole trap. Increasing the pulse duration results in larger trapped atom numbers, as should be expected from Fig. 4.18. The equilibrium trapped atom number, for laser powers ≥ 2 W was measured as $> 10^9$, limited by the MOT laser beam size. This equilibrium number took over 100 s to achieve and the background
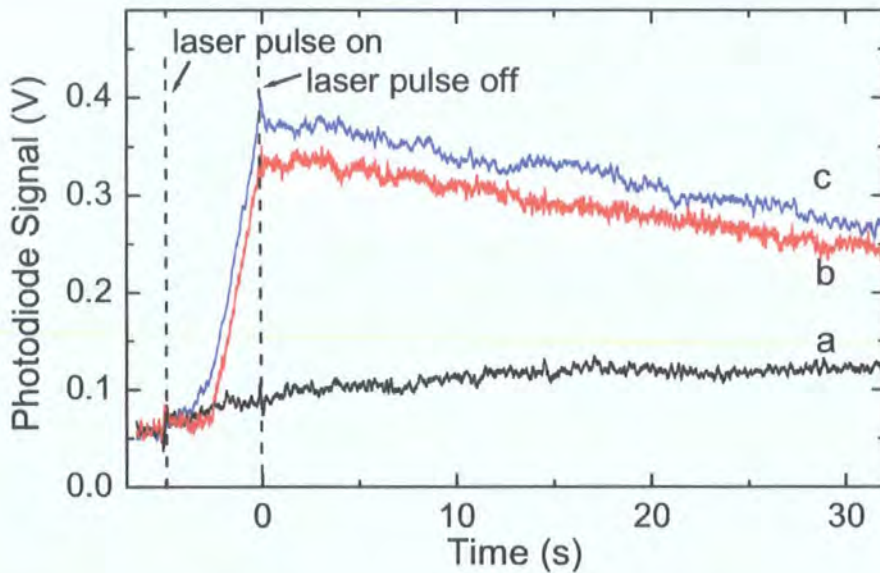
Figure 4.18: Atomic fluorescence signal from the MOT for different times between turning the dispensing laser off and the MOT field on. In each case 2 W of the dispensing laser is pulsed on for 5 s, and turned off at t=0 s. The MOT B field is on at (a) t=0.01 s, i.e., 10 ms after the dispensing pulse is switched off, (b) t=-2.5 s, and (c) t=-5 s, i.e., MOT on at the start of the dispensing pulse. Line (a) shows that the switch off time of the Rb flux is on the order of 10 ms.

pressure took many minutes to recover.

The optimum position of the heating laser focus was along the bar which protects the active region within the dispenser, see Figs. 4.7, 4.16. The flux of atoms varied with the position of the heating beam along the bar. Also, when the dispensing laser was used repeatedly on a single spot, over a period of weeks, the number of atoms captured in the MOT began to decrease by $10 - 20\%$. However, by moving the focus by $\sim 100\ \mu$m along the bar the original flux was recovered.

To obtain a measure of the repeatability of light induced dispensing, the MOT was loaded on a cycle of fixed loading times. Fig. 4.19 shows the atom number as a function of time for pulsing on both the dispensing laser and the MOT trapping fields for 4.1 s, followed by 3.5 s of no dispensing or MOT trapping. We typically loaded 2.4×10^7 atoms with a standard deviation of 10^6. We observed that using lower powers (0.5 W) increased the shot–to–shot variation
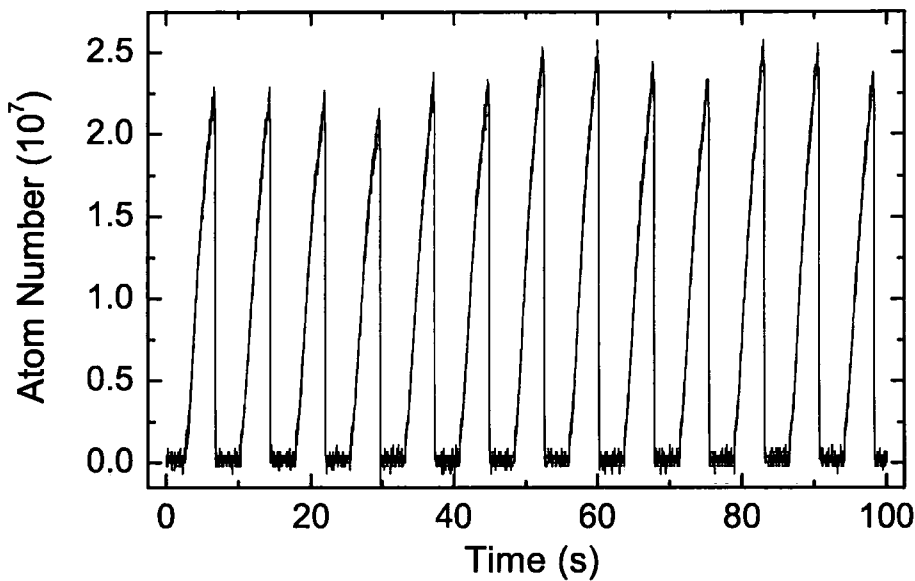
Figure 4.19: Trapped MOT atom number from repeated pulsing of the dispensing laser (2 W for 4 s) and MOT trapping fields. The mean of the peak number of atoms loaded is 2.4×10^7 atoms, with a standard deviation of 10^6.

of number of atoms trapped in the MOT.

It was observed that the switch–off time of the atom source was very rapid, though the turn on time could be greater than 1 s. This can be explained as follows: when the dispenser is heated by the dispensing–laser beam the temperature locally rises until the laser is extinguished, assuming the laser is not on long enough to reach a steady state temperature. When the laser is extinguished the temperature falls. Fig. 4.20 illustrates the temperature variation as a function of time. As the alkali metal vapor emission is a threshold phenomenon the turn off time can be considerably faster than the turn on time. However, if the laser is switched on again before the local temperature reaches "room temperature" then the local temperature will reach the threshold value more rapidly than before. In a pulsed sequence the time taken to reach the threshold temperature will decrease and the local maximum temperature will increase for each pulse. However, these effects saturate to steady state values after a few cycles due to the balance between the heating and thermal losses. This behaviour is confirmed by our experimental observations, namely when the dispensing laser is used in single–shot experiments the time constant to reach a threshold atom number is greater than that in pulsed experiments. In

Fig. 4.18, the time taken to start dispensing atoms is 1.3 s whereas in a pulsed experiment, such as shown in Fig. 4.19, the time taken to start dispensing is only 0.2 s.
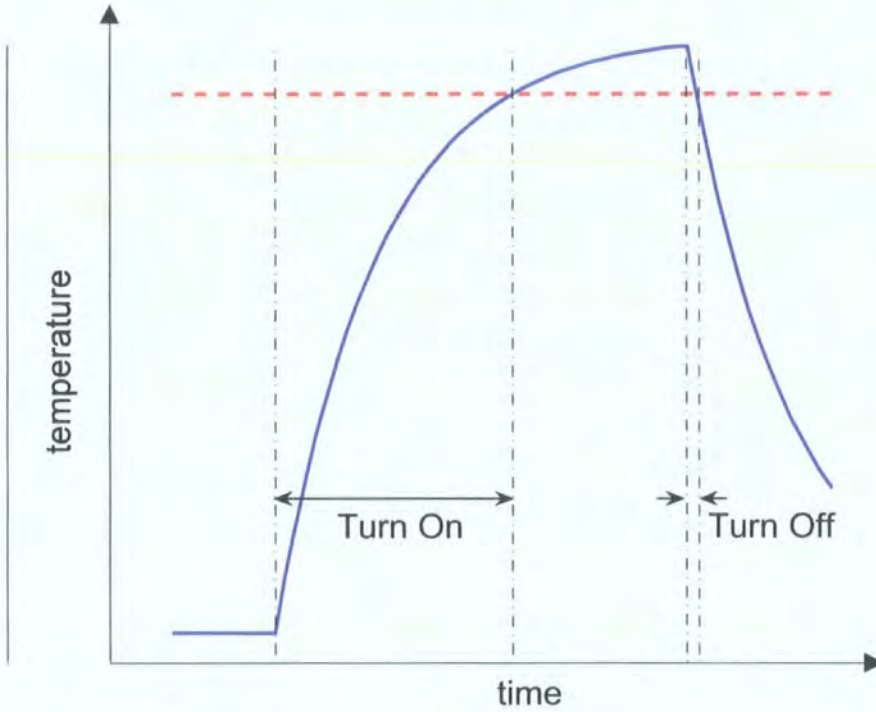
Figure 4.20: Schematic of the temperature vs. time behavior of the active region of the dispenser. The figure shows the difference in the 'turn on' and 'turn off' times of the alkali metal vapor release for a single pulse of the heating laser. The dashed, horizontal line marks the threshold temperature for emission of the alkali metal vapor

A shutter was used along the Nd:YAG beam to switch the emission of the Rb vapour. By triggering the shutter closing from the captured MOT fluorescence we could stabilise the number of atoms loaded into the MOT. A Schmitt trigger was used, as it provides stable switching from a signal with noise, due to hysteresis in the switching [89]. The simple circuit used is shown in Fig. 4.21. The triggering voltages are

$$V_{up} = \frac{R_1 \, || \, R_2 \, || \, R_3}{R_1} V_{ref} + \frac{R_1 \, || \, R_2 \, || \, R_3}{R_3} V_{ref} \qquad (4.24)$$

$$V_{down} = \frac{R_1 \, || \, R_2 \, || \, R_3}{R_1} V_{ref} - \frac{R_1 \, || \, R_2 \, || \, R_3}{R_3} V_{ref} \, , \qquad (4.25)$$

where $R_1 \,\|\, R_2 \,\|\, R_3$ is the parallel resistance of the three resistors. Hysteresis occurs in the switching due to the sign difference in V_{up} and V_{down}. In the circuit used, Fig. 4.21, $V_{ref} = 5$ V.
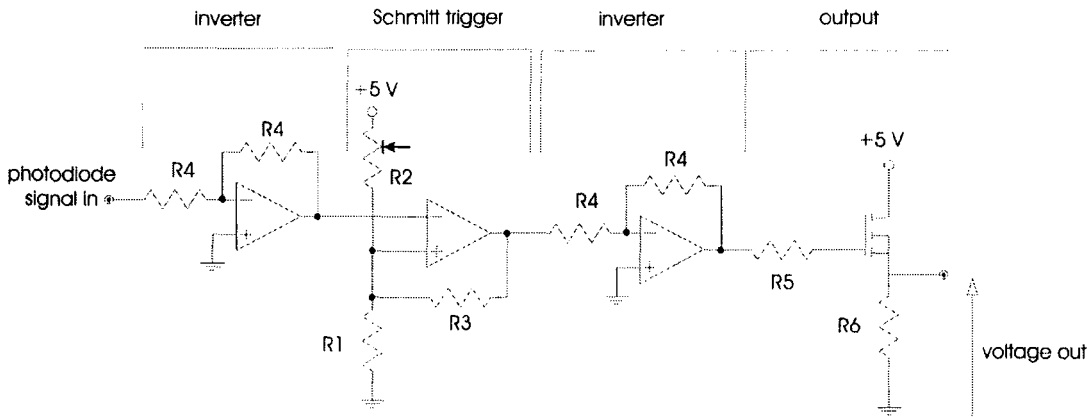
Figure 4.21: Circuit diagram of the Schmitt trigger used to trigger the start of the experiment from the fluorescence photodiode signal. The first inverter is used as the photodiode circuit outputs a negative voltage. The Schmitt trigger section also outputs a negative voltage which is also inverted. A circuit without inverter stages was attempted but not found to work. The FET is opened when the trigger is switched by the photodiode signal. The values of the resistors are; R1 = 4.7 kΩ R2 = 200 kΩ, variable, R3 = 200 kΩ.

The use of high powered diode lasers was also examined as a cheaper laser source. High power laser diodes (> 1 W) with high quality spatial mode are available but cost–per–Watt are more expensive than many Nd:YAG lasers. A cheaper option is to use a diode bar laser, though the poor beam quality from this type of laser makes it difficult to achieve a small spot size and the corresponding high intensity required. We used 2 W diode bar laser (High Power Devices HPD1120 2 W bar) and observed a Rb flux from the dispensers. However, the number of atoms captured, and the capture rate in the MOT were an order of magnitude lower than from using 2 W of Nd:YAG power. This was attributed to the better quality of the Nd:YAG beam.

As an aside, while the use of this technique was a discovery born out of desperation we have found that the technique was very useful for our experiments and has some advantages over existing sources of atoms for laser cooling. The main attributes of the laser induced emission are a high atom flux followed by

a very fast switch off time. This allows large clouds of atoms to be trapped without compromising the background pressure or trap lifetimes. Nearly all BEC experiments use a separate chamber or a large Zeeman slower to precool the atoms from a background vapour and then transfer to a science chamber for experiments. This increases the vacuum and laser requirements of the experiment and adds much complexity. A technique such as laser induced emission of atoms could remove the need of a precooling stage.

4.9 Shutters
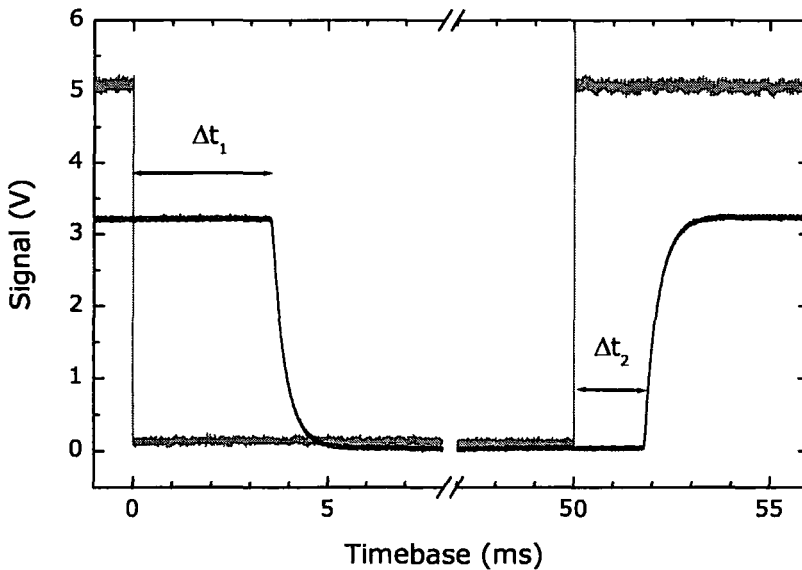
Figure 4.22: Typical switching characteristics of the shutters used in the experiments. The shutter is positioned at the focus of a telescope, with an estimated beam waist of 20 μm, and the transmitted power is monitored on a photodiode. The trigger pulse is shown in light grey and the transmitted light is shown in black. The delays, Δt_1 and Δt_2 are constant to better than 50 μs.

Shutters, based on the Singer *et al.* design [90] were used on the repumping laser and also on the Nd:YAG laser used to heat the dispensers. The shutters use a modified speaker coil which has the speaker cone trimmed off, to reduce weight. A lightweight 'flag', made from aluminium is moved to block the beam.

The coils are powered by a simple FET circuit which can then be triggered from LabVIEW. Typical performance of the shutters is shown in Fig. 4.22.

The shutters compared well with expensive, commercial shutters used in other experiments within the group in that they displayed very little jitter when either opening or closing. The jitter was on the noise level of the oscilloscope, and was estimated at < 50 μs. Over the course of a year 2 shutters failed, with no sign of wear before ceasing to work completely. Replacing a shutter is a quick and easy job and characterising the new shutter merely requires a photodiode in the beam.

Chapter 5

Experimental Control

5.1 Introduction

When all hardware is in place - the vacuum system holds an UHV, the lasers
are 'locked', aligned and have the correct polarisations, and the dispensers are
available to provide a rubidium vapour - then the running of the experiment is
down to millisecond and microsecond switching of lasers, magnetic fields and
cameras. We use an (at the time) high specification PC (Pentium4, 2.2 GHz
with 512 Mb RAM) with analog and digital input and output boards, controlled
by LabVIEW to provide this control. The system described in this section
provides a high level of accuracy and repeatability.

5.2 Hardware

Three National Instruments (NI) cards were used to interface with the experi-
ment. The cards were connected together by NI's proprietary RTSI (real time
synchronous interface) bus which allows for precise timing between the different
cards.

The card used to output all signals to the experiment was a digital card, the
PCI-DIO-32-HS:

- PCI→ PCI interface bus

- DIO → Digital Input-Output

- 32 → number of DIO lines

- HS → High Speed.

As suggested by the name, this card provides 32 high speed (20 MHz), digital input/output lines. No digital input lines were used on this card.

An analogue card, the PCI-6713 provided 8 channels for analog control. In the course of the experiment only one of these lines was used for accurate adjustment of the CO_2 AOM, to control the CO_2 laser power during initial alignment. However, the analog card was integral to the experiment as the clock on the card was used to synchronise the timing of the experiment. This clock is capable of 20 MHz resolution allowing the use of timesteps of 50 ns, which is much smaller than required in this experiment. The clock used can be any multiple of this base clock. The timestep used in the experiments discussed in this thesis was 10 μs.

The final card was the PCI–1408, used for image acquisition, IMAQ. Initially a next–generation card, the PCI–1409 was purchased, but was found after many problems to not be capable of interfacing with the CCD camera used. The main difference between the two image acquisition cards was that the PCI–1408 lacked a RTSI interface. However, as the camera and the image acquisition card are triggered externally from the digital card this was not required.

5.3 Software

To create the digital patterns and write them to the boards a program was written in LabVIEW (National Instruments, LabVIEW 7.0). LabVIEW is a graphical programming language developed for interfacing a PC or PC cards with external hardware. Its interface is based around a user–created front panel which is designed to mimic the front panel of a physical control box, with switches, toggles and dials, and a back panel which uses self-contained virtual instruments (VIs) and 'wires' to manipulate and direct data. LabVIEW is very different from any other computer language that had been used previously, but

its modular format and its powerful interfacing with hardware mean it is very adaptable to different problems.

When the experiment is started the code writes a time varying pattern for each of the digital output lines to the computer memory. One bit is written for each line at each of the timesteps defined by the clock. These outputs will be variously sent to various devices requiring switching, to trigger the image acquisition card or to level boxes to convert the digital voltages to other, pre–defined voltages, see Section. 5.4. When the full digital pattern is written to memory it is read out to the digital lines and runs independently of the computer for the read out stage. One of the digital lines is used to prepare the image acquisition card and another to take trigger the image acquisition of the atomic cloud at the end of the experimental run. This image is read into an array and analysed by the code to extract information about the spatial distribution of the atoms.
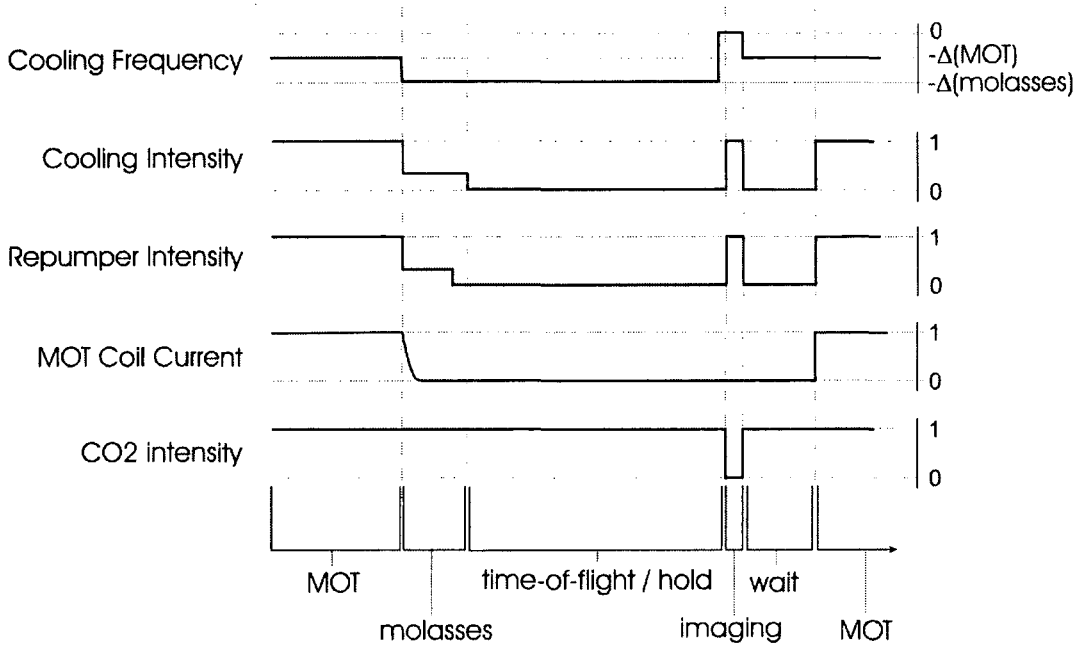
Figure 5.1: Graph of timing of the experiment (not to scale). The graph shows the desired experimental levels which are then controlled by one, or more, digital levels using the digital–level boxes (Section. 5.4).

5.4 Digital Level Boxes

A digital level box was designed and built in house based on a design brought to Durham by Simon Cornish. These circuits convert digital signals to other, predefined voltages. A chip (Maxim REF01) provides a +10 V voltage reference with low noise, 10 μV p–p. An op–amp inverter then provides a -10 V reference, with similar noise characteristics, due to the low noise on the op–amp. A potentiometer, referenced to these voltages allow a voltage level to be selected with precision limited by the resolution of the potentiometer. A digital switch (Maxim DG419) then allows selection between two such voltage levels. By combining two, or more, of these devices more levels can be switched between. Fig. 5.2 shows a general schematic of the circuit. The level boxes are primarily
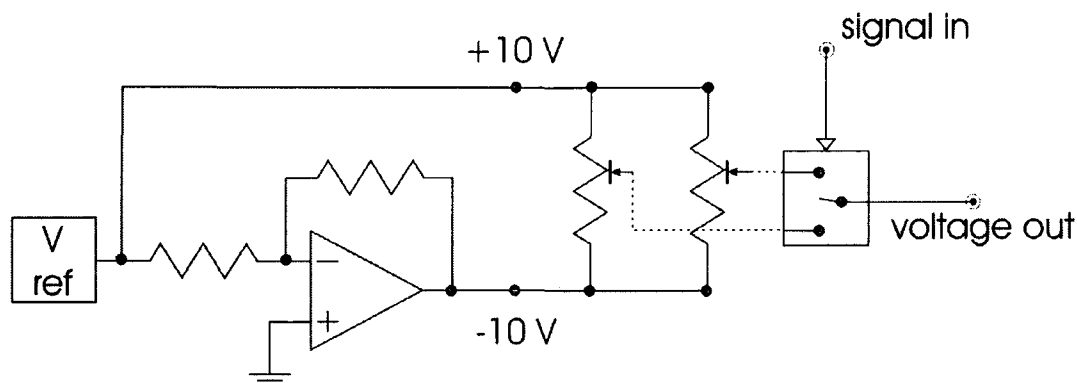
Figure 5.2: The digital level box circuit. The operation is described in Section. 5.4.

used for switching of AOMs between the various frequencies and laser intensities required for MOT, molasses and imaging.

5.5 Imaging

Fluorescence imagining was used for detection of the atomic cloud parameters at the end of an experiment. The MOT beams were tuned to resonance and were pulsed on, with the repumper beams, for an imagining time δt. The scattered photons were collected by a lens and imaged onto a CCD camera. The basic configuration is as shown in Fig. 4.15.

5.6 The Camera

Two cameras, both JAI-M50 models, were used in the experimental set-up. One camera was mounted directly above the vacuum chamber looking through a ZnSe window. ZnSe has a transmission of 65% at 780 nm. The other camera was mounted as close to the MOT region as possible, looking at an angle through the large viewports shown in Fig. 3.1.

An advantage of these cameras is that they can be triggered to take an image with a maximum jitter of 64 μs. As the imaging time is defined by the duration of the probe pulse a jitter on this level is very easily accommodated by triggering the probe pulse more than 64 μs after triggering the camera. A range of shutter open times are available on the camera, from 100 μs to 20 ms. However, using longer shutter times results in having many lost frames when transferring images from the camera to the IMAQ card. This effect has been noticed by others (Aidan Arnold in Strathclyde). For a camera shutter time of 20 ms, up to 4 out of every 5 frames are lost, which is clearly not acceptable. The effect is greatly lessened by using shorter shutter times. Using a camera shutter of 2 ms results in better than 90% of the frames being correctly transferred. For a camera shutter time of 200 μs, approximately 99% of the frames are transferred correctly. These were the two shutter speeds used, depending on the imaging pulse duration used.·

When the camera was used in triggered mode with the PCI-1409 IMAQ card, images were never captured. Over a period of 7 months a huge number of software and hardware fixes, many suggested by JAI and National Instruments, were tried until National Instruments admitted the limitations of their card and replaced the card for the PCI-1408 card that was originally requested. The problem, according to private communication with National Instruments was

> "One of the major differences that can cause a "Can't lock on video source" error for the PCI-1409 and not the PCI-1408 is due to variations in locking circuitry. For non-standard analog cameras, the PCI-1408 and PCI-1409 are designed to lock to these cameras in external lock mode. This means the camera's HSYNC, VSYNC, and pixel clock are supplied to the IMAQ board, which allows the board to bypass its locking circuitry and acquire the non-standard

images using the camera's timing signals instead of generating its own. The PCI-1408 could often times acquire from non-standard cameras without being in external lock mode because its locking circuitry was more flexible, but it didn't cover as wide a range of frequencies as the PCI-1409. The PCI-1409 supports standard, discrete locking frequencies that cover a wider range (including VCR), but for frequencies that aren't quite standard frequencies, it won't lock. Operating in External Lock mode will acquire non-standard images for both the PCI-1408 and PCI-1409."

Using the PCI–1408 IMAQ card removed these problems.

5.6.1 Calibration of Images

Spatial Calibration

A calibration image of a grid was taken to convert the spatial unit of the images from pixel sizes to μm. This give an effective pixel size of $22.5(\pm0.2)$ μm by $11.2(\pm0.2)$ μm.

Atom Number Calibration

To convert pixel counts to atom number the MOT was loaded with 10^7 atoms, as determined by the fluorescence captured on a photodiode. The MOT trapping fields were turned off and after a short delay a CCD image was taken of the cloud. The total pixel count of the image was summed. From the ratio of the atom number to integrated pixel number a value of 4 atoms per count, for a 50 μs imaging time, was evaluated. To ensure that the whole depth of the atom cloud was being observed a delay up to 10 ms was allowed between the release of the atomic cloud and imaging. The pixel/atom ratio remained the same, independent of the delay time.

5.6.2   Heating During Imaging

The absorption of resonant light will necessarily heat the cold atoms, and impart momentum onto the cloud. The effect of this is to blur the image taken. For imaging, the situation is identical as for an optical molasses with zero detuning [75]. If during the imaging pulse duration, δt, an atom scatters N photons then the root–mean–square velocity of the atom will change by

$$v_{\mathrm{rms}} = \sqrt{\frac{N}{3}}\, v_{recoil} \, , \qquad (5.1)$$

due to the isotropic emission of the absorbed photons [91]. This will cause a random displacement of

$$
\begin{aligned}
r_{\mathrm{rms}} &= \frac{v_{\mathrm{rms}}}{\sqrt{3}}\, \delta t \\
&= \frac{\sqrt{N}}{3}\, v_{recoil}\, \delta t \, .
\end{aligned}
\qquad (5.2)
$$

In the experiments an imaging time of 100 μs was used for the best signal to noise ratio. The scattering rate during this imaging for a total intensity of $I = 55$ mW/cm^2 is $\Gamma_{sc} = (\pi)5.5$ MHz, meaning that $N = \Gamma_{sc}\,\delta t = 1700$ photons are scattered. Using $v_{recoil} = 5.97$ mm/s for Rb, this results in $r_{\mathrm{rms}} = 8.1$ μm. The effect of this position spread is to blur the image. However this blurring is less than the pixel resolution and the effect on the image should not degrade the image taken any more than the pixelation inherent in the image.

Chapter 6

Optical Dipole Trapping

Atoms interacting with a light field experience both dispersive and dissipative forces. The latter is due to the absorption of photons from the field and subsequent spontaneous emission. This 'radiation pressure' force is used for laser cooling as the atom can lose energy through the spontaneous emission process. The dispersive component of atom–light interactions is due to the interaction of the light field with the induced dipole moment of the atom. The effect of this interaction is a shift in the energy of atomic states - the ac–Stark shift [19]. For near resonant conditions, as in the MOT and optical molasses, the dissipative part dominates. For large detunings of the light field from atomic resonances the dispersive part dominates and the absorption–spontaneous emission processes can be neglected, giving a truly conservative force. However, the interaction is weak, where traps on the order of 1 mK deep are considered deep.

6.1   Dipole Force due to the Induced Dipole Moment

An atom in a laser field has a dipole moment, $\mathbf{d}$ induced by the electric field, $\mathcal{E}$. The dipole moment oscillates at the frequency of the driving field, and is closely related to the field by

$$\mathbf{d} = \alpha(\omega)\mathcal{E} \ , \tag{6.1}$$

where α is the complex polarizability. The dipole potential due to this interaction is given by

$$V_{\text{dipole}} = -\frac{1}{2} \langle \mathbf{d} \cdot \mathcal{E} \rangle \qquad (6.2)$$

$$= -\frac{1}{2\,\epsilon_0\,c}\,\alpha\,I \ . \qquad (6.3)$$

The angular brackets indicate that we take the time average, and the intensity of the laser field is given by

$$I = \frac{1}{2}\,\epsilon_0\,c\,|\mathcal{E}|^2 \ . \qquad (6.4)$$

In Eqn. 6.3 we should write $\Re(\alpha)$ in favour of α as we look at the in–phase component of the force. However, in this work we will only consider the real part of α and so will keep this notation.
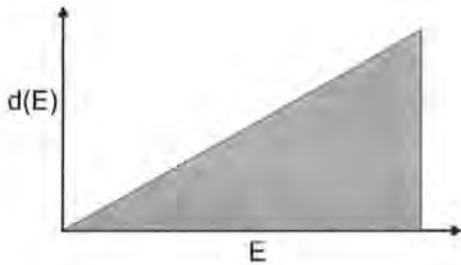
Figure 6.1: Illustration showing that the energy of the dipole is $\frac{1}{2}\,\mathbf{d} \cdot \mathbf{E}$ if the dipole moment is proportional to the driving field.

.5The factor of $\frac{1}{2}$ in Eqn. 6.2 comes about due to the dipole moment being induced, and not permanent. Assuming the atom has a linear response to the field, as in Eqn. 6.1, we can write the instantaneous electrostatic energy as [92]

$$V_{inst} = \int_0^{\mathcal{E}} -\mathbf{d}(\mathcal{E}) \cdot \delta\mathcal{E} \qquad (6.5)$$

$$= -\frac{1}{2}\,\mathbf{d} \cdot \mathcal{E} \ . \qquad (6.6)$$

This can be seen in the figure on the left, where the energy required to create the dipole is shown graphically. For an ac–field the time average of this must be taken which leads directly to Eqn. 6.2.

While Eqn. 6.3 is identical to Eqn. 6.2, it has the advantage of clearly separating the interaction into an atom part, α, and a field part, $|\mathcal{E}|^2$. We do note that α is still a function of the frequency of the E-field.

6.2   Spatially Trapping with the Optical Dipole Force

The dipole force occurs due to gradients in the light field,

$$F_{\text{dipole}} = -\nabla V_{\text{dipole}}$$

$$= \frac{1}{2\,\epsilon_0\,c}\,\alpha\,\nabla I\;. \tag{6.7}$$

If the frequency of the driving field is below that of an atomic resonance then **d** will be in phase with **E** and, from Eqn. 6.1, α will be positive. Thus 3D confinement can be realised in the simple geometry of a focussed laser beam that is red–detuned from an atomic resonance, as was proposed by Ashkin in 1978 [16]. The form of this potential about the laser focus is shown in Fig. 6.2. In this arrangement the focus provides a local maximum in intensity axially along the beam and the Gaussian radial profile provides radial confinement. The general equation for a focussed Gaussian beam of peak intensity I_0 is

$$I(z,r) = I_0\,\frac{w_0}{w^2(z)}\,\mathrm{e}^{-2r^2/w^2(z)}, \tag{6.8}$$

where $w(z)$ is the $1/e^2$ radius at z and r is the radial position. The variation of w along the beam axis is given by

$$w(z) = w_0\sqrt{1 + \left(\frac{z - z_0}{z_R}\right)^2}, \tag{6.9}$$

where

$$z_R = \frac{\pi w_0^2}{\lambda} \tag{6.10}$$

is the Rayleigh length and z_0 is the location of the beam focus where $w(z) = w_0$, the minimum spot size. Knowing that the potential in a dipole trap is proportional to the intensity we find an equation of the same form,

$$U(z,r) = -U_0\,\frac{w_0^2}{w(z)^2}\,\mathrm{e}^{-2r^2/w^2(z)}, \tag{6.11}$$

where U_0 is the minimum of the trap.

6.3   Derivation of the Light Shift

Existing literature attempts to find a form of the interaction of light with an induced dipole by making use of of Lorentz's classical oscillator model [18]. This
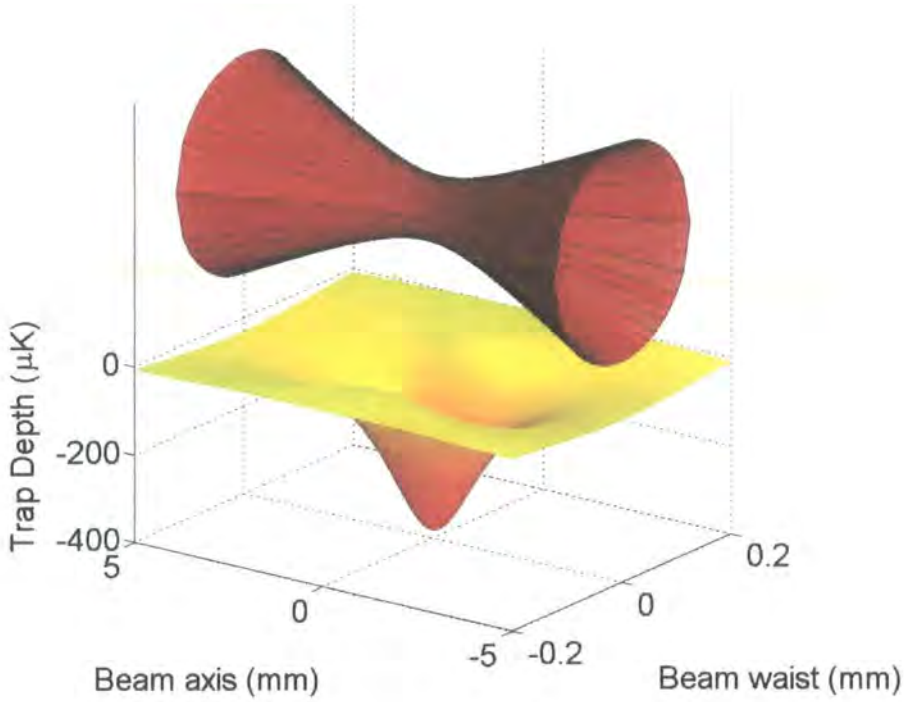
Figure 6.2: Form of the potential of an optical dipole trap at the focus of a red–detuned laser, shown schematically above the potential surface. The specific example here is for Rb atoms at the focus of a 50 W, CO_2 laser ($\lambda = 10.6\ \mu m$) focussed to a waist of 71 μm.

approach considers the valence electron to be bound elastically to the core with an oscillation eigenfrequency ω_0. Dampening is included by dipole radiation due to the accelerating electron.

This model does have the advantages of simplicity and makes use of known results of classical electrodynamics theory but a more rigorous approach is taken in the next sections to get a similar result without making gross assumptions.

6.3.1   Time Dependent Perturbation Theory

We begin with the Schrödinger equation

$$i\hbar\frac{\mathrm{d}}{\mathrm{d}t}|\Psi(t)\rangle = (H_a + V(t))|\Psi(t)\rangle , \tag{6.12}$$

where H_a is the atomic Hamiltonian and $V(t)$ is the interaction of the atom with a monochromatic radiation field as a perturbation, given by

$$V(t) = -\mathbf{d} \cdot \mathcal{E} \cos(\omega t) \ . \tag{6.13}$$

Here

$$\mathbf{d} = -e\,\mathbf{r} \tag{6.14}$$

is the dipole moment of the atom, with e the electronic charge and $\mathbf{r}$ is the displacement of the electron from the atomic centre of mass. This model assumes a single valence electron; for a multi–electron system the dipole moment is a sum over the individual moments. $\mathcal{E}$ is the electric field vector. We also introduce the Rabi frequency, Ω,

$$\Omega = \langle i|\mathbf{d}|f\rangle \frac{\mathcal{E}}{\hbar} \ , \tag{6.15}$$

where $\langle i|\mathbf{d}|f\rangle$ is the dipole moment between states $|i\rangle$ and $|f\rangle$. We expand the wavefunctions, which form a complete set, in the concise Dirac notation

$$|\Psi(t)\rangle = \sum_i c_i \, |i\rangle \, \mathrm{e}^{-i\omega_i t} \ . \tag{6.16}$$

We can further simplify the situation to only consider two atomic states, which will be labelled $|1\rangle$ and $|2\rangle$. Substituting Eqns. 6.13 and 6.16 into Eqn. 6.12 leads to

$$i\dot{c}_1 = \Omega \cos(wt) \, \mathrm{e}^{-i\omega_0 t} c_2 \tag{6.17}$$

$$i\dot{c}_2 = \Omega \cos(wt) \, \mathrm{e}^{i\omega_0 t} c_1 \ , \tag{6.18}$$

where $\omega_0 = (\omega_2 - \omega_1)$. We re-write these equations in a more convenient form,

$$i\dot{c}_1 = c_2 \, \frac{\Omega}{2} \left(\mathrm{e}^{i(\omega - \omega_0)t} + \mathrm{e}^{-i(\omega + \omega_0)t} \right) \tag{6.19}$$

$$i\dot{c}_2 = c_1 \, \frac{\Omega}{2} \left(\mathrm{e}^{i(\omega + \omega_0)t} + \mathrm{e}^{-i(\omega - \omega_0)t} \right) \ . \tag{6.20}$$

For near resonant fields we would now make the rotating wave approximation (RWA), dropping terms that oscillate at $\omega + \omega_0$, known as the counter–rotating terms. By this step we can quickly come to the energy shift of the states as,

$$\Delta E_{\mathrm{RWA}} = \pm \frac{\hbar\Omega^2}{4\Delta} \ , \tag{6.21}$$

where $\Delta = \omega - \omega_0$. This derivation is performed step–by–step in Appendix B.

For very large detunings, such as will be looked at in these experiments, $\omega \ll \omega_0$, so $\omega - \omega_0 \approx \omega + \omega_0$ and the counter–rotating terms in Eqns. 6.19 and 6.20 must be kept. There is then no analytical solution for the energy shifts of the states in Eqns. 6.19 and 6.20.

6.3.2 Floquet Theory

Using perturbation theory the form of the light–shift potential can be derived. The full derivation is in Appendix C, but the basic details are included here.

Again we consider an atom in a monochromatic field and use the time–dependent Schrödinger equation Eqn. 6.12 with perturbation Eqn. 6.13 as before.

The perturbation, $V(t)$ is separated into two parts

$$V(t) = V_+ \, e^{-i\omega t} + V_- \, e^{i\omega t} \,, \tag{6.22}$$

where it is evident that

$$V_+ = V_- = \frac{\hbar \Omega}{2} \,. \tag{6.23}$$

It must be arranged that $V_+ = V_-^*$.

The Floquet method involves rewriting

$$|\Psi(t)\rangle = e^{-iEt/\hbar}|\psi(\tau)\rangle \,. \tag{6.24}$$

Following for the formulation of Potvliege *et al.* [93] we examine the coupled, time–independent "Floquet equations" which lead to a second–order shift

$$
\begin{aligned}
E^{(2)} &= \frac{\langle e|V_+|g\rangle}{E_0 - \hbar\omega - E_2} + \frac{\langle e|V_-|g\rangle}{E_0 + \hbar\omega - E_2} \\
&= -\frac{|\langle e|V_+|g\rangle|^2}{\hbar} \left(\frac{1}{\omega - \omega_0} + \frac{1}{\omega + \omega_0} \right) \,.
\end{aligned}
\tag{6.25}
$$

From the earlier definitions of Eqns., 6.15 and 6.23 the light–shift is

$$E^{(2)} = \frac{\hbar \Omega^2}{4} \left(\frac{1}{\omega_0 - \omega} + \frac{1}{\omega_0 + \omega} \right) \,. \tag{6.26}$$

This result agrees with the result from the Grimm *et al.* review article, derived using a classical oscillator model [18].

6.4 Transitions in Multilevel Atoms

As was derived above, the Stark shift of an atomic state $|i\rangle$ coupled to another state $|f\rangle$ is given by

$$V = -\frac{\hbar\Omega^2}{4\Delta_{eff}} \, , \tag{6.27}$$

with

$$\frac{1}{\Delta_{eff}} = \left(\frac{1}{\omega_{if} - \omega} + \frac{1}{\omega_{if} + \omega} \right) \, . \tag{6.28}$$

Substituting the Rabi frequency, Eqn. 6.15 into Eqn. 6.27 and including all allowed transitions from $|i\rangle$ we get an expression for the energy shift of level $|i\rangle$

$$\Delta E_i = -\frac{\mathcal{E}^2}{4\hbar} \sum_{f \neq i} |\langle i|\mathbf{d}|f\rangle|^2 \frac{1}{\Delta_{eff}} \, , \tag{6.29}$$

where the sum is over all states $|f\rangle$ except the initial state.

The transition matrix elements $\langle i|\mathbf{d}|f\rangle$ will be a function of the quantum numbers n, J, F, m_F of both the initial and final states and also of the polarisation ϵ of the laser field, where $\epsilon = 0, \pm1$ for π and $\sigma^\pm$ transitions, respectively. Using the Wigner–Eckart theorem [94], the matrix elements can be decomposed into the product of a Clebsch–Gordan coefficient $\langle F, m_F|F', 1, m'_F, \epsilon\rangle$ and a reduced matrix element $\langle F||\mathbf{d}||F'\rangle$

$$\langle i|\mathbf{d}|f\rangle = \langle F, m_F|F', 1, m'_F, \epsilon\rangle \, \langle F||\mathbf{d}||F'\rangle \tag{6.30}$$

$$= C_{if} \, \langle F||\mathbf{d}||F'\rangle \, . \tag{6.31}$$

The reduced matrix element can be simplified further into a fully reduced matrix element that is then only a function of the fine structure state [95, 96]

$$\langle F||\mathbf{d}||F'\rangle = \langle J||\mathbf{d}||J'\rangle(-1)^{F'+J+1+I}\sqrt{(F'+1)(2J+1)} \left\{ \begin{array}{ccc} J & J' & 1 \\ F' & F & I \end{array} \right\} \, . \tag{6.32}$$

The remaining fully reduced matrix element can be expressed in terms of the Einstein A coefficient or lifetime of the transition, τ, between the J states by [97]

$$A_{if} = \frac{1}{\tau_{if}} = \frac{\omega_{if}^3}{3\pi\epsilon_0\hbar c^3} \frac{2J+1}{2J'+1} |\langle J||\mathbf{d}||J'\rangle|^2 \, . \tag{6.33}$$

Then, using Eqns. 6.31–6.33 in Eqn. 6.29, we derive a general expression for the
light–shift of any atomic, hyperfine state $|J, F, m_F\rangle$,

$$\Delta E_i = \frac{3\pi c^2 I}{2} \sum_{f \neq i} \frac{A_{if}}{\omega_{if}^3} (2J' + 1)(2F' + 1) \left\{ \begin{array}{ccc} J & J' & 1 \\ F' & F & I \end{array} \right\}^2 \frac{C_{if}^2}{\Delta_{eff}} . \quad (6.34)$$

In the situation of unresolved hyperfine structure the light–shift can be written
in the simpler form

$$\Delta E_i = -\frac{\mathcal{E}^2}{4\hbar} \sum_J \frac{|\langle Jj|\mathbf{d}|J'\rangle|^2}{\Delta_{if}} \sum_{m'_J} |\langle J, m_J|J', 1, m'_J, \epsilon\rangle \quad (6.35)$$

$$= \frac{3\pi c^2 I}{2} \sum_{f \neq i} \beta \frac{A_{if}}{\omega_{if}^3} \left(\frac{1}{\omega_{if} - \omega} + \frac{1}{\omega_{if} + \omega} \right) . \quad (6.36)$$

The last equation has been written so that β contains the prefactors that are
due to the atomic states other than the experimentally measurable quantities
A_{if} and ω_{if}.

Thus it seems that in order to calculate the light–shift of any energy level, i
the only requirements are the Einstein A coefficients for the possible transitions
and also the frequency of each of those transitions. Using the Kurucz line data
[98], it is possible to get data for transitions up to $5s \rightarrow 10p$ and $5p \rightarrow 11s, 4d$
lines.

There is some concern as there is no estimate of the error in any of the pa-
rameters given from this database. Most of the data given is from theoretical
calculations. One of the main references for the Rb data on the database warns
against comparison with experimental data, though this is due to *"very large
disagreements among the observed data"* [99]. It does claim a better than 10 per
cent agreement between calculations and measured lifetimes. Other references
claim significant disagreement with the results of Warner [100]. However, the
energies of the states given in the Kurucz database agree with those distributed
by NIST to better than 0.1% [101]. With these caveats in mind, our initial light
shift calculations were of this form, due to the simplicity of the calculations.

Care must be taken when evaluating Eqn. 6.36 to avoid over–weighting the
contribution of particular states. This problem arises as the quoted Einstein
A values sometimes have the β prefactors absorbed, and sometimes not. In
general it seems that linestrength factors have been included, whereas the $(2J'+$

$1)/(2J + 1)$ terms have not. Then for transitions from the ground $S_{1/2}$ state to $P_{3/2}$ and $P_{1/2}$ states a weighting of 3:2 is included in calculations. Similarly, transitions to $d_{5/2}$ and $d_{3/2}$ from the $p_{3/2}$ are weighted 5:3.

In general, only a few states contribute to the gross light–shift away from a few nm about transition wavelengths. Fig. 6.3 shows that the D2 and D1 lines, from $5^2 S_{1/2}$ to $5^2 P_{3/2}$ and $5^2 P_{1/2}$ respectively, form the strongest contributions to the light-shift of the ground state in Rb. More terms are required to calculate the light-shift of the $5^2 P_{3/2}$ state, Fig. 6.4. The first thing to be noted from this figure is that the shift due to the $5^2 S_{1/2}$ state is opposite in sign from all other shifts. This is to be expected from the dressed state model, where in a two level system the light–shifts of the two states are equal in magnitude, but opposite in direction.
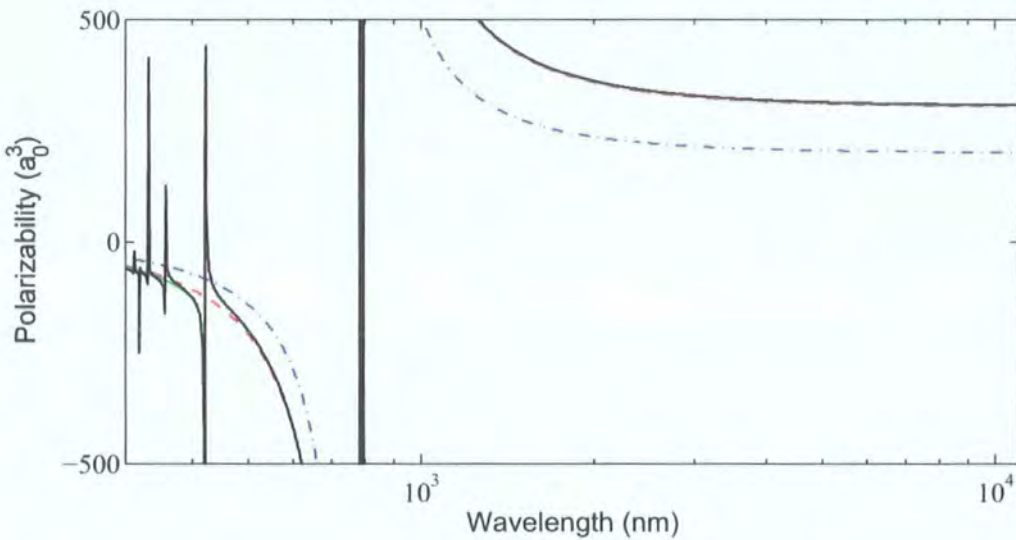
Figure 6.3: The contribution of various lines to the light-shift of the $5^2 S_{1/2}$ ground state of Rb as a function of laser wavelength for a laser of intensity of 1 MW/cm^2. The dot–dashed line is the shift due to the $5^2 P_{3/2}$. After the inclusion of the $5^2 P_{3/2}$ line (red dash) the other transition make negligible contribution away from the wavelength of the transition. The black solid line is due to the 12 strongest transitions from $5^2 S_{1/2}$ found in [98].
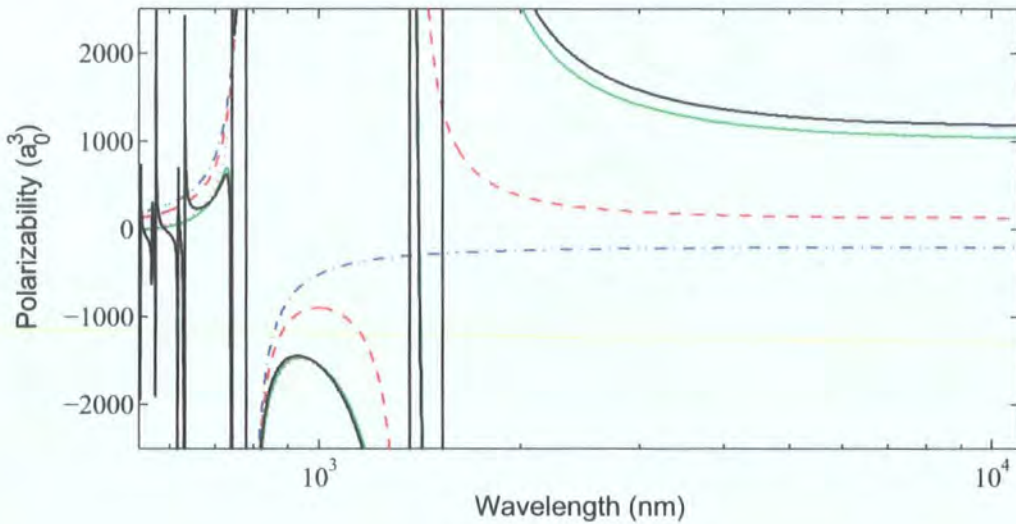
Figure 6.4: The contribution of various lines to the light-shift of the $5^2P_{3/2}$ state of Rb as a function of laser wavelength for a laser of intensity of 1 MW/cm^2. The lines are most easily identified at long wavelengths. From bottom (blue dot–dash) $5^2S_{1/2}$, (red dash) as above plus $6^2S_{1/2}$, (green solid) as above plus $7^2S_{1/2}$. The solid black line is the contribution of the 17 strongest lines from $5^2P_{3/2}$ [98].

6.5   Comparison of Methods

It is useful to plot the various methods of calculating ground– and excited–state light–shifts in order to see that there are not any gross deviations between results in the limits considered. Here we will preempt our main approach at solving the light–shift problem, and compare the light–shifts calculated from Eqn. 6.36 with results using theoretical polarizabilities in Eqn. 6.3 [29]. These data are plotted in Fig. 6.5. For the ground state, the calculations agree to better than 8% at the CO$_2$ and Nd:YAG wavelengths. For the excited states the results differ by $\sim 35\%$ at both wavelengths. The theoretical values at the CO$_2$ wavelength agree well with other results [102].
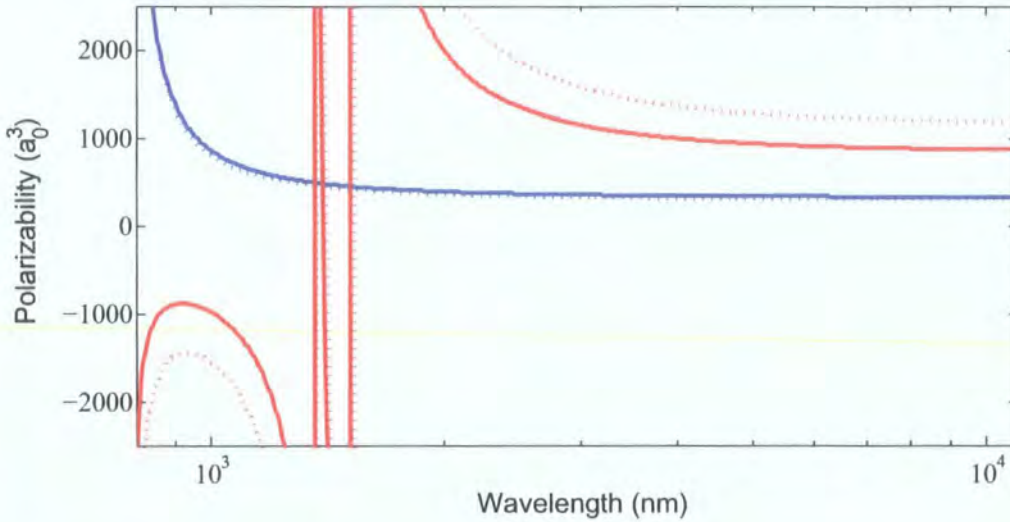
Figure 6.5: Comparison of light-shifts of the $5^2S_{1/2}$ (blue) and $5^2P_{3/2}$ (solid red) states of Rb calculated using different methods. The dotted lines are calculated from Eqn. 6.36 using data from [98]. The solid lines are the results from calculations of polarizabilities of the same states [29]. The calculations for the $5^2S_{1/2}$ in excellent agreement. The agreement is still reasonable for the $5^2P_{3/2}$ state, as the form is clearly similar. All calculations are for an intensity of 1 MW/cm^2.

6.6 Polarizability Formation

Evaluation of the light–shift by summing over all possible transitions requires tables of Einstein A coefficients and transition wavelengths. This is unsatisfactory as the information is coming second–hand from the Kurucz database [98], which is the standard method of these calculations. This means that there is no information on the quality of the data used, or whether the data is experimental or theoretical. Furthermore, as will be shown in this section, calculation by this method fails to give us the tensorial features of the light–shifts of some states.

6.6.1 Formulation

Schmieder [103], following from Angel and Sandars [20] shows that the polarizability in Eqn. 6.1, α is actually a sum of two terms

$$\alpha = \alpha_0 \, \mathbb{1} + \alpha_2 \, \mathsf{Q} \ , \tag{6.37}$$

where α_0 is the *scalar polarizability*, $\mathbb{1}$ is the identity matrix, α_2 is the *tensor polarizability* and $\mathbf{Q}$ is an operator that involves the coupling of the atomic angular momentum $\mathbf{J}$ to the electric field direction [103]

$$\mathbf{Q} = \frac{3(\mathbf{u} \cdot \mathbf{J})^2 - J(J+1)}{J(2J+1)} \,, \tag{6.38}$$

with $\mathbf{u}$ the unit vector in the electric field direction.

The matrix elements of $\mathbf{Q}$ between two hyperfine states are given by [103]

$$
\begin{aligned}
\langle F\,m_F|\mathbf{Q}|F'\,m_F'\rangle = {}& \sqrt{\frac{15}{2}} \left[\frac{(J+1)(2J+1)(2J+3)}{J(2J-1)} \right]^{1/2} \\
& \times \sum_q \sum_{\mu=-1}^{1} \sum_{\mu'=-1}^{1} u_\mu u_{\mu'} \begin{pmatrix} 1 & 2 & 1 \\ \mu & -q & \mu' \end{pmatrix} \\
& \times (-1)^{I+J+F-F'-M_F} \sqrt{2(F+1)(2F'+1)} \\
& \times \begin{pmatrix} F & 2 & F' \\ M_F & q & -M_F' \end{pmatrix} \begin{Bmatrix} F & 2 & F' \\ J & I & J \end{Bmatrix}.
\end{aligned}
\tag{6.39}
$$

In this equation $u_{-1} = (u_x - iu_y)/\sqrt{2}$, $u_0 = u_z$, and $u_1 = -(u_x + iu_y)/\sqrt{2}$ are the spherical tensor components of $\mathbf{u}$. The 3-j symbols impose the requirements that $q = \mu + \mu' = M_F' - M_F$. It must be noted that q is defined by the summation of μ and μ', not the other way around.

If the electric field is aligned along z, then $u_z = 1$ and is the only non-zero term of the electric field tensor. This means, from Eqn. 6.39 that $\mu = \mu' = 0$ and therefore $q = 0$. As would be expected in a linearly polarised field m_F is then only coupled to $m_F' = m_F$. We then construct a matrix that is diagonal in m_F and with rows and columns for each m_F labelled by F and F' respectively. The matrix shown in Eqn. 6.40 illustrates the form of this matrix for ^{87}Rb, with $I = \frac{3}{2}$ and $J = \frac{3}{2}$. The labeling of the matrix is shown in Fig. 6.6.

$$
\begin{pmatrix}
\| & & & & & & & & & \\
 & \| & \| & & & & & & & \\
 & \| & \| & & & & & & & \\
 & & & \| & \| & \| & & & & \\
 & & & \| & \| & \| & & & & \\
 & & & \| & \| & \| & & & & \\
 & & & & \| & \| & \| & \| & & \\
 & & & & \| & \| & \| & \| & & \\
 & & & & \| & \| & \| & \| & & \\
 & & & & \| & \| & \| & \| & & \\
 & & & & & & \| & \| & \| & \\
 & & & & & & \| & \| & \| & \\
 & & & & & & \| & \| & \| & \\
 & & & & & & & & \| & \| \\
 & & & & & & & & \| & \| \\
 & & & & & & & & & \|
\end{pmatrix}
\tag{6.40}
$$

Figure 6.6: Form of the $\langle F\, m_F | \mathbf{Q} | F'\, m'_F \rangle$ matrix.

6.6.2 Hyperfine Interactions

Up to this point we have neglected the hyperfine interaction, V_{hfs}. As we wish to calculate the energy levels of real atomic systems, such as ^{85}Rb and ^{87}Rb, we must find energy shifts due to the combined interactions of $V + V_{hfs}$. The hyperfine interaction is given by the operator [104]

$$V_{hfs} = \hbar A \, \mathbf{I} \cdot \mathbf{J} + \hbar B \, \frac{6 \left(\mathbf{I} \cdot \mathbf{J} \right)^2 + 3 \mathbf{I} \cdot \mathbf{J} - 2I(I+1)J(J+1)}{2I(2I-1)2J(2J-1)} , \tag{6.41}$$

where A and B are the hyperfine structure constants. For the $5P_{3/2}$ states of ^{85}Rb, $A = 25.009$ MHz and $B = 25.88$ MHz [105]. The non–zero matrix elements of Eqn. 6.41 are written as

$$\langle F \, m_F | V_{hfs} | F \, m_F \rangle = -\frac{1}{2} A \, K + \hbar B \, \frac{\frac{3}{2} K(K+1) - 2I(I+1)J(J+1)}{2I(2I-1) \, 2J(2J-1)} , \tag{6.42}$$

where

$$K = F(F+1) - I(I+1) - J(J+1) . \tag{6.43}$$

In this basis, the operator V_{hfs} will be diagonal.

6.6.3 Scalar and Tensor Polarizabilities

The scalar (α_0) polarizability is the average of the dipole polarizabilities, α_{xx}, α_{yy} and α_{zz} for an atom in a laser field polarized, respectively, in the x, y and z–directions [102]:

$$\alpha_0 = \frac{\alpha_{xx} + \alpha_{yy} + \alpha_{zz}}{3} . \tag{6.44}$$

The scalar polarizability is the same for all m_F values of the states concerned. The tensor (α_2) polarizability of a P state is given by [102]

$$\alpha_2 = \frac{\alpha_{xx} - \alpha_{zz}}{3} . \tag{6.45}$$

The values for the dipole polarizabilities are taken from Griffin *et al.* [29]. For a state with $J = 1/2$ the situation is simplified by symmetry, $\alpha_{xx} = \alpha_{yy} = \alpha_{zz}$ such that α_2 is then zero. For a P state $\alpha_{xx} = \alpha_{yy}$ and $|\alpha_{zz}|$ is typically larger than the other components. The values of the dipole, scalar and tensor polarizabilities for the $5P_{3/2}$ state are plotted in Fig.6.7.
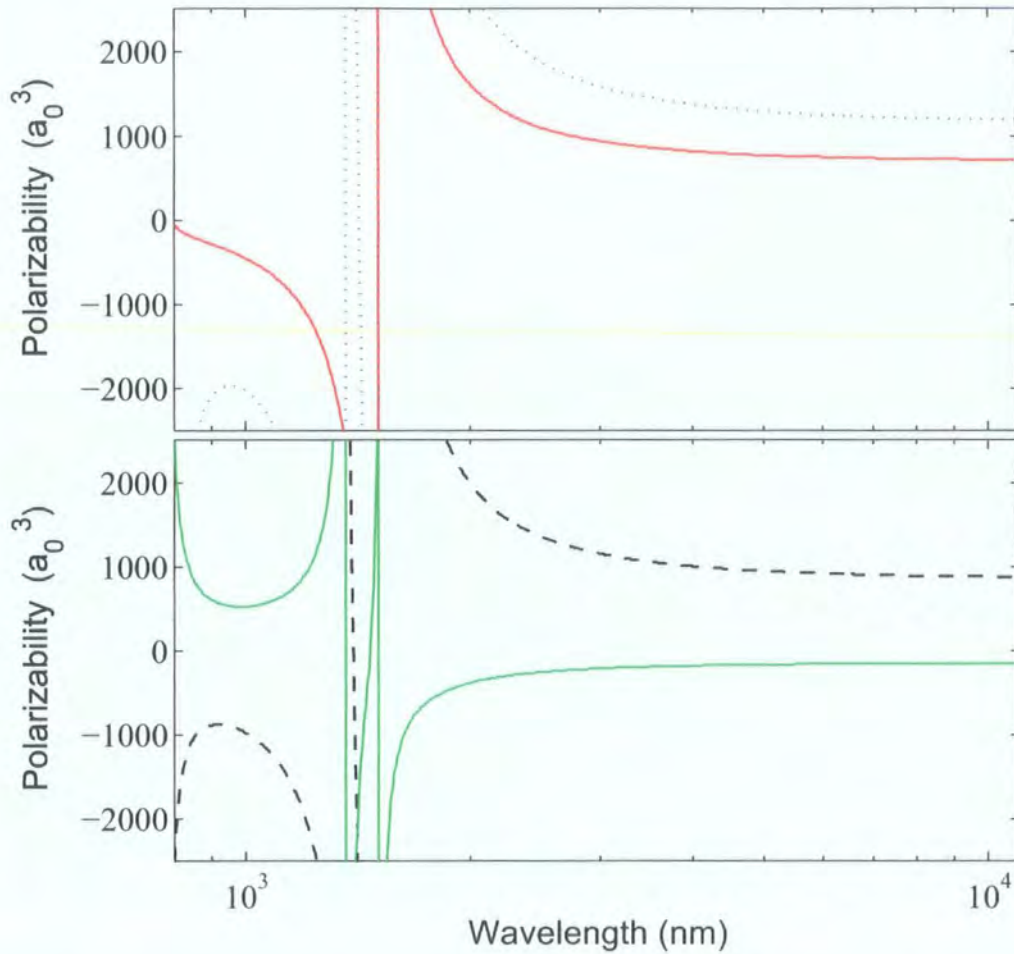
Figure 6.7: (**top**) Calculated dipole polarizabilities of $5p\,^2P_{3/2}$ state of Rb. For the $P_{3/2}$ state $\alpha_{xx} = \alpha_{yy}$, shown as dotted blue line. α_{zz} is the solid red line. (**bottom**) The scalar and tensor polarizabilities for the $5P$ state $\alpha_0 = (\alpha_{xx} + \alpha_{yy} + \alpha_{zz})\,/3$ (black dashed) and $\alpha_2 = (\alpha_{xx} - \alpha_{zz})\,/3$ (green solid), respectively. For the $5S$ state, $\alpha_0 = \alpha_{xx} = \alpha_{yy} = \alpha_{zz}$, as shown in Fig. 6.5, and $\alpha_2 = 0$.

6.7 Evaluating Energy Level Shifts

To calculate the energy level shifts we must find the eigenvalues of the matrix

$$V_{tot} = V_{hfz} + (\alpha_0\,\mathbb{1} + \alpha_2\,\mathsf{Q})\,\frac{I}{2\epsilon_0\,c}\,. \tag{6.46}$$

Solving Eqn. 6.46 was performed using Mathematica 4.1. The values of α_0 and α_2 were taken from the theoretical calculations described in [29]. When
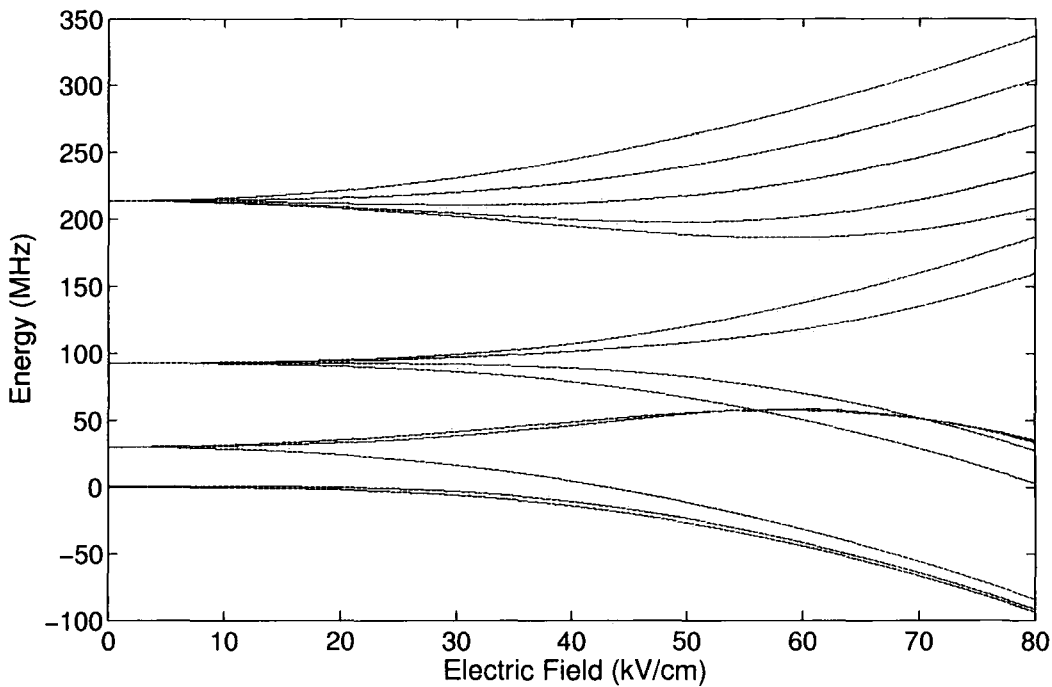
Figure 6.8: Quadratic Stark effect on the $5^2P_{3/2}$ state of ^{85}Rb. At zero applied field the fine structure state is split into the hyperfine states $F = 4, 3, 2, 1$ by the perturbation V_{hfs}. At relatively low E–fields the hyperfine states are split according to $|m_F|$ by the atom–field interaction. At stronger fields the $|m_J|$ levels become separated. The $-\frac{1}{2}\alpha_0\mathcal{E}^2$ shift, common to all levels, has been removed from this plot.

calculating light–shifts of a state the scalar polarizability terms were generally left from the calculation as these are merely a multiple of the unit matrix. All hyperfine states of a fine structure state will be shifted by $-\frac{1}{2}\alpha_0\,\mathcal{E}^2$.

The light–shifts calculated from diagonalising Eqn. 6.46 should be independent of the orientation of the electric field in Eqn. 6.39. Comparing results calculated for orthogonal fields was then the first test that the codes were working.

6.8   Differential Light–Shifts

From Fig. 6.5 we see that the scalar polarizability of the $5P_{3/2}$ state is signifi-cantly larger than that of the $5S_{1/2}$ in the static E–field limit. This has a con-siderable effect on the operation of the cooling and trapping fields in the MOT
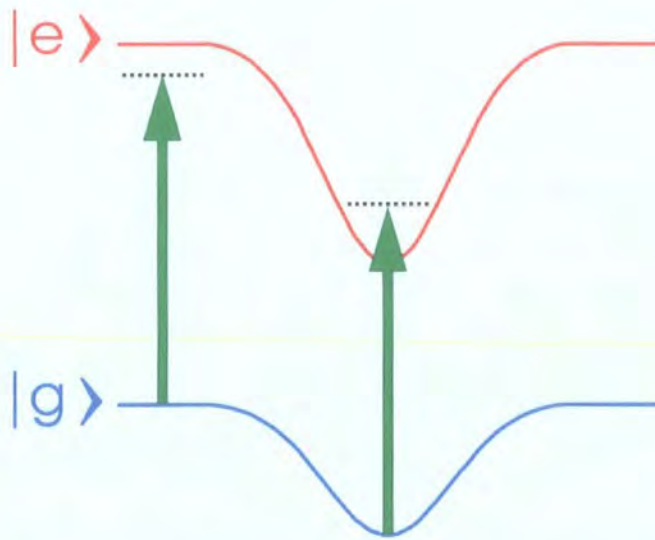
Figure 6.9: Effect on the laser–cooling states of the differential light–shift in an optical–dipole trap. The arrow represents the frequency of the cooling light. In the presence of the optical–dipole trapping field the cooling lasers becomes blue–detuned with respect to the atomic transition.

as the energy levels involved in laser cooling are shifted by different amounts, as shown in Fig. 6.9. At the centre of the optical lattice in our experiments that the differential light–shift, shown in Fig. 6.10, is ~ 60 MHz$= 10 \; \Gamma$. If the CO_2 laser trap is overlapped with a MOT, where detunings of the cooling light of $\sim -2 \; \Gamma = -12$ MHz are typical, then atoms in regions of significant ground–state trap depth will experience an effective detuning of ~ -50 MHz and will be heated from the trap.
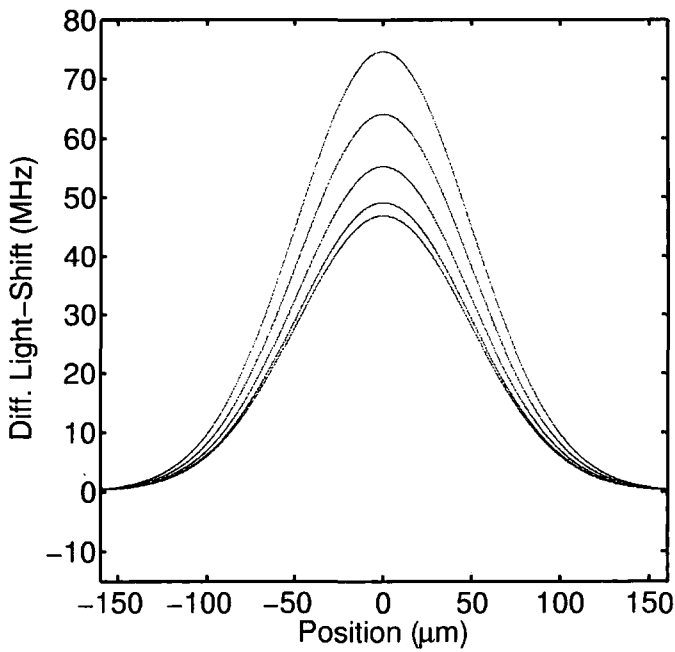
Figure 6.10: The differential light–shift of the $5^2 P_{3/2}$, $F = 4$ and $5^2 S_{1/2}$ $F = 3$ states of ^{85}Rb in a CO_2 laser dipole trap. Trap parameters are $P = 4 \times 45$ W of power (an optical lattice) focussed to $w_0 = 70$ μm. The ground state light–shift is $U_0/h = -36$ MHz. The mean of the differential light–shifts at trap centre is 57 MHz.

Chapter 7

Implementing a CO_2 Laser Dipole Trap

7.1 Introduction

In the previous chapter it was shown that the depth of an optical dipole trap is proportional to the intensity of the laser, and to a good approximation, inversely proportional the the detuning from resonance, Eqn.6.21,

$$U_0 \propto \frac{I}{\Delta} \,. \tag{7.1}$$

Furthermore, the scattering of trapping lights scales approximately as [18]

$$\Gamma_{sc} \propto \frac{I}{\Delta^2} \,. \tag{7.2}$$

For these reasons it is desirable to use a high powered, very far detuned laser for optical dipole trapping.

A CO_2 laser satisfies the requirements of large detuning and high power required for optimal optical dipole trapping, as discussed in Chapter. 6. A CO_2 laser typically operates at $\lambda = 10.6$ μm which is 13.6 times greater than the cooling transition in Rb at 780 nm. This difference means that for an induced dipole moment the electric field of a CO_2 laser appears to be quasi-electrostatic. A CO_2 laser can produce large and very stable powers [106, 107].

7.2 The Laser

For the experiments described in this thesis a Coherent-DEOS, GEM100 Select CO_2 laser was acquired. In this section we consider the operation and application of a CO_2 laser for stable trapping of laser-cooled atoms.

7.2.1 Considerations

Early experiments in very far–off resonance lasers (more than 100 nm from resonance) observed that the lifetime of the dipole traps was very much less than expected from either background collisions or from predicted photon scattering from the trapping laser. Adams *et al.* trapped sodium in a Nd:YAG laser trap, which has a wavelength approximately twice that of the cooling transition in Na. They observed trap lifetimes of 0.8 s, in comparison with predicted, vacuum limited lifetimes of 14 s [78].

The Thomas group at Duke has done much work on identifying heating mechanisms in optical dipole traps [108, 109]. A theoretical investigation of the situation identified intensity fluctuations as the dominant contribution to the heating of the trapped atoms [108]. Considering that the the trap frequency is related to the trap depth, U and laser intensity, I by

$$\omega_{osc} \propto \sqrt{U}$$
$$\propto \sqrt{I}, \tag{7.3}$$

it is evident that changes in the intensity will parametrically heat the trapped atoms. The heating rate is predicted to be exponential with time, as the hotter atoms will be heated more. In order to obtain background limited lifetimes it is indicated that the intensity fluctuations must be reduced to below 0.1% of I_0 [110].

Measurements taken by Gehm have shown that the Coherent-DEOS laser exhibits very low intensity fluctuations [111]. For trap frequencies of up to 7 kHz, exponential heating rates of $< 10^{-4}$ Hz were measured. This extremely low heating rate was a main consideration in the selection of our laser.

7.2.2 Power Stability

As was discussed in Section 7.2.1, the power stability of the dipole trapping laser is of great importance. The power meter used in this experiment could not give the resolution required to measure power fluctuations on the order of 0.1%. The response time of the power meter is also on the order of 1 s, meaning that even relatively low frequency fluctuations could not be measured. However, the lifetime of the trapped atoms would give an excellent indication of the beam quality. It was desirable to know how long it would take the laser to get into stable operation, when the large drifts due to turn on effects (such as temperature stabilisation) would settle down. Measurements of the power were taken directly after the laser head over a period of 2 hours, as plotted in Fig. 7.1. The power meter used only gives readings to 3 significant figures, which reduces the resolution above 100 W. It should be clear that the power stability is better than 1% after 45 minutes. The laser head has an internal shutter, which was hoped would not affecting the power stability, making the initial stabilisation much safer. However, as can be seen in Fig. 7.1 the use of the shutter does cause drifts in the power once the shutter is opened. The shutter was rarely used in the experiment operation, except for non critical alignment.
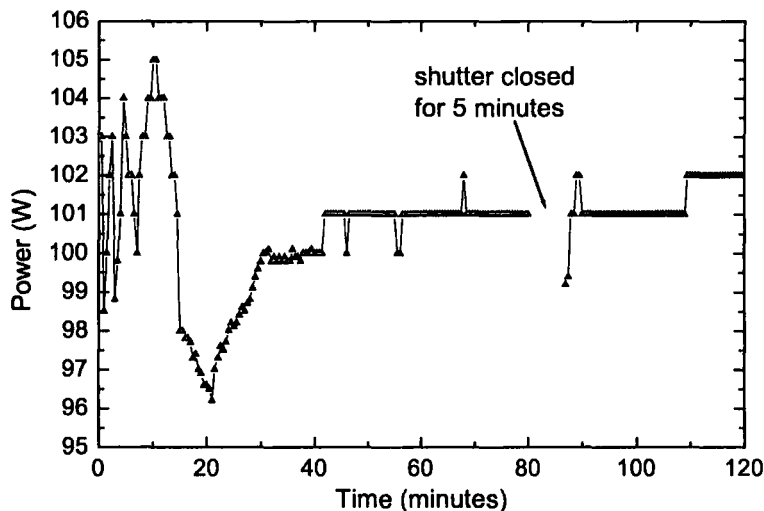
Figure 7.1: Measurements of the CO_2 laser power over 2 hours. The measurements were taken immediately after the laser head with no optics before the power metre. Note that power metre only gives reading to 3 significant figures, reducing the resolution above 100 W.

7.3 AOMs for CO_2 Lasers

For the CO_2 laser we use an AOM to control the intensity of the beam to the experiment. The AOM diffracts the beam into four orders, including the zeroth order, and is arranged so that the first order contains the maximum amount possible. By varying the rf power to the AOM the amount of CO_2 power that is transmitted can be carefully controlled.

An AOM for a CO_2 laser works on the same principles as one for a diode laser, but is much bigger and requires significantly more power. An IntraAction Corp AGM-406BIM AOM is used to control the power that reaches the trapping region. The AOM uses germanium for the mixing crystal and is driven by 30 W of rf power at 40 MHz. This rf is supplied by a GE–4030 driver, also from IntraAction. The AOM crystal absorbs $\sim 10\%$ of the total incident power. This means that 40 W of power must be dissipated from the AOM, otherwise the device will be permanently damaged. The cooling water for the AOM comes for the same chiller as is used for the laser. As an extra level of safety there is a thermal sensor in the AOM which turns off the AOM driver when the temperature of the crystal goes above 40°C. A flow switch was installed on the cooling water line immediately after the AOM. If the water supply fails this cuts the power to the CO_2 laser directly.

The first order diffracted beam from the AOM, with up to 65 W of power is used for dipole trapping experiments. The zeroth order beam, which contains 90 W of power when the power is lowered in the first order, is diverted into an air–cooled beam dump. In addition to these two orders a few W of power is found in the second and the other first order beams. This power is blocked using two further beam dumps. By further knife edge measurements it was found that the first order beam focusses to ~ 2 mm after the AOM. This is due to thermal lensing in the crystal due to the rf power and energy deposited by the laser itself within the crystal. The measurement of the beam profile was very difficult to take as knife edge measurements must be taken close to the AOM. In this region there are 4 CO_2 beams, with significant power in the zeroth and first orders and greater than 1 W in the second and minus first orders. This focussing effect could have been compensated by adjusting the telescope before the AOM. However we used the divergence of the beam in the far field to our

advantage, as described in the next section.

We have found that changing the rf power causes the direction of the first-order beam to change. This has been speculated as being due to a temperature dependent refractive index of the germanium crystal. Angular changes of up to 3 mrad have been measured when the rf power is increased from 3 W to 30 W. For this reason alignment of the CO_2 laser has had to be done with the laser on full power.

7.4 Aligning the CO_2 Laser

The Gaussian beam that emerges from the CO_2 laser has a $1/e^2$ radius of 3 mm. The beam is passed through a $\sim 3 : 2$ telescope (using 1 inch diameter lenses of $f = 190$ mm and $f = 127$ mm) to reduce the insertion loss through the AOM, which has an aperture of 6 mm. Before the AOM was installed in the beam path knife edge measurements were taken after the telescope to ensure a collimated beam.

To achieve deep traps it is then desirable to focus the laser as tightly as possible. The radius of a Gaussian beam focussed by a thin lens is a function of the wavelength of light, λ, the focal length, f and the beam radius before the lens, w [112],

$$w_0 = \frac{f\lambda}{\pi w}. \tag{7.4}$$

Then, for a fixed focal length the spot size at the focus can be minimised by maximising the beam size before the lens. After the AOM the CO_2 beam propagates along a beam path of 3 m, over which distance it diverges to a size of 9 mm ($1/e^2$ radius). As discussed earlier, the trap depth at the CO_2 laser focus depends on the laser intensity. In initial experiments a telescope was included to collimate the laser beam before the final focussing lens, giving a beam waist at the final focussing lens of 7.2 mm ($1/e^2$ radius). This allowed easier calculation of the axial positioning of the focussing lens due to having a collimated beam entering the final lens. However the beam size at the focussing lens is larger if the collimating telescope is removed. The positioning of the lens was not found to be more difficult with a diverging beam before the lens as the divergence was well characterised by knife–edge measurements along the beam. The laser was
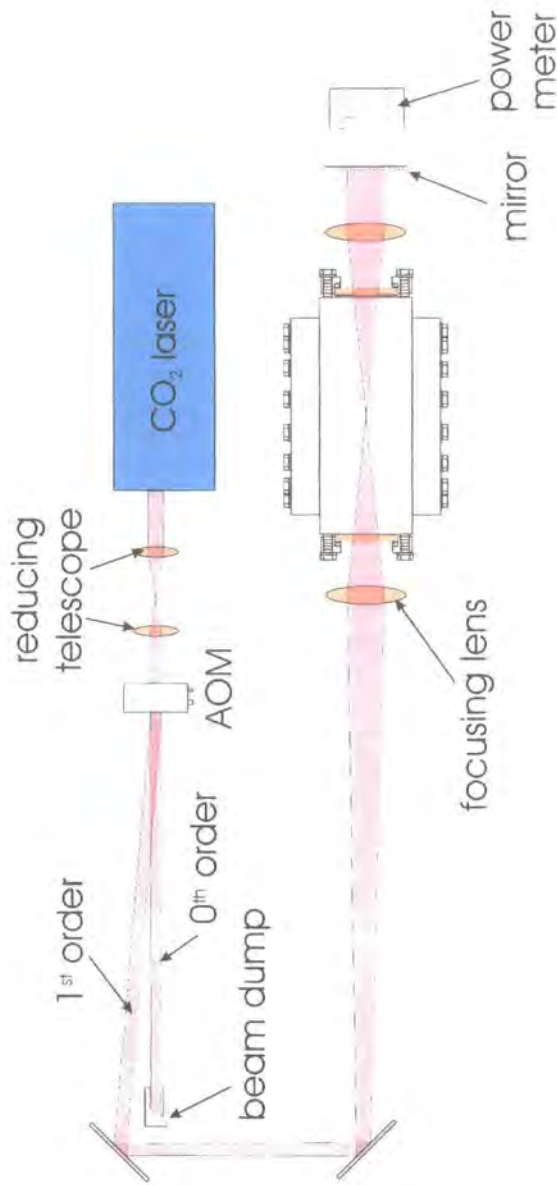
Figure 7.2: CO_2 laser beam path to the experiment. After the chamber the mirror is present for optical lattice experiments and removed for single beam experiments.

focussed into the chamber by a $f = 190.5$ mm lens, producing a final spot size ($1/e^2$ radius) of 71 μm.

When retro–reflecting the beam to form an optical lattice the beam must be slightly misaligned. This precaution is to prevent the beam feeding back into the laser cavity. Also, if the beam were perfectly retro–reflected then the beam

would heat the AOM crystal causing thermal lensing of the beam. This would change the beam alignment completely. The retro–reflected beam is aligned onto a beam dump. The misalignment is approximately 3 mm after a distance of 3 m. At the trap centre this corresponds the separation of the foci of two beams was observed to be < 10 μm.

7.4.1 Overlapping Dipole Trap and MOT

In order to trap atoms in a CO$_2$ laser beam it must be well overlapped with the MOT. This task is very difficult due to the CO$_2$ beam being invisible and having little effect on a MOT operating under normal conditions. A much more 'real world' consideration is that the beam is very powerful and great care must be taken with all adjustments in order to know exactly where all the power is going. This makes alignment a slow and nerve–wrecking procedure. Ideally the beam would be aligned at low power and then the AOM would be ramped up to full power. However the beam position changes when the AOM power is altered. This is due to heating effects from the rf–power and also from thermal–lensing due to the first order beam itself. The movement in beam position at the chamber between 5 W and 55 W of laser power could be greater than 1 cm. While gross alignment could be done at lower powers the final alignment had to be done at full power.

'Burn paper' was used to locate beam edges and on lower beam powers to find the beam centre. Burn paper is a type of paper that blackens very quickly when heated, and is used in thermal printers, such as used in cashier tills in supermarkets. For powers above 10 W the paper will burn with flames if left in the beam for any length of time.

The final focussing lens was mounted on a system of 3 translation stages with Vernier scales giving control of the focus in axial and orthogonal radial directions. Two mirrors before this lens allowed steering of the beam up to this point.

For initial alignment the CO$_2$ laser was operated with a power of $\simeq$ 5 W in the first order, the minimum required to leave a mark on burn paper in a time of 1 s. A beam dump was positioned before the chamber and the CO$_2$ laser was aligned so that it was horizontal and would pass through the chamber, without

the focussing lens installed. This was checked by removing the beam dump and positioning the power metre after the chamber. The power metre was positioned before the chamber in the centre of the laser beam. As the power was ramped up the two steering mirrors were adjusted to keep the laser centred on the power meter. The power meter was then positioned after the chamber and the beam was observed to pass through the chamber and to pass through the centre of each of the ZnSe windows.

Before the lens was installed the path of the CO_2 laser was mapped out by positioning four 5 mm diameter apertures along the beam. Each was positioned to maximise the power passed through. A probe beam with 2 mW at 780 nm was taken from the laser cooling set–up and was overlapped with the apertures. With the MOT running the final steering mirror was adjusted slightly so as to overlap the probe beam with the MOT. The effect of this was a clear perturbation of the position of the MOT. If necessary the apertures were repositioned, but in general this was not required. The ZnSe focussing lens was then positioned so as to focus the probe onto the MOT. Another ZnSe lens was positioned after the chamber, centred on the probe beam and approximately equidistant from the centre of the chamber as the focusing lens. This lens was to re–collimate the CO_2 laser after it passed through the chamber. The axial position of the lens was adjusted for the different refractive index of the ZnSe, (the lens and window,) seen by $\lambda = 10.6$ μm and $\lambda = 780$ nm beams. The probe beam was then removed and, with a beam dump before the chamber, it was checked that the CO_2 laser was overlapped with the apertures. The beam dump was then removed and the power was checked after the chamber to ensure the beam passed straight through.

This procedure, however, did not overlap the CO_2 focus and the MOT due to the refractive index of ZnSe being different for $\lambda = 10.6$ μm and $\lambda = 780$ nm and to the somewhat crude nature of overlapping the CO_2 laser and the resonant probe beam. The final alignment was carried out as described next.

7.4.2 Precise Alignment

Here we examine some of the alignment methods that were attempted.

The group of Summy at Oklahoma State University have approached the prob-

lem of aligning MOT and dipole trap from the consideration that a CO_2 laser *is* a trap [113]. They run their MOT on a far detuning on the order of $5\,\Gamma$ so that their MOT does not load efficiently and is more diffuse than normal. The loading effects of the CO_2 laser can then be seen by observing a region of enhanced fluorescence in the MOT corresponding to atoms trapped from the MOT into the dipole trap. However, we attempted this procedure but with no success.

At Duke University ^{6}Li is trapped in a CO_2 laser dipole trap and have examined the alignment issue from basic optical considerations. In the ideal final configuration, the lens that focusses the dipole trapping laser would be positioned $1/f$ away from the centre of the MOT. However, by considering the MOT to be a point source of a fluorescence, it can be seen that this lens would then also then collimate the emitted light from the trapped atoms. By positioning the final focussing lens to optimise this effect, and allowing for the differing refractive indices of the ZnSe in the focussing lens and the UHV viewports at 671 nm (the wavelength used for laser cooling Li) and 10.6 μm, the lens can be placed so as to be aligned for focussing a collimated beam at 10.6 μm onto the MOT. Even allowing for experimental errors they find that by this method they can generally obtain a signal of trapped atoms that can be further optimised by positioning of the focussing lens. The reason this method was used in their lab is due to the polarizabilities of the ground and excited states being almost identical.

We tried to use this procedure in our experiment but got signal. For a MOT containing 10^7 atoms the peak intensity levels expected are on the order of 1×10^{-9} W cm^{-2}, which is 3 orders of magnitude less than that detected on the photodiode for number measurements. The photodiode used for temperature measurements would then have given a signal of ~ 1 mV for a MOT of this size. Beam profiles of this collimated 'beam' would then have to be taken to check the beam was collimated. This method was attempted using a CCD camera, but no signal was ever found.

7.4.3   Anti-Trapping as Optimised Alignment

In Rb the ground and excited states for laser cooling have significantly different polarizabilities at $\lambda = 10.6$ μm and correspondingly different light–shifts. Both states are shifted down in energy at this wavelength but the light–shift of the excited state is $\simeq 2.5$ times that of the ground state. For an optical lattice, with single beam power of 45 W focused to a e^{-2} radius of 70 μm the mean differential light shift between the excited and ground states at the centre of the lattice is 57 MHz. If the MOT is run at a detuning of less than this then the atoms in the region of the CO_2 laser will see the MOT lasers to be blue detuned with respect to the cooling transition and will be heated in, and ejected from, the overlap region. This effect, the absence of atoms in a background of cold atoms should be clearly seen if the density of the atoms is low. This low density can be achieved by keeping the Rb vapour pressure low and by lowering the B-field gradient in the MOT.

B-field gradients as low as 1 $G\,cm^{-1}$ were used in this anti-trapping alignment technique. The detuning of the cooling light was set to $\Delta = -4$ MHz. Two, orthogonal CCD cameras were focussed on to the MOT and both were monitored in real time. The focussing lens was rastered across a small volume. When the CO_2 and the cold atom cloud were overlapped a dark stripe was seen on the monitor screen, as the example in Fig. 7.3 shows. In the first observation the movement of the stripe is usually more easily observed than the stripe itself. The dark region was then centred on the MOT centre.

Figure 7.3: Screen captures of images taken during alignment of the CO_2 laser with the MOT using the anti–trapping technique. The CO_2 laser can be seen as a dark stripe through the centre of the image.

The MOT was then switched back to normal operation. For the final alignment, the number of atoms captured in the dipole trap from an optical molasses were measured by a fluorescence imaging on to a CCD. The position of the CO_2 laser was optimised by adjusting the focussing lens to optimise the number of atoms captured.

7.5 Dirty Windows

It was noticed that a speckled, scummy layer appeared on the inside of the ZnSe viewports after a few months of operation of the MOT. Concerned that it was some chemical from the dispensers, as these are the only active element within the vacuum chamber, we contacted SAES. They assured us that there could be no reactive compounds, other than those meant to be in the dispensers. The suspicion was then that it was a reaction between Rb and the anti–reflection coating on the windows used. We were worried that this scum might affect the transmission of the CO_2 beam. A fraction of the CO_2 beam power was diverted to pass through the chamber without focussing to observe the effect on the transmitted power. For an input power of 30 W approximately 6 % of the power was absorbed by two windows. The pressure in the chamber, as measured by the ion–gauge, was observed to increase from 2.2×10^{-10} Torr to $\sim 10^{-9}$ immediately but returned to the original pressure within 10 s. This pressure change was not observed again when shining the CO_2 laser through. Later conversations with members of the Weitz group indicated that they observed this layer on their focussing lens, which were within their chamber. Over time up to 25 % of the CO_2 power was lost on these optics, meaning they had to be changed with each vacuum break. In our set–up, the power lost never went above ~ 3 % on each of the windows.

Chapter 8

CO_2 Laser Trapping of Rb

This section describes how Rb atoms are loaded into the CO_2 laser dipole trap and the imaging technique used to extract the number and spatial distributions of the trapped atoms.

Both the ground and excited states of the Rb cooling transitions have positive scalar polarizabilities at the CO_2 wavelength, $\lambda = 10.6$ μm. The excited state scalar polarizability is, however, 2.5 times that of the ground state. For even moderate trapping intensities the operation of the MOT is affected by dipole trapping field.

Switching of the power in the CO_2 laser with the AOM causes changes in the position of the beam. For this reason the CO_2 laser is left on at full trapping power at all times except for during the imaging of the trapped atoms which takes a few ms.

For loading, the thermal Rb vapour was provided by pulsing a focussed Nd:YAG laser onto the dispensers, as described in Section 4.3. The MOT was loaded with 2×10^7 ^{85}Rb atoms in approximately 3 s, followed by a 10 ms optical molasses phase to reduce the atomic cloud temperature to 20 μK, measured in a separate experiment with the CO_2 laser switched off. For the molasses phase the repumper power was reduced to 200 μW/cm^2 and was completely switched off with a shutter for the final 5 ms such that the atoms were pumped into the lower hyperfine state [78]. The MOT beams were then switched off with an AOM and the cold atom cloud allowed to fall, under gravity, out of the trapping region. To measure the number of atoms, and the spatial distribution of the

trapped atoms the CO$_2$ laser was switched off and the MOT beams, tuned to resonance, were pulsed on. The scattered fluorescence was captured with the CCD camera.

8.1   Dipole Trap Heating and Trapping Lifetimes

8.1.1   Considerations

There are three mechanisms for heating atoms that are confined in an optical dipole trap: fluctuations of the trapping laser, scattering of the trapping light and collisions with hot background atoms.

Trapping Laser Fluctuations

As reported by the Thomas group, the causes of parametric heating in an optical dipole trap are intensity noise and position (pointing) noise [108, 109]. In the first case, fluctuations at twice the trap frequency cause resonant driving of the atomic motion. In the second case, shaking at the trap frequency directly couples to the atomic motion, increasing the amplitude of oscillations.

These fluctuations are difficult to measure directly. Studies of these noise sources in a Coherent–DEOS laser, similar to that used in our experiments, have been taken [114]. Observed heating rates are on the order of hours. O'Hara *et al.* have demonstrated trap lifetimes for Li of 300 s in a CO$_2$ laser trap, which is predicted to be limited only by the background pressure.

The optical set–up for the CO$_2$ laser in the experiments described here was made as mechanically stable as possible. Large, heavy mounts and posts were used where possible for lenses and mirrors. The trap lifetimes measured in the experimental chamber of 6 s appear to be limited by a background pressure on the order of 2×10^{-10} Torr.

Scattering of Trap Light

Red–detuned optical dipole traps do have the feature of trapping atoms at the maximum of laser intensity, thus it is important that the scattering rate is very low. The scattering rate of a far detuned laser is [18]

$$\Gamma_{sc} = \frac{3\pi c^2}{2\hbar\omega_0^3} \left(\frac{\omega}{\omega_0}\right)^3 \left(\frac{\Gamma}{\omega_0-\omega} + \frac{\Gamma}{\omega_0-\omega}\right)^2 I \,. \tag{8.1}$$

To a good approximation we can write $\Gamma_{sc} \propto I/\Delta^2$, from which it is clear that the photon scattering rate decreases rapidly with increasing detuning. Using our trapping parameters in Eqn. 8.1 we get $\Gamma_{sc} = 7.0 \times 10^{-3}$ Hz, or approximately 2.5 photons per hour.

The scattering of $\lambda = 10.6$ μm photons by Rb will, due to conservation of energy, be completely elastic. The energy gained by an atom during scattering, $E_{recoil} = (\hbar^2 k^2)/(2M)$ will be a factor of $(\lambda_{CO_2}/\lambda_0)^2 \approx 185$ lower than for scattering of resonant light. Combined with the low scattering rate, we calculate a heating rate,

$$\dot{E}_{heat} = \Gamma_{sc} \times 2\,E_{recoil}$$
$$= \Gamma_{sc}\,\frac{\hbar^2 k^2}{M} \,, \tag{8.2}$$

or 4.5 pK/s.

Collisions with Background Atoms

Background gas atoms in the vacuum system will typically have a temperature of 300 K. As the trap depth U_0/k_B is of the order of 1 mK collisions with such a 'hot' atom will generally cause single particle loss and both partners in this collision will exit without colliding with other atoms . These losses are a function of the flux of background atoms and so vary linearly with the background pressure. Glancing collisions can transfer energy to atoms, but unless the energy gained $\Delta E < U_0$ the atom will be expelled from the trap. However, Cornell *et al.* predict that such collision are negligible for traps on the order of a few mK [54].

8.2 CO_2 Trap Loading

The first experiments on dipole trapping were attempted with a single focussed CO_2 laser. The laser was focussed to a beam waist of 89 μm and with a power of 50 W in the beam. This corresponds to a trap depth of 300 μK.

Atoms were loaded directly from an optical molasses with a measured, free space temperature of 22 μK. Up to 2×10^6 ^{85}Rb atoms were loaded into this single–beam trap.

8.3 Dipole Trap Measurements

All measurements of the dipole trap were taken from CCD images. This method allowed both number and spatial information to be extracted simultaneously. Dipole trap images were taken typically more than 50 ms after the MOT had been turned off. For shorter delay times the atoms not in the dipole trap had not fallen out of the trapping region.

During imaging the dipole trapping beam was switched off. Imaging then takes place in the absence of any spatial differential light–shifts which allows measurement of the true spatial distribution. The scheme for imaging was as follows: the trap was switched off with the AOM in < 1 μs and the on–resonance trapping and repumping beams were pulsed on for 100 μs. The fluorescence was captured with the CCD camera. Using the pixel count calibration described in the MOT imaging section the total trapped atom number was estimated.

8.3.1 Dipole Trap Lifetime

The lifetime of the dipole trap was measured by monitoring the trapped atom number for varying hold time in the CO_2 laser trap. Initial measurements of the trap lifetime, shown in Fig. 8.1, indicated a $1/e$ trap lifetime of 6.25(1.42) s. The pressure in the vacuum chamber was measured to be 1.4×10^{-10} Torr. Emperical evidence from other groups suggest that for a background pressure of 10^{-9} Torr a trap lifetime of 1 s is typical [54]. An order of magnitude reduction in the back ground pressure produces and order of magnitude longer
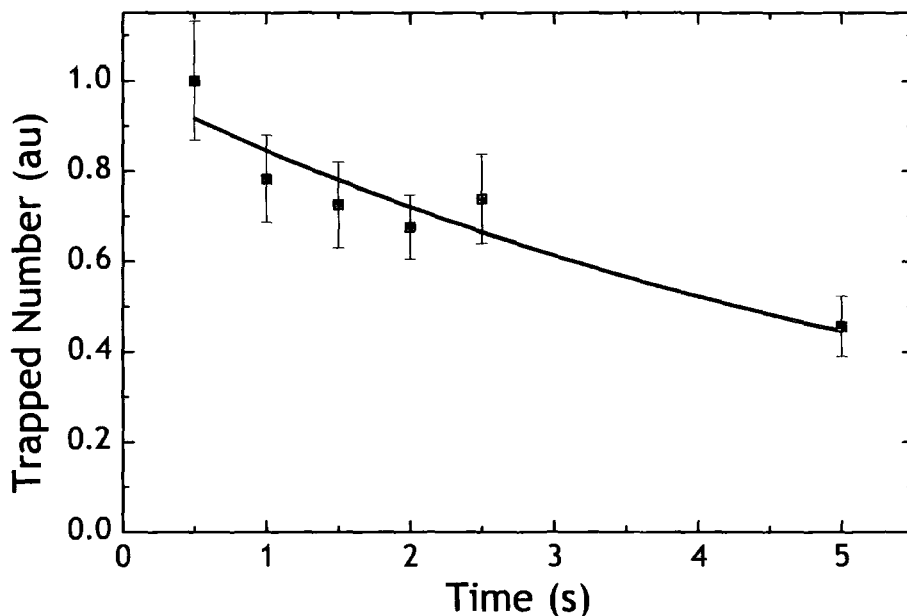
Figure 8.1: Measurement of the dipole trap lifetime up to 5 s. The exponential fit gives a time constant of 6.25(1.42) s.

trap lifetimes. Our lifetime result and pressure measurement indicate that the lifetime is background pressure limited. This initial experiment was as a proof of principle that we could trap atoms for long time periods. The longest hold time used for measurements was 5 s.

Further measurements were taken of the dynamics of the initial atom decay in the trap. Fig. 8.2 shows an initial fast decay of the atom number then a slower decay. A double exponential fit to the trapped atom number gives time constants for the fast and slow decay of 152($\pm$128) ms and 2.67($\pm$2.93) s, respectively. This initial decay is attributed to plain evaporation of the hotter atoms from the trap. The shorter time constant here for the slow decay is due to a higher background pressure as the trap was loaded with approximately an order of magnitude more atoms than for Fig. 8.1.

Lifetime measurements were also taken for an optical lattice. The trap depth in this case is $U_0/h = 1.9$ mK. The time constants measured for the lattice were 39($\pm$13) ms and 1.77($\pm$0.10) s for the fast and slow decays, respectively.
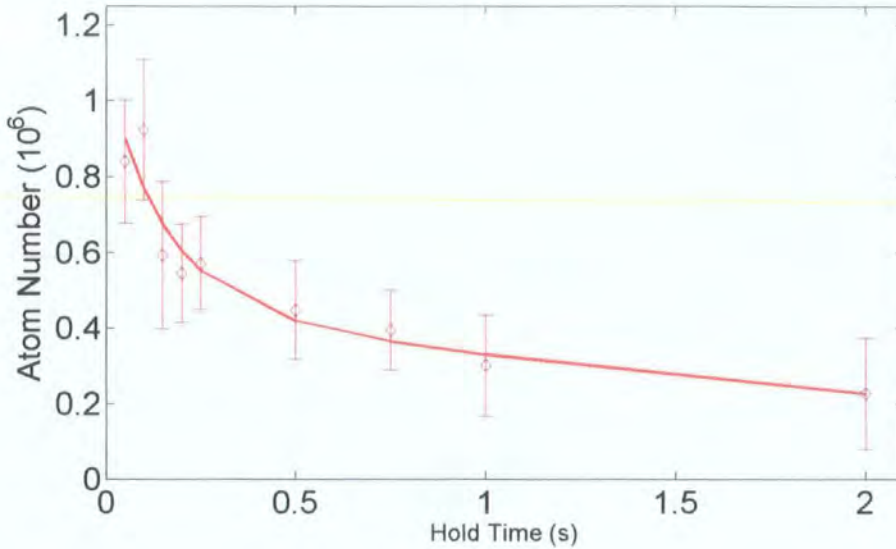
Figure 8.2: Double exponential fit to dipole trap lifetime. An initial decay rate of 150($\pm$128) ms is followed by a slower rate of 2.67($\pm$2.93) s.

The data for this measurement are plotted in Fig. 8.3. The lifetimes of the single–beam and lattice traps, after the fast initial decay, are consistent and are suspected to be pressure limited.

8.4 Molasses Cooling in the Optical Dipole Trap

Our loading procedure involved using a molasses phase detuned by ~ -8 Γ from the $F = 3 \rightarrow F' = 4$ resonance. In this way we achieved trapped atom temperatures of 77 μK in an optical lattice, as measured by time–of–flight. Other groups have used molasses phases of -18 Γ, for ^{85}Rb, [115] and -23.5 Γ, for ^{87}Rb, [49] and have observed trapped temperatures of 9 μK in a CO$_2$ lattice and 38 μK in a CO$_2$ crossed trap, respectively, after a 1.5 s hold time. Both temperatures were significantly lower than $U_0/10$, the typical temperature of
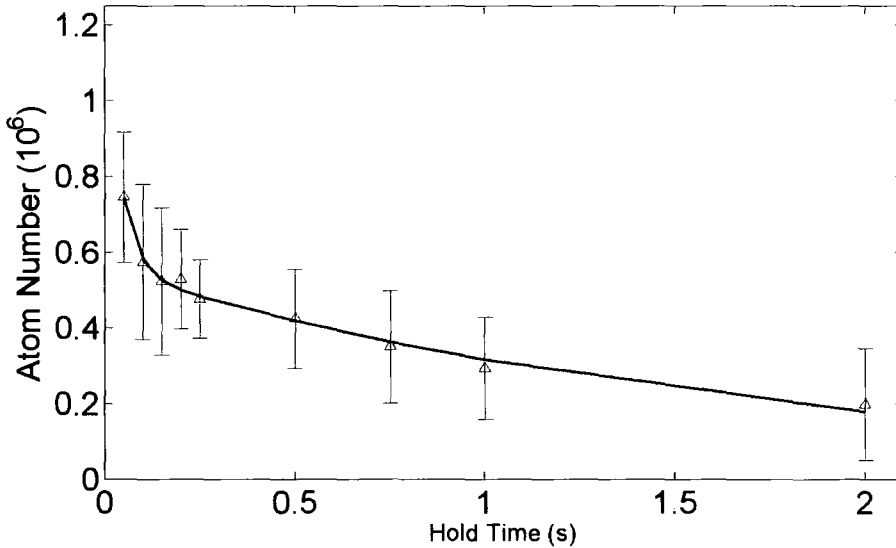
Figure 8.3: Double exponential fit to optical lattice trap lifetime. An initial decay rate of $39(\pm13)$ ms is followed by a slower rate of $1.77(\pm0.10)$ s.

trapped atoms after free evaporation, where U_0 is the trap depth. These low temperatures are suggested as being due to a blue detuned molasses [116]. The laser frequency is now closest to the $F \rightarrow F' = F$ transition. In regions of circularly polarised cooling light atoms are locally pumped into the $m_F = \pm F$ Zeeman level of the ground state, which is then dark to the light that pumped it there, resulting in reduced scattering. In linearly polarised regions atoms are cooled by blue detuned Sisyphus cooling.

8.4.1   Molasses Duration

The effect of the molasses duration on the number and distribution of atoms loaded was investigated. The results are shown in Fig. 8.4. The free-space temperature of the MOT was measured to be $200(17)$ μK, which is $\sim U_0/10$ for Rb in an optical lattice using 45 W of CO_2 power focussed to 71 μm. However it was observed that atoms did not load into the optical lattice without a molasses

phase. A maximum number of atoms were observed to be loaded into the lattice for a molasses phase lasting approximately 5 ms. For longer molasses phases the differential light–shift effects were observed to become pronounced. The reason behind this is not understood. It is evident that further cooling occurs due to the molasses as atoms are now loaded into the optical lattice. If the reduced loading at the lattice centre was due only to the differential light–shift then it would be expected that this effect would be observed for all molasses durations. The loss of atoms could be postulated as being due to light–induced collisions which are enhanced by the differential light–shift.

8.5 Evaporative Cooling

Evaporative cooling entails selectively removing atoms from the high–energy tail of the thermal distribution and then allowing the remaining atoms to come into thermal equilibrium. In order to successfully complete the second part, the atomic density must be high enough so that thermalising, elastic scattering rate is large in comparison with the trap lifetime.

Evaporative cooling in an optical dipole trap was first observed in 1995 [78] when Adams *et al.* trapped Na in a crossed Nd:YAG optical dipole trap, observing high initial densities of 4×10^{12} atoms/cm^2. Subsequent forced evaporation reduced the temperature of trapped sodium atoms to 4 μK and increased the phase space density by a factor of 28. The next reported result of evaporative cooling in an optical dipole trap was not until 2000 when Engler *et al.* realised cooling of rubidium in a CO_2 laser trap with very long storage times of > 150 s [117]. Free evaporation from the trap reduced the temperature by a factor of 2 over 300 s. This result was only attainable due to the exceptionally low heating rates due to a stable trapping laser and low background pressures.

Efficient evaporative cooling in an optical dipole is complicated by the fact that lowering the trap depth causes relaxation of the trapping parameters, slowing down the rethermalisation stage. However the very high phase space densities that have been observed in optical dipole traps, and the high trapping frequencies that can be found in crossed and lattice geometries mean that the initial collisional rates are also very high and evaporation proceeds rapidly. An

all–optic BEC of ^{87}Rb was created in a crossed CO$_2$ laser, dipole trap by evap-
oratively cooling a trapped atomic sample to degeneracy in ~ 2 s [49]. Since
then the same group has improved the efficiency of this technique to achieve
condensates of 3×10^5 atoms in similar timescales [118]. Kinoshita *et al.* have
created similar sized BECs from forced evaporation in a Nd:YAG laser trap
[119]. Both these last two techniques involve dynamically changing the spot
size at the laser focus after loading of the dipole trap to increase the density
and collision rates. By this method the trap frequencies can be kept constant
or even increased during evaporation. Optical dipole traps have since become
the tool of choice for creation of Fermi–degenerate gasses as the trapping is
state–independent [50].

In the experiments in this thesis no attempt was made to force evaporation
of atoms from the dipole trap. Generally, experiments were conducted with
trapped atom temperatures much lower than $U_0/10$, the typical temperature
limit of free evaporation.

8.6   Atomic Oscillation Frequencies in an Optical Dipole Trap

The oscillation frequencies can be found by a Taylor expansion of the trap-
ping potential in the radial and axial directions. From Hooke's law, the spring
constant is related to the potential by

$$U = -\frac{1}{2} k\, x^2 \; . \tag{8.3}$$

Then using the relation between oscillation frequency and the spring constant

$$\omega = \sqrt{\frac{k}{m}} \; , \tag{8.4}$$

where m is the atomic mass, we arrive at the oscillation frequency.

Radially, the potential varies as

$$U(r) = U_0\, e^{-2\frac{r^2}{w_0^2}}$$
$$= U_0 \left(1 - \frac{2r^2}{w_0^2} + O[r^4] \right) \; . \tag{8.5}$$

Using Eqns. 8.3,8.4 we get

$$\omega_r = \sqrt{\frac{4\,U_0}{m\,w_0^2}} \; .$$

(8.6)

Axially, at the beam focus

$$U(z) = U_0 \cos^2\left(\frac{2\,\pi\,z}{\lambda}\right)$$

$$= U_0\left(1 - \frac{4\,\pi^2\,z^2}{\lambda^2} + O[z^4]\right) \; ,$$

(8.7)

and in the same way as above

$$\omega_z = 2\pi\,\sqrt{\frac{2\,U_0}{m\,\lambda^2}} \; .$$

(8.8)

In a single running beam trap

$$U(z) = U_0\,\frac{w_0^2}{w(z)^2}$$

$$= U_0\left(1 - \frac{\lambda^2\,z^2}{\pi^2\,w_0^4} + O[z^4]\right)$$

$$= U_0\left(1 - \frac{z^2}{z_R^2} + O[z^4]\right)$$

(8.9)

$$\Rightarrow \omega_z = \sqrt{\frac{2\,U_0}{m\,z_R^2}}$$

(8.10)

In our experiments $U_0 = 1.9$ mK, $w_0 = 71$ μm and $z_R = 1.5$ mm. This gives trapping frequencies of $\omega_r = (2\pi)\,1.93$ kHz and $\omega_z = (2\pi)\,57.3$ kHz. These results compare well with measured results for similar trapping parameters in the Weitz group [28].

8.7   Atomic Density

The spatial extent of the trapped atom cloud can be estimated from knowledge of the oscillation frequencies of the trap. In a harmonic trap the mean potential energy per dimension will be

$$\frac{1}{2}\,k_B\,T = \frac{1}{2}\,M\,\omega_i^2\,\langle x_i^2\rangle \; .$$

(8.11)

From our calculated oscillation frequencies of $\omega_r = (2\pi)\,1.93$ kHz and $\omega_z = (2\pi)\,57.3$ kHz we obtain widths of $r_{\mathrm{rms}} = 7.3$ μm and $z_{\mathrm{rms}} = 0.24$ μm.(The

peak number of atoms per site was measured to be ~ 3500 giving an estimated peak density of 4.2×10^{12} atoms/cm^3. For a measured temperature of 80 μK, with an associated de Broglie wavelength of $\lambda_{dB} = 37$ nm, this gives a phase space density of $\sim 2 \times 10^{-4}$.

8.8   Temperature Measurements

The temperature of the trapped atoms was measure by time of flight expansion. The MOT was loaded for ~ 3 s, followed by a (typically) 10 ms molasses phase. The CO_2 laser trap was overlapped with the atomic cloud centre during the optical cooling phases. During the molasses phase the repump intensity was reduced by a factor of 30 and completely shut off for the final 5 ms of the molasses phase. The cooling light was then extinguished and the untrapped atoms allowed to fall under gravity out of the experiment region. The CO_2 power was switched off in ~ 1 ms and after a variable time–of–flight the MOT beams, tuned to resonance, were pulsed back on for an imaging time of 100 μs. The scattered light was collected on a CCD camera to give spatial and number information of the trapped cloud.

In a single beam trap, $U_0 = 470$ μK, a temperature of 51($\pm$3) μK was measured. We have measured a temperature of 77($\pm$4) μK in our optical lattice, for a trap depth of $U_0 = 1.9$ mK. At first examination this appears rather high in comparison to the results quoted by other groups; Friebel *et al.* measured temperatures of 15 μK for ^{85}Rb in a CO_2 laser optical lattice [115]. However this lattice had a depth of only 360 μK. The same group measured temperatures of 70 μK for a lattice of 2.1 mK deep [28], a system which is directly comparable to ours. The molasses phase for this loading was similar to earlier experiments, using a detuning of -13 $\Gamma = -78$ MHz. The maximum differential light–shift in this lattice is 65 MHz meaning that in no region would the trapped atoms experience a differential light–shift strong enough to cause effective blue–detuning of the molasses light.

Also, in the first all–optical BEC, the temperature of ^{87}Rb atoms trapped in a crossed dipole trap was initially measured to be 75 μK [49]. This trap had a rel-atively lower depth of 780 μK, though due to the crossed geometry orientation

it had oscillation frequencies of ~ 1.5 kHz in all directions. Through free evaporation the measured temperatures reduced to 38 μK, which is approximately $1/10^{th}$ the depth of the individually trapping beams.
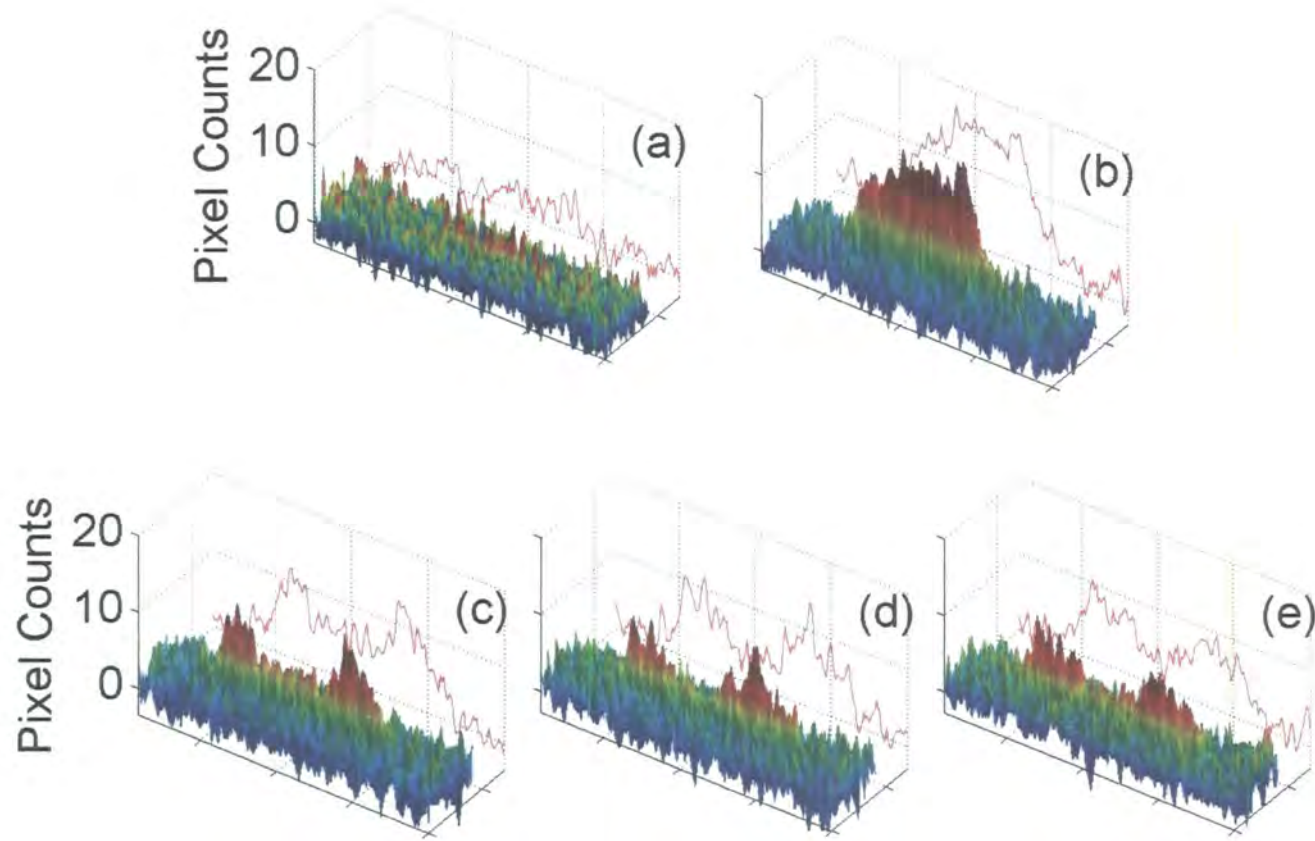
Figure 8.4: The effect of molasses duration on number and distribution of atoms loaded into the optical lattice. The scale of the spatial axes is 2 mm×0.5 mm. The molasses times are a) 0 ms, b) 5 ms, c) 10 ms, d) 15 ms, and e) 20 ms. The images were taken after a 60 ms hold time in the lattice trap. The molasses parameters are $\Delta = -30$ MHz and single beam intensities of 4 mW/cm². The molasses temperatures are shown in Fig. 4.13.

Chapter 9

Enhanced Loading of Dipole Traps

9.1 Introduction

Loading of ultra-cold atoms into an optical dipole trap is a complex problem. Loading into two, overlapped traps with very different optical and trapping parameters raises the complexity even further. However, this system, as will be shown, provides some initially counter–intuitive results.

9.2 Two Dipole Fields

9.2.1 Introduction

The effect of including a second dipole trapping field requires some adaption of the theory considered, but does introduce somewhat counter-intuitive effects. The special cases of two laser fields of identical or nearly-identical frequencies, or of counter-propagating laser beams are standard in literature and have been examined in many cases, [28, 78].

In this section we look at the light–shifts of the excited state of alkali atoms in the presence of two lasers, with frequencies differing by an order of magnitude. However, the theory developed is general and applies any laser fields for which

the dynamic polarizabilities are known. In this case we also define that the lasers propagate orthogonally to each other and with the polarizations orthogonally aligned.

9.2.2 Theory

The theory of this section is essentially a slight modification of the situation of an atom in a single dipole field. The scalar and tensorial matrices for each field are calculated and are summed before diagonalisation,

$$U = U_0 - \frac{1}{2\epsilon_0 c} \sum_{i=1,2} \left(\alpha_0^i \mathbb{1} + \alpha_2^i Q \right) I_i \, . \tag{9.1}$$

As discussed earlier, the tensorial matrix for light polarized along the z–axis is block diagonal in the $|F, m_F\rangle$ basis, as shown in Eqn. 6.40 and Fig. 6.6.

For orthogonally polarized light (i.e., along the x– or y–axes), the tensorial matrix is of the form,

$$
\left(
\begin{array}{cccccccccccccccc}
\| & & & \bot & \bot & \bot & & & & & & & & & & \\
& \| & \| & & & & \bot & \bot & \bot & \bot & & & & & & \\
& \| & \| & & & & \bot & \bot & \bot & \bot & & & & & & \\
\bot & & & \| & \| & \| & & & & & \bot & \bot & \bot & & & \\
\bot & & & \| & \| & \| & & & & & \bot & \bot & \bot & & & \\
\bot & & & \| & \| & \| & & & & & \bot & \bot & \bot & & & \\
& \bot & \bot & & & & \| & \| & \| & \| & & & & \bot & \bot & \\
& \bot & \bot & & & & \| & \| & \| & \| & & & & \bot & \bot & \\
& \bot & \bot & & & & \| & \| & \| & \| & & & & \bot & \bot & \\
& \bot & \bot & & & & \| & \| & \| & \| & & & & \bot & \bot & \\
& & & \bot & \bot & \bot & & & & & \| & \| & \| & & & \bot \\
& & & \bot & \bot & \bot & & & & & \| & \| & \| & & & \bot \\
& & & \bot & \bot & \bot & & & & & \| & \| & \| & & & \bot \\
& & & & & & \bot & \bot & \bot & \bot & & & & \| & \| & \\
& & & & & & \bot & \bot & \bot & \bot & & & & \| & \| & \\
& & & & & & & & \bot & \bot & \bot & & & & & \|
\end{array}
\right) . \tag{9.2}
$$

The effect is to couple terms that differ in m_F by $\pm 2, 0$. This form comes about due to the possible combinations of μ in Eqn. 6.39. As should be expected, the

eigenenergies of this matrix are identical to those plotted earlier in Section. 6.6, with levels being split according to $|m_F|$.

9.3 Reducing the Differential Light–Shift

The differential light–shifts, discussed in Section 6.8 come about as the scalar polarizability of the $5^2P_{3/2}$ excited state of Rb is 2.6 times larger than that of the $5^2S_{1/2}$ ground states at $\lambda_{CO2} = 10.6$ μm. A second laser field, at a wavelength where the excited state polarizability is large and negative would counteract the detrimental effects this has on laser cooling and loading of atoms in the trap region. A further consideration must be be that the ground state polarizability at this second wavelength must be either small or positive so as to not reduce the trap depth.

From the calculations shown in Fig. 6.7 we see that the a high powered laser Nd:YAG laser at $\lambda_{Nd:YAG} = 1$ μm fulfils the requirements outlined. As show

λ	α_0 [5s] (a_0^3)	α_0 [5p] (a_0^3)	α_2 [5p] (a_0^3)
1.064 μm	722	-1166	567
10.6 μm	335	873	-155

Table 9.1: Calculated polarizabilities for the $5S_{1/2}$ and $5P_{3/2}$ states of Rb. For a state with $J = 1/2$, $\alpha_2 = 0$.

in Table 9.1, the excited state α_0 at the Nd:YAG wavelength is of the opposite sign and significantly larger than that at the CO_2 wavelength. Furthermore, the ground state polarizability is the same sign and more than twice as big. Then, at the Nd:YAG wavelength we see that the differential light–shift is of the opposite sign, making the cooling light more red–detuned at trap centre.

9.4 Solving the Light–Shift For Two Fields

The solutions for two laser fields have been solved as the differential light–shift between the excited $5^2P_{3/2}$ states and the ground $5^2S_{1/2}$ states of ^{85}Rb for the experimentally realisable conditions in the laboratory. The calculations were
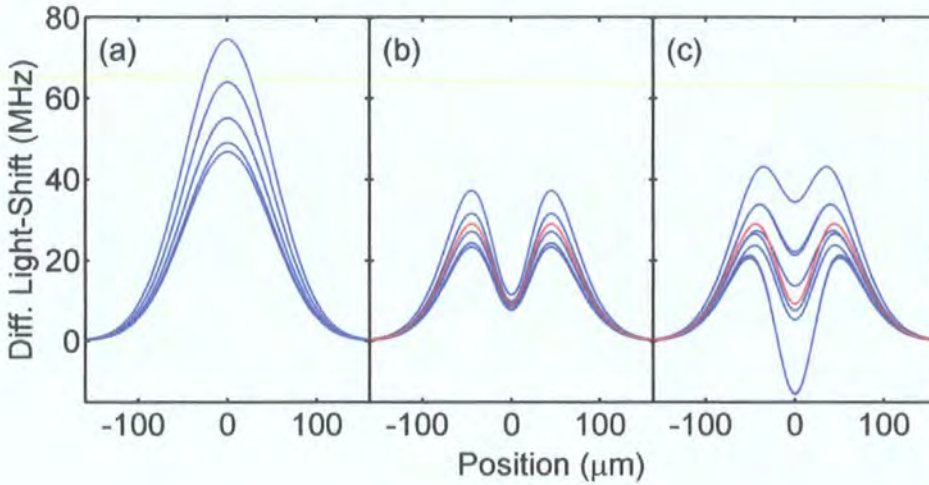
Figure 9.1: Differential light–shifts as a function of position along an axis perpendicular to both the CO_2 and Nd:YAG laser propagation directions. Plotted are, the differential light–shift in (a) the CO_2 laser lattice only, (b) the overlapped CO_2 and Nd:YAG region, with parallel polarizations, and (c) with orthogonal polarizations. The red line in (b) and (c) shows the differential shift due to the scalar polarizabilities alone.

performed for a 45 W, CO_2 laser focussed to 70 μm and retro–reflected to create an optical lattice of trap depth $U_0/h = -36$ MHz. A 7.8 W Nd:YAG beam, focussed to a beam waist of 30 μm crosses the CO_2 beam at 90°. The ground state light–shift of the Nd:YAG beam is $U_0/h = -18.6$ MHz. The results for the calculations are shown in Fig. 9.1 for the cases of parallel, and orthogonally aligned polarisations. The result from Fig. 6.10 is shown for comparison to the situation with the CO_2 laser alone.

In Fig. 9.1(a) and (b) the states are separated, as before, by $|m_F|$. In Fig. 9.1(c) this degeneracy is lifted. More importantly, one of the m_F states is pulled down into a region where it is acquires a large effective red–detuning. In both (b) and (c) the differential light–shift due to the scalar polarizabilities alone is

plotted, and is observed to be effectively blue–detuned at all intensities (in this situation).

Chapter 10

Results of Light–Shift Engineering

Due to the manipulation of the excited state light–shift we find that loading into the light–shift engineered region can be more efficient than in the CO_2 dipole trap alone. Ideally the engineering of the differential light–shift would allow cooling of the atoms in this region to lower temperatures than the CO_2 trap. However other effects are found to lead to higher temperatures in the engineered region.

Light–shift engineering occurs in the region where the trapping and perturbing lasers overlap. The localised nature of the light–shift engineering allows, with tuning of the cooling laser detuning during the molasses phase, region specific loading of the CO_2 lattice.

10.1 Alignment of Trapping and Perturbing Beams

The most technically challenging aspect of the experiment is to overlap the CO_2 and Nd:YAG lasers. The CO_2 dipole trap was aligned with the MOT centre, which was fixed at the zero of the B–field of the MOT coils. The MOT laser beams were aligned through the centre of the BK7 windows. Two of the ZnSe windows were used for the CO_2 dipole trapping beam. The Nd:YAG beam

could then either be aligned through the vertical ZnSe viewports or at an angle through one the large BK7 viewports. The anti–reflection (AR) coated ZnSe windows reflect $\sim$ 30% of light at λ = 1.06 μm (quoted by Umicore Laser Optics). While the reduced intensity at the focus is undesired a greater concern is that reflections from the exit window could cause standing wave effects in the Nd:YAG beam. Also, the ZnSe viewports were 22 cm from the centre of the chamber, limiting the minimum spot size of the focussed beam that could be achieved. By focusing the laser through the large viewports we could use a shorter focal lens, f = 15 cm, achieving a smaller spot size at the focus and avoid the standing wave effects.

The Nd:YAG beam was focussed into the chamber as shown in Fig. 10.1. The angle between the laser beam (the principal ray) and the window was measured to be 19° to the normal. For this angle 80.3(4) % of the power was measured to be transmitted through the 6 mm thick viewports. For normal incidence, the quoted transmission is 92%.

Focussing a laser through an inclined glass plate causes aberration of the beam, see Fig. 10.2. In the plane of the beam shown, the laser focuses to a point different than it would in the absence of the plate. In the other plane which is also orthogonal to the plate surface the beam will again focus to a different point. The predicted separation of each δf is [120]

$$\delta f = d \left(1 - \frac{\cos \alpha}{\sqrt{\eta^2 - \sin^2 \alpha}} \right) , \tag{10.1}$$

where d is the thickness of the plate, η is the refractive index of the plate and α is approximately the angle between the principal ray and the normal to the window. For a laser beam focussing at $\alpha_\perp$ = 19° through a plate with d = 6 mm and of refractive index η = 1.49 the predicted separation of the two foci is 0.12 mm.

The above calculation does not account for Gaussian beams nor for differences in the beam radii prior to focussing and makes small angle approximations. To examine the effect on our real system the laser beam was diverted with a mirror before the focussing lens. The beam was focussed through a unused viewport at the appropriate angle and knife–edge measurements were taken about the focus (see Appendix A for details of knife–edge measurements). Fig. 10.3 shows that
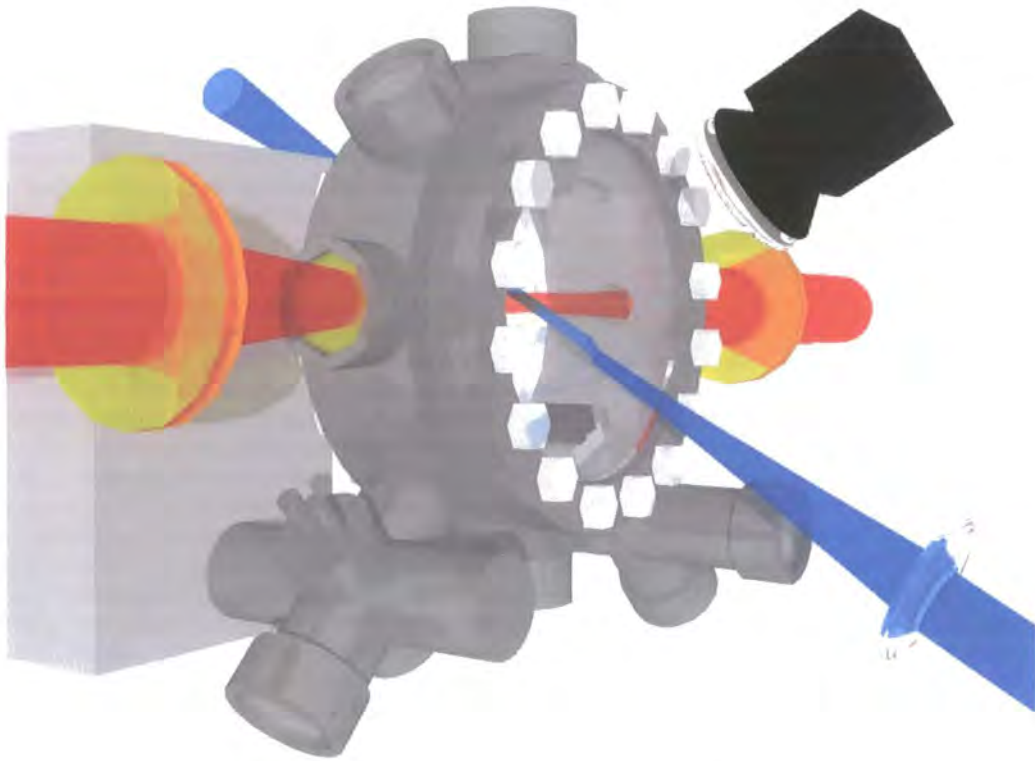
Figure 10.1: Schematic of the overlapped CO_2 and Nd:YAG lasers. The CO_2 laser enters horizontally while the Nd:YAG laser enters at 19° to the horizontal. The imaging camera (top right) is orientated such that the field of view is approximately perpendicular to both CO_2 and Nd:YAG beams. The MOT beams are removed for clarity but two pairs of retro–reflected beams are in the vertical plane at ±45° to the CO_2. The other enters horizontally through the centre of the large viewports.

the vertical and horizontal waist minima are separated by 8(±1%) mm, vastly different from that predicted by raytracing. The main reasons for this are due to the beam not being perfectly Gaussian and also having different radii in the horizontal and vertical directions, as can be seen from the fits in Fig. 10.3.

The minimum spot size can be estimated by the product of the fits, Fig. 10.4, which gives an area of 2430(80) μm^2. At this point we expect the maximum trap depth for the Nd:YAG laser. Initial alignment of the Nd:YAG as a dipole trap agree with the form of the potential shown in Fig. 10.4, with a sudden minimum of the trap followed by a region of lesser trap depth.
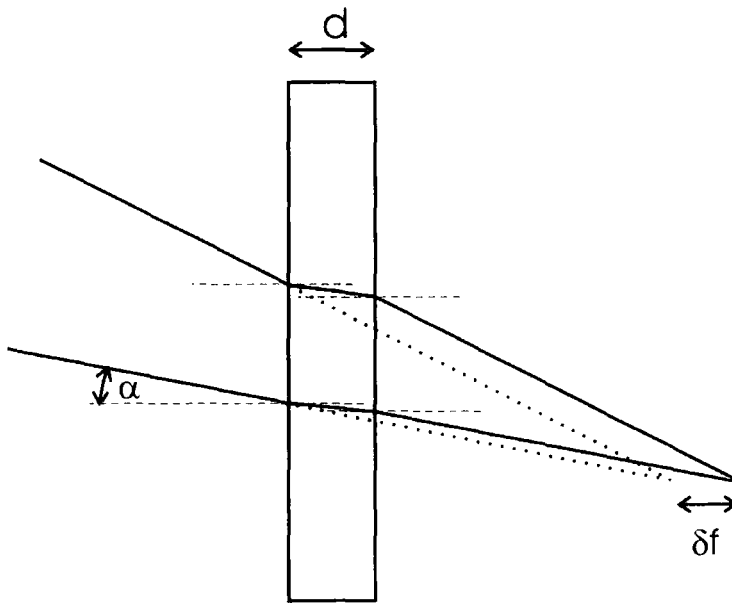
Figure 10.2: A beam focussed through a tilted glass plate focusses to a different point than if the plate were not present.
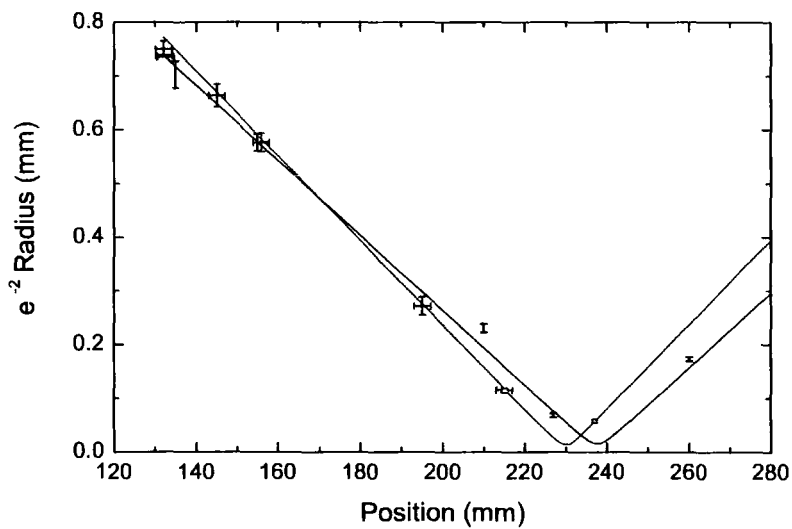
Figure 10.3: Results of knife–edge measurements of the vertical (blue) and horizontal (red) radii of the Nd:YAG beam focussed at 19° to the normal through a 6 mm thick viewport. From the Gaussian beam fits, the focussed beam waists are separated by 8 mm.
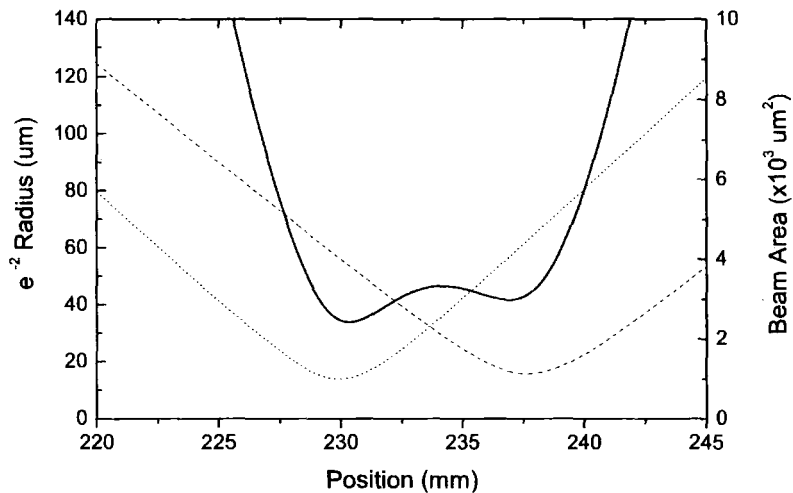
Figure 10.4: Location of the minimum spotsize of Nd:YAG after focussing through the angled viewport. The dotted and dashed lines are the fits from Fig. 10.3 (left axis) while the solid black line is the beam cross–section area at that position (right axis). The double minimum arises due to astigmatism produced by the window the laser is focussed through.

10.2 Overlapping Orthogonal CO_2 and Nd:YAG Lasers

For initial alignment of the Nd:YAG laser the position of the CO_2 lattice was recorded. Two cameras were used to take images of the dipole trap, one camera as shown in Fig. 10.1 and the other looking vertically down through the top ZnSe viewport. The centre of the trap was then found with approximately pixel resolution.

From the measurements described in Fig. 10.3 the position of the lens before the chamber was approximately known. The uncertainty arises due to the difficulty in measuring exactly the position from the MOT centre. To align the Nd:YAG laser use was made of the MOT being at the centre of the vacuum chamber. The beam was adjusted so that it entered and left the vacuum chamber with odd symmetry about the centre. The CO_2 was not used for the next section. The Nd:YAG beam was adjusted until it was observed to trap atoms, as shown in
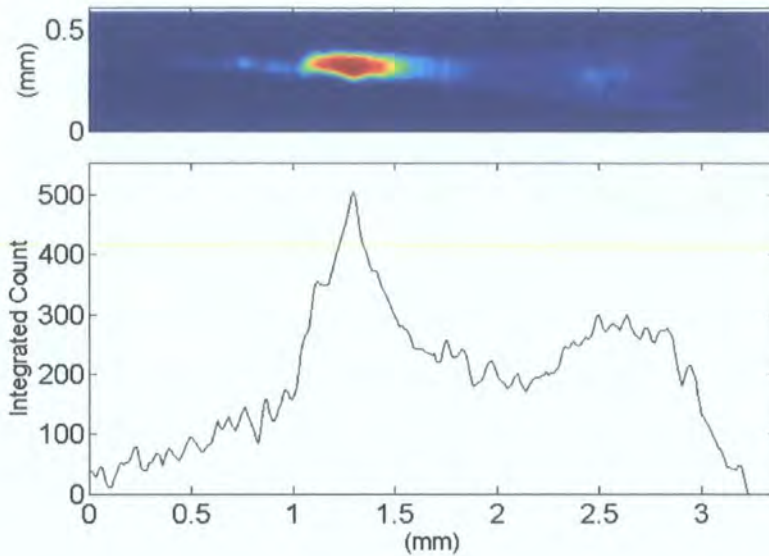
Figure 10.5: **Top)** The Nd:YAG laser as a dipole trap. The laser is focussed in from the left, in this picture. **Bottom)** Integrated pixel count of same image in which two maxima can be seen. The figure was taken with an imaging pulse length of 1 ms.

Fig. 10.5. By binning the image along the beam axis two maxima of the number of trapped atoms are evident. This agrees with the prediction of an astigmatic beam creating a trapping potential with two minima. However, the maxima are separated by 1.3 mm, in clear disagreement with the result shown in Fig 10.4 which predicts a separation of 8 mm. To clarify the situation the beam was modeled using a lens design program, OSLO LT [121]. This software is used for modeling optical systems by ray–tracing and using Gaussian beam ABCD matrices. The model predicted that the focii are separated by 1.6 mm in much better agreement with observations. The minimum beam size was calculated to be 31 μm.

The polarisation of the Nd:YAG laser was aligned with the direction of propagation of the CO_2 laser to ensure the polarisations of the two lasers were orthogonal.

To overlap the lasers the CO_2 trap was loaded with 3×10^5 ^{85}Rb atoms. The Nd:YAG laser was on throughout the loading and trapping phase. After a 60 ms

hold time both CO_2 and Nd:YAG lasers were switched off and a fluorescence image of the trapped cloud taken. The profile was compared to a profile of an atomic sample that was trapped in the CO_2 laser alone to check for localised enhancement in atom density. The position of the Nd:YAG beam focus was then changed and the process repeated. To examine whether a change in the observed profile was a viewing effect due to one beam being behind the other relative to the camera the procedure was repeated. This time the Nd:YAG was switched off completely at the end of the molasses phase. An adapted shutter, Section. 4.9, with a highly reflective Alanod flag was used to deflect the beam into a beam dump immediately after the laser head, turning off the beam in approximately 1 ms. If the beams were not correctly aligned the increased atom number disappeared when the Nd:YAG was switched off at the end of the molasses phase.

10.3   Enhanced Loading

The first observations of enhanced loading were easily identified. Fig. 10.6 shows density profiles of trapped atomic clouds with and without the light–shift engineering Nd:YAG beam on during the MOT and molasses phase. The enhanced region has a peak density of more than a factor of two higher than without light–shift engineering.

By tuning the optical molasses the enhancement can be made more dramatic. For a 10 ms, $\Delta = -20$ MHz molasses a loading enhancement of a factor of four is observed, as shown in Fig. 10.7.

10.4   Temperature of Light–Shift Engineered Region

To measure the temperature a time–of–flight technique was used. The lattice was loaded with 10^5 ^{87}Rb atoms from a MOT with 5×10^7 atoms. The MOT phase was followed by a 10 ms molasses phase with a detuning of $\Delta = -30$ MHz. During the molasses phase the hyperfine repumping laser intensity was lowered

by a factor of 30 and was completely shut off for the final 5 ms. The molasses beams and the Nd:YAG laser were then switched off and the untrapped atoms allowed to fall under gravity. After a 60 ms hold time the CO_2 laser was switched off in $\sim 1~\mu$s and an image of the cloud taken with the now on–resonance MOT beams for varying expansion times up to 400 μs. For each release time six data sets were taken and averaged. Line profiles were taken axially (along the CO_2 axis) through the data and Gaussian fits were made of the light–shift engineered region, see for example Fig. 10.8. A temperature of 380(75) μK was extracted from the data which are plotted in Fig. 10.9.

An attempt was made to measure the temperature of ^{85}Rb in the method described above, but the Gaussian fits could only be made of the light–shift engineered region up to $< 100~\mu$s.
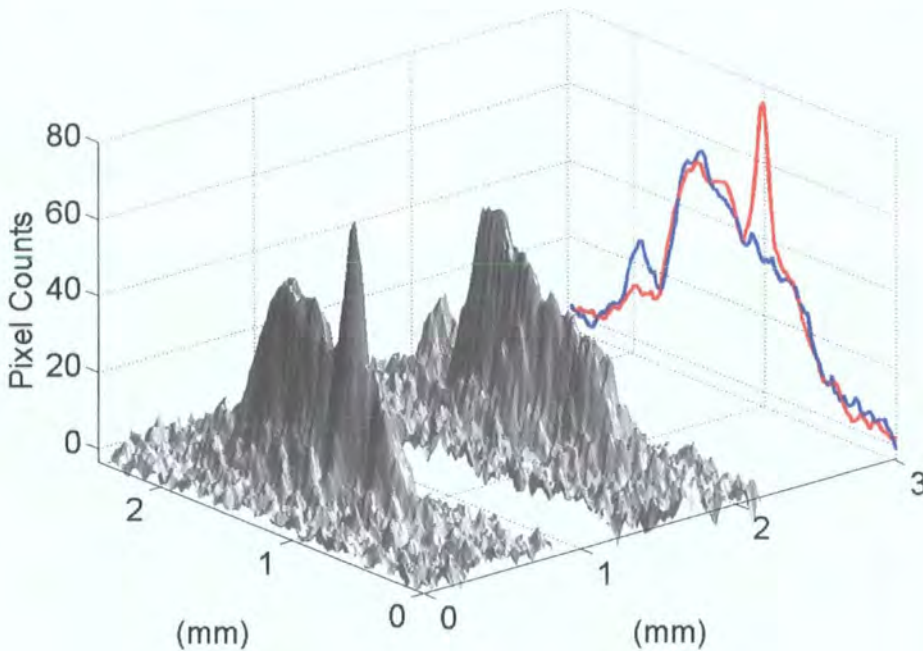
Figure 10.6: Images of the first observation of enhanced loading in a CO_2 laser optical lattice by light–shift engineering. Left) an atomic profile with light–shift engineering and right), without the light–shift engineering beam. Axial line–profiles through each plot are also shown, clearly identifying the enhancement.
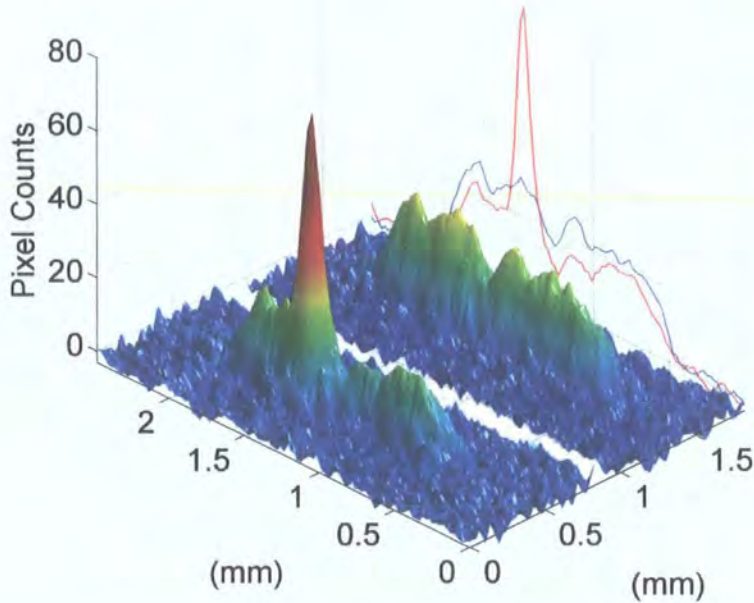
Figure 10.7: For a molasses phase of $\Delta = -20$ MHz the number loaded into the light–shift engineered region is almost four time greater than before.

10.5 Dimple Trick

The experiment described here of a $\lambda = 1.064$ μm laser being used to locally enhance the density of atoms in a CO_2 laser trap seems at least similar to the Cs experiment at Innsbruck [122]. In this experiment a tightly focussed ($w_0 = 30$ μm) Yb fibre laser was used to local increase the phase space density of atoms in a CO_2 laser trap by increasing the density of atoms in the overlapped trapping region. The temperature was maintained approximately constant by using the volume of atoms trapped by the CO_2 laser alone as a thermal reservoir. This technique, the 'dimple trick' had previously been used in the Ketterle group to repeatedly cross the transition to BEC in a magnetically trapped gas by using a red–detuned laser.

To show that the enhanced loading was not merely due to an increased ground state trap depth the intensity of the CO_2 laser was lowered by a factor of four such that the combined trap depth of the CO_2 lattice and Nd:YAG com-
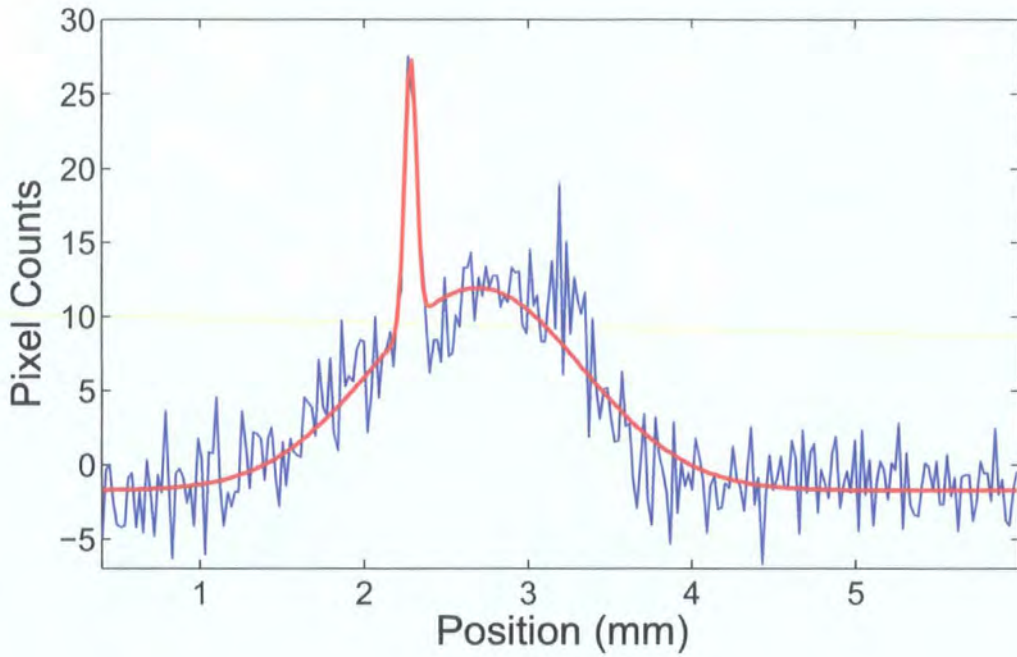
Figure 10.8: Example of double Gaussian fit to optical lattice and light–shift engineered region.
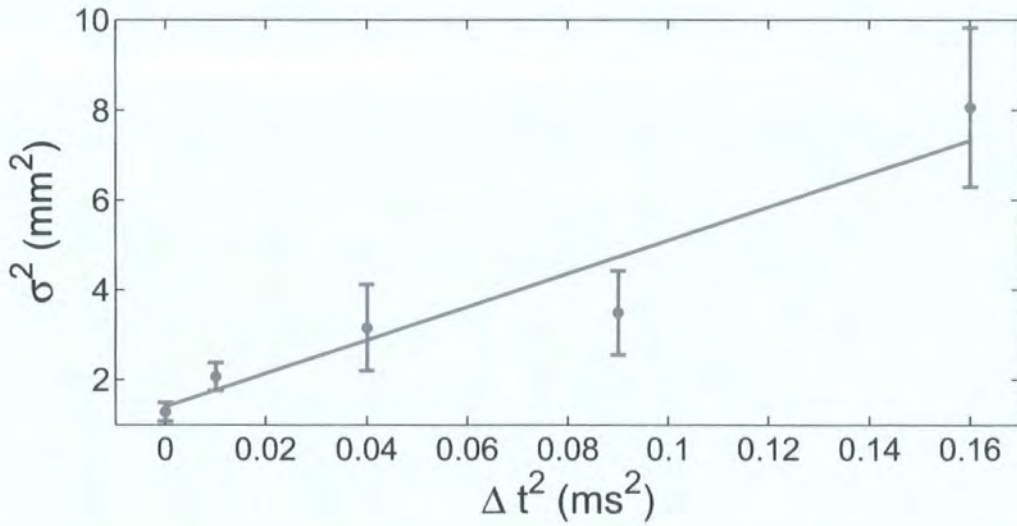
Figure 10.9: Graph of Gaussian widths squared against time–of–flight squared to estimate the temperature of atoms in the light–shift engineered region. The fit yields a temperature of 380(75) μK.

bined ($h \times 27$ MHz)was less than the trap depth of the full CO_2 lattice alone ($h \times 36$ MHz). The peak number of atoms trapped in the full intensity CO_2 lattice was more than a factor of 2 less than in the light–shift engineered region Fig. 10.10.
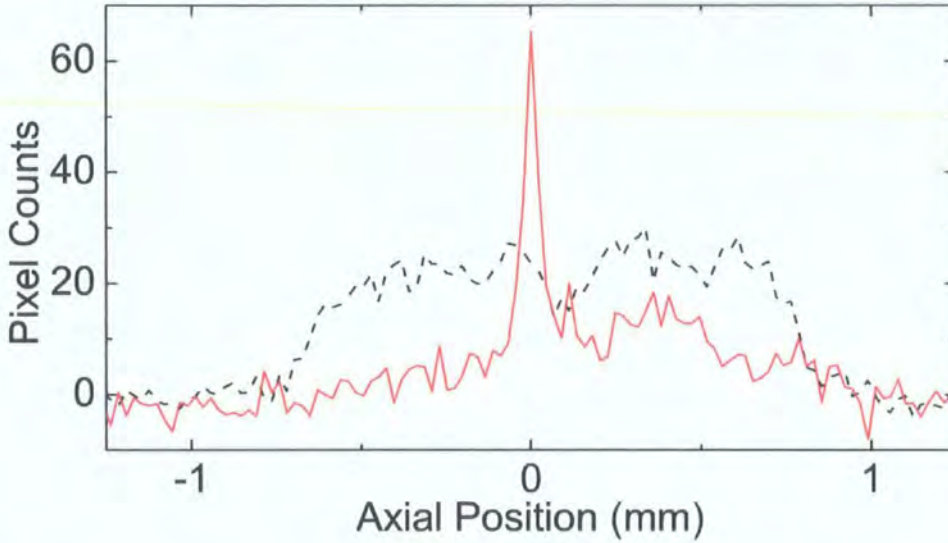
Figure 10.10: Column density for a CO_2 laser lattice without the Nd:YAG laser (dashed line), and for a shallower CO_2 laser lattice with the Nd:YAG laser (solid line). The overall ground state light–shift in the overlap region of the shallow combined trap (-27 MHz) is less than the maximum light-shift for the CO2 laser lattice alone (-36 MHz), but loading into the combined trap is still significantly more efficient. Both profiles are for a molasses detuning of -20 MHz.

10.6   Region–Specific Loading

To prove that the experimental observation of enhanced loading is due to a mechanism beyond the dimple trick a further experiment was conducted. Here the lattice was loaded as before, but now a blue–detuned, $\Delta = +2$ MHz molasses phase was implemented after the MOT phase. Time–of–flight measurements of an untrapped atom cloud after such a molasses phase revealed a temperature of 200(17) μK. When the Nd:YAG laser was overlapped with the CO_2 lattice we observes that loading still occurred in the light–shift engineered region, but nowhere else in the lattice. The shot–to–shot variation in the number of atoms
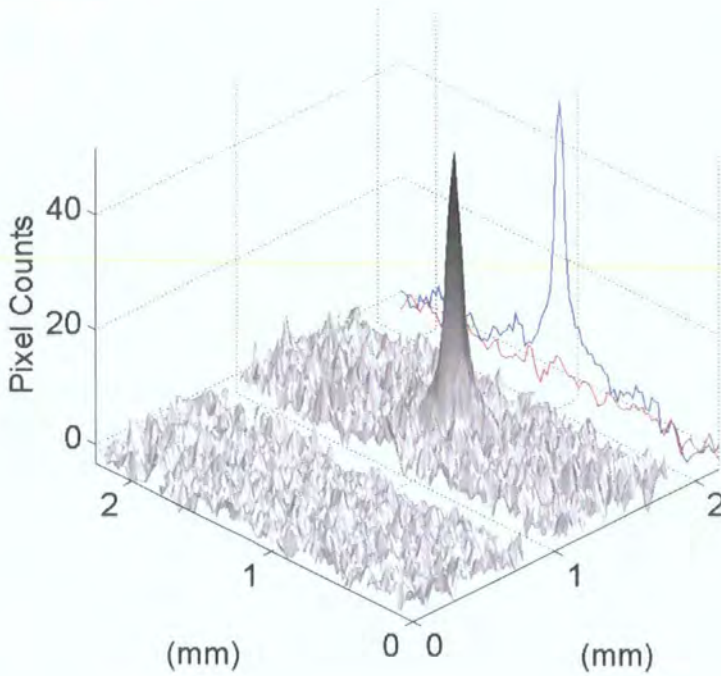
Figure 10.11: Loading only a specific region of an optical molasses by light–shift engineering. The molasses detuning was $\Delta = +2$ MHz for 10 ms.

is significant, though atoms were observed to be loaded each time. The region loaded in Fig. 10.11 is estimated to contain 10^4 atoms, spread over 6 lattice sites.

The density of atoms loaded into selected regions can be higher than for an optical lattice loaded from a standard optical molasses, detuned by $\Delta = -20$ MHz. This effect is shown clearly in Fig. 10.12.

This effect is explained by Fig. 9.1(c), where one of the m_F states is observed to acquire a large effective, additional red detuning.
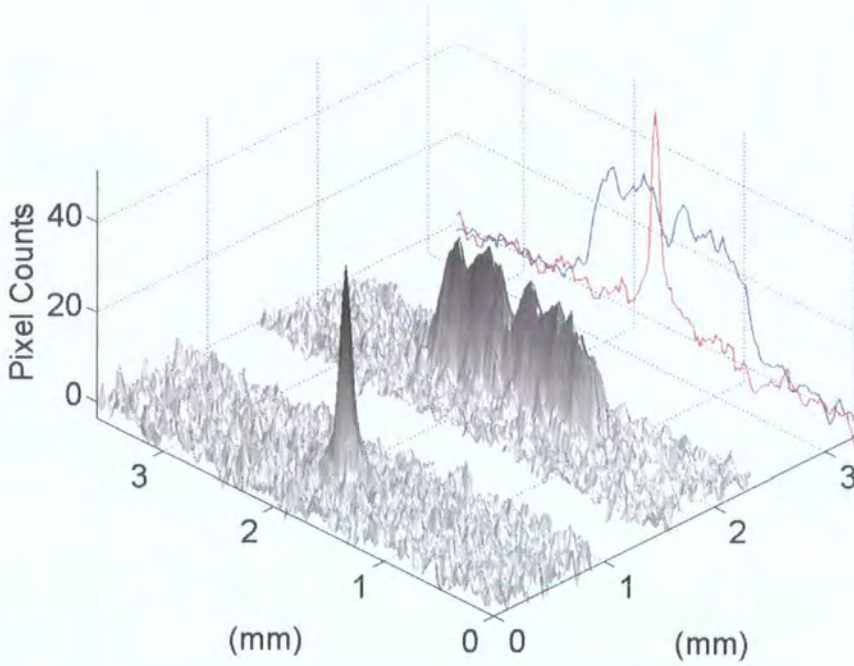
Figure 10.12: Comparison of the result number density of atoms loaded into an optical lattice using spatially selective light–shift engineering (Fig. 10.11) and into a typical optical lattice without light–shift engineering. For the region specific loading a molasses detuning of $\Delta = +2$ MHz was used, compared to $\Delta = -20$ MHz for the normal lattice.

Chapter 11

Status and Future Work

During the course of this work we have developed and built an experiment to laser cool and optically dipole trap rubidium. The entire experiment was designed and constructed during the course of my PhD. We have built a compact vapour cell MOT, developing a new method of making high–quality viewports for use at $\lambda = 10.6$ μm [60]. A novel method of providing a short pulses of alkali atoms while maintaining an ultra–high vacuum has been implemented [88]. We have loaded large numbers of Rb atoms into a CO_2 laser optical dipole trap in single beam and lattice geometries. We have proposed and demonstrated engineering of the light–shift of an excited atomic state. By this method we have increased the number and density of atoms loaded into selected regions of an atomic lattice by more than a factor of three. We have adapted the technique to load only specific regions of an optical lattice.

Wavelength Dependency of Light–Shift Engineering

In the experiments in this thesis we have only examined a light–shift engineering laser field at one wavelength. We have proposed using a high powered, tunable diode laser to investigate the rapidly varying polarizabilities in the region ± 10 nm from the $D2$ line. This experiment would allow accurate measurements of the polarizabilities of the excited and ground states. Much greater enhancements in the loading of optical latices could possibly be observed.

Such a tunable laser has been acquired. A wavemeter has also been bought to map out the wavelength accurately.

Addressing of Single Sites

Loading of individual sites of an optical lattice represents a starting point for proposals for quantum computing using optical lattices. A high resolution lens system has been designed [123] and assembled by Matt Pritchard for use with a newly purchased, low–noise CCD camera.

A 3D CO_2 Laser Optical Lattice

Most interestingly, a next generation experiment has been designed and built in the Adams group. In this experiment a 3D face–centred–cubic (FCC) optical lattice, with a lattice constant > 10 μm will be used to trap Rb. Such a lattice will have extremely high trapping frequencies, on the order of 50 kHz. The differential light–shift at the centre of this lattice would be $\geq$ 100 MHz, which would prevent the loading of atoms in this region. The lattice could be loaded at lower CO_2 laser powers and the intensity ramped up latter. However we have observed that changing the power of the beam to the experiment results in changes of the beam position. Using an appropriately tuned auxiliary laser the differential light–shifts could be manipulated so as to allow efficient loading of the 3D lattice.

Laser Cooling of Calcium to Degeneracy

An experiment on laser cooling of Ca in a 3D CO_2 optical lattice will be constructed in the group of Riis at Strathclyde. A recent proposal suggests that in such a system it is possible to laser cool Ca directly to the ground state of the lattice and hence observe the first BEC of Ca and more importantly, generation of a BEC without deliberate loss of atoms [124].

Results of loading of Ca into a CO_2 laser trap at the Physikalisch-Technische Bundesanstalt (PTB) in Germany indicate that the loading efficiency is less than 0.1%, most probably due to the large scalar polarizability of the excited state in the quasi–electrostatic regime. Increasing the loading efficiency would allow higher densities of Ca atoms to be trapped, representing an improved starting point for experiments.

Appendix A

Knife Edge Measurements of Gaussian Beams

The profile of an ideal Gaussian beam is

$$I(x,y) = I_0 e^{-2x^2/w_x^2} e^{-2y^2/w_y^2}, \tag{A.1}$$

where w_i is the $1/e^2$ radius in the i direction and I_0 is the maximum intensity. The power in the beam is given by

$$P = \int_{-\infty}^{\infty} \int_{-\infty}^{\infty} I(x,y) dy dx \tag{A.2}$$

$$= \frac{\pi}{2} I_0 w_x w_y. \tag{A.3}$$

Consider moving an object, larger than the beam's cross section and with a straight, sharp edge, across the beam as shown in the figure. The straightness of the edge is for ease of the integrals in the calculations below. The reason for having a sharp edge is to define the edge more exactly and not have it depend on the orientation of the edge. As the knife edge moves across the beam the

power measured is now

$$P(X) = P_{total} - \int_{-\infty}^{X} \int_{-\infty}^{\infty} I(x,y) \, dy \, dx \tag{A.4}$$

$$= P_{total} - I_0 \sqrt{\frac{\pi}{2}} \int_{-\infty}^{X} e^{-2x^2/w_x^2} dx \tag{A.5}$$

$$= P_{total} - I_0 \, w_y \sqrt{\frac{\pi}{2}} \left(\int_{-\infty}^{0} e^{-2x^2/w_x^2} dx + \int_{0}^{X} e^{-2x^2/w_x^2} dx \right) \tag{A.6}$$

$$= P_{total} - I_0 \, w_y \sqrt{\frac{\pi}{2}} \left(\sqrt{\frac{\pi}{8}} w_x + \int_{0}^{X} e^{-2x^2/w_x^2} dx \right) \tag{A.7}$$

$$= \frac{P_{total}}{2} - I_0 \, w_y \sqrt{\frac{\pi}{2}} \int_{0}^{X} e^{-2x^2/w_x^2} dx. \tag{A.8}$$

We introduce a change of variable $u^2 = 2x^2/w_x^2 \rightarrow dx = w_x \, du/\sqrt{2}$ such that

$$P(X) = \frac{P_{total}}{2} - \frac{\pi}{4} I_0 \, w_x \, w_y \frac{2}{\sqrt{\pi}} \int_{0}^{u} e^{-u^2} du \ . \tag{A.9}$$

Noting that the definition of the error function is

$$\text{erf}(u) = \frac{2}{\sqrt{\pi}} \int_{0}^{u} e^{-u^2} du \ , \tag{A.10}$$

and making use of the definition of the intensity in a Gaussian beam is

$$I_0 = \frac{2 \, P_{total}}{\pi \, w_x \, w_y} \ , \tag{A.11}$$

we come to

$$P(X) = \frac{P_{total}}{2} \left(1 - \text{erf}\left(\frac{\sqrt{2} \, X}{w_x} \right) \right) \ . \tag{A.12}$$

When fitting to knife edge measurements we plot X vs $P(X)$. Then w_x can be extracted by fitting the data using Eqn. A.12.

Appendix B

Light–Shifts

This appendix shows the derivation of the light–shift of an atomic state when the rotating wave approximation (RWA) is valid.

B.1   Rotating Wave Approximation

We start with the time–dependent Schrödinger equation

$$i\hbar\frac{d\Psi}{dt} = H\Psi \,, \tag{B.1}$$

and expand the wavefunctions, which form a complete set, in the concise Dirac notation

$$\Psi\left(\mathbf{r}, t\right) = \sum_n c_n|n\rangle e^{-i\omega_n t} \,. \tag{B.2}$$

The interaction due to an AC electric field is included as a perturbation,

$$V(t) = -\mathbf{d} \cdot \mathcal{E}_0 \cos(\omega t) \,. \tag{B.3}$$

This perturbation corresponds to the energy of a dipole, $\mathbf{d} = -e\,\mathbf{r}$ in the oscillating electric field, where e is the electronic charge and $\mathbf{r}$ is the displacement of the electron with respect to the atomic centre of mass. The dipole moment is parallel to the electric field. We introduce here the Rabi frequency, Ω, which is defined as,

$$\begin{aligned} \Omega_{\mathrm{mn}} &= \frac{\langle m|\mathbf{d} \cdot \mathcal{E}|n\rangle}{\hbar} \\ &= \frac{e\mathcal{E}_0}{\hbar}\langle m|\mathbf{r}|n\rangle \,. \end{aligned} \tag{B.4}$$

We can further simplify the situation to only consider two atomic states, which will be labelled $|1\rangle$ and $|2\rangle$. Substituting Eqns. B.2 and B.3 into Eqn. B.1 leads to

$$i\dot{c}_1 = \Omega \cos(wt) \, e^{-i\omega_0 t} c_2 \tag{B.5}$$

$$i\dot{c}_2 = \Omega \cos(wt) \, e^{i\omega_0 t} c_1 \, , \tag{B.6}$$

where $\omega_0 = (\omega_2 - \omega_1)$. We re-write these equations in a more convenient form,

$$i\dot{c}_1 = c_2 \frac{\Omega}{2} \left(e^{i(\omega - \omega_0)t} + e^{-i(\omega + \omega_0)t} \right) \tag{B.7}$$

$$i\dot{c}_2 = c_1 \frac{\Omega}{2} \left(e^{i(\omega + \omega_0)t} + e^{-i(\omega - \omega_0)t} \right) \, . \tag{B.8}$$

At this point the rotating wave approximation (RWA) is made and terms that include $\omega + \omega_0$ are dropped [19]. To simplify further we define $\Delta = \omega - \omega_0$. Then,

$$i\dot{c}_1 = c_2 \frac{\Omega}{2} e^{i\Delta t} \tag{B.9}$$

$$i\dot{c}_2 = c_1 \frac{\Omega}{2} e^{-i\Delta t} \, . \tag{B.10}$$

We now define a new set of variables to include the time dependencies,

$$\widetilde{c}_1 = c_1 e^{-i\Delta t/2} \tag{B.11}$$

$$\widetilde{c}_2 = c_2 e^{i\Delta t/2} \, . \tag{B.12}$$

Differentiating Eqns. B.11 and B.12 w.r.t. time, and multiplying by i gives

$$i\dot{\widetilde{c}}_1 = i\dot{c}_1 e^{-i\Delta t/2} + \frac{\Delta}{2} c_1 e^{-i\Delta t/2} \tag{B.13}$$

$$i\dot{\widetilde{c}}_2 = i\dot{c}_2 e^{i\Delta t/2} - \frac{\Delta}{2} c_2 e^{-i\Delta t/2} \, . \tag{B.14}$$

Substituting in Eqns. B.9 – B.12 into these differential equations yields,

$$i\dot{\widetilde{c}}_1 = \frac{1}{2} \left(\widetilde{c}_1 \Delta + \widetilde{c}_2 \Omega \right) \tag{B.15}$$

$$i\dot{\widetilde{c}}_2 = \frac{1}{2} \left(\widetilde{c}_1 \Omega - \widetilde{c}_2 \Delta \right) \, . \tag{B.16}$$

We can now combine Eqns. B.15 and B.16 and write them in matrix form

$$i\frac{\mathrm{d}}{\mathrm{d}t} \begin{pmatrix} \widetilde{c}_1 \\ \widetilde{c}_2 \end{pmatrix} = \begin{pmatrix} \frac{\Delta}{2} & \frac{\Omega}{2} \\ \frac{\Omega}{2} & -\frac{\Delta}{2} \end{pmatrix} \begin{pmatrix} \widetilde{c}_1 \\ \widetilde{c}_2 \end{pmatrix} \, . \tag{B.17}$$

The eigenenergies of the perturbed system are of the form

$$E = \pm \frac{\hbar}{2} \sqrt{\Delta^2 + \Omega^2} \; . \tag{B.18}$$

In the limit that $|\Delta| \gg \Omega$ the energies are

$$E = \pm \frac{\hbar}{2} \left(\Delta + \frac{\Omega^2}{2\,\Delta} \right) \; , \tag{B.19}$$

or an energy shift of the electronic states of

$$\Delta E = \pm \frac{\hbar \Omega^2}{4\Delta} \; , \tag{B.20}$$

as used in Section 6.3.1.

Appendix C

Derivation of Light–Shifts Using a Floquet Approach

We approach the problem from the same starting point as in Appendix B but take a different approach to the problem. Again we start with Eqns. B.1 and B.3. We separate the perturbation, $V(t)$ is into two parts

$$V = V_+ e^{-i\omega t} + V_- e^{i\omega t} , \qquad (C.1)$$

where

$$V_+ = V_- = \frac{\hbar\Omega}{2} . \qquad (C.2)$$

We make us of the Floquet ansatz

$$|\Psi(t)\rangle = e^{-iE_m t/\hbar}|\psi_m(\tau)\rangle \qquad (C.3)$$

with

$$\tau = \omega t \qquad (C.4)$$

and $|\psi_m(\tau)\rangle$ is periodic with period 2π and E_m is defined as the quasi–energy [125].

The new states $|\psi_m(\tau)\rangle$ are expanded as a Fourier expansion

$$|\psi_m(\tau)\rangle = \sum e^{-in\omega t}|\psi_{m,n}\rangle . \qquad (C.5)$$

Substituting Eqns. C.3 and C.5 into Eqn. B.1 we get

$$\hbar\omega \sum e^{-int}|\psi_{m,n}\rangle + \sum n\,\hbar\, e^{-int}|\psi_{m,n}\rangle = H_a \sum e^{-int}|\psi_{m,n}\rangle + \cdots$$
$$V_+ \sum e^{-i(n-1)t}|\psi_{m,n}\rangle + V_- \sum e^{-i(n+1)t}|\psi_{m,n}\rangle \qquad (C.6)$$

This equation should hold for all time. Thus we compare terms oscillating with the same frequency and get the coupled equations

$$(E + n\,\hbar\omega - H_a)\,|\psi_n\rangle = V_+|\psi_{n-1}\rangle + V_-|\psi_{n+1}\rangle \;. \qquad (C.7)$$

C.1   Energy Shifts

Perturbation

From Eqn. C.7 we see that the dipole interaction causes ψ_0 to couple to ψ_{-1} and ψ_1, ψ_1 to couple to ψ_0 and ψ_2, and so on. As the interaction is to be considered as a perturbation, we take it that the field is weak, $\mathcal{E} \to 0$. We also note

$$V_+, V_- \propto \mathcal{E} \qquad (C.8)$$

$$E = E_0 + E^{(1)}\mathcal{E} + E^{(2)}\mathcal{E}^2 + \ldots \qquad (C.9)$$

$$|\psi_n\rangle = |\psi_n^{(0)}\rangle + |\psi_n^{(1)}\rangle\,\mathcal{E} + |\psi_n^{(2)}\rangle\,\mathcal{E}^2 + \ldots \qquad (C.10)$$

To arrive at a solution we substitute for $|\psi_n\rangle$ and E, to the correct order, in Eqn. C.7 and compare terms by the order of $\mathcal{E}$.

Zeroth Order

By definition, the zeroth order energies and wavefunctions correspond to the unperturbed results for solving Eqn. B.1 with $V(t) = 0$. The results are

$$E^{(0)} \equiv E,$$
$$\psi_0^{(0)} = \phi_0, \qquad (C.11)$$
$$\psi_n^{(0)} = 0, \ \ \forall\, n \neq 0$$

C.1.1   First Order

<u>n=0</u>

$$E^{(1)}\psi_0^{(0)} + \left(E^{(0)} + 0\hbar\omega - H_a\right)\psi_0^{(1)} = V_+\psi_{-1}^{(0)} + V_-\psi_1^{(0)} \qquad (C.12)$$

Projecting onto $\psi_0^{(0)}$

$$E^{(1)}\langle\psi_0^{(0)}|\psi_0^{(0)}\rangle + \langle\psi_0^{(0)}|E^{(0)} - H_a|\psi_0^{(1)}\rangle = 0 \qquad (C.13)$$

As the second term is zero, we see that there is no first order shift.

<u>n=±1</u>.

Working from

$$\left(E^{(0)} + \hbar\omega - H_a\right)\psi_1^{(1)} = V_+\psi_0^{(0)} + V_-\psi_2^{(0)} \tag{C.14}$$

we can show that

$$\Rightarrow |\psi_{\pm 1}^{(1)}\rangle = G\left(E^{(0)} \pm \hbar\omega\right) V_\pm |\psi_0^{(0)}\rangle\,, \tag{C.15}$$

where we have defined the Green's function

$$G\left(E^{(0)} \pm \hbar\omega\right) = \frac{1}{E^{(0)} \pm \hbar\omega - H_a} \tag{C.16}$$

C.1.2   Second Order

<u>n=0</u>

$$E^{(2)}\psi_0^{(0)} + \left(E^{(0)} + 0\hbar\omega - H_a\right)\psi_0^{(2)} = V_+\psi_{-1}^{(1)} + V_-\psi_1^{(1)} \tag{C.17}$$

and as before we project onto $\psi_0^{(0)}$ and remove the terms that go to zero.

$$\Rightarrow E^{(2)} = \langle\psi_0^{(0)}|V_+|\psi_{-1}^{(1)}\rangle + \langle\psi_0^{(0)}|V_-|\psi_1^{(1)}\rangle\,. \tag{C.18}$$

Substituting Eqn. C.15

$$\begin{aligned}\Rightarrow E^{(2)} = {} & \langle\psi_0^{(0)}|V_+G\left(E^{(0)} - \hbar\omega\right) V_-|\psi_0^{(0)}\rangle + \\ & \langle\psi_0^{(0)}|V_-G\left(E^{(0)} + \hbar\omega\right) V_+|\psi_0^{(0)}\rangle\,. \end{aligned} \tag{C.19}$$

This equation says that the second order shift is due to two terms: the first term on the RHS is due to an atom emitting a photon and then absorbing a photon. The second term is due to an emission followed by absorption.

The Green's function, Eqn. C.16 can be presented in a more useful form

$$\frac{1}{E^{(0)} \pm \hbar\omega - H_a} = \sum_k \frac{|k\rangle\langle k|}{E_0 - E_k \pm \hbar\omega}\,. \tag{C.20}$$

This equation can be proved by making use of the closure relation $\sum_k |k\rangle\langle k| = \mathbb{1}$ in the following way.

$$|\psi_k\rangle = \frac{|k\rangle}{E^{(0)} \pm \hbar\omega - H_a}$$

$$\Rightarrow \qquad (E^{(0)} \pm \hbar\omega - H_a)|\psi_k\rangle = |k\rangle$$

$$\Rightarrow \quad \sum_{k'}(E^{(0)} \pm \hbar\omega - H_a)|k'\rangle\langle k'|\psi_k\rangle = |k\rangle$$

$$\Rightarrow \quad \sum_{k'}(E^{(0)} \pm \hbar\omega - E_{k'})|k'\rangle\langle k'|\psi_k\rangle = |k\rangle$$

$$\Rightarrow \quad (E^{(0)} \pm \hbar\omega - E_k)\langle k|k\rangle\langle k|\psi_k\rangle = \langle k|k\rangle$$

$$\Rightarrow \quad (E^{(0)} \pm \hbar\omega - E_k)\langle k|\psi_k\rangle = 1$$

$$\Rightarrow \qquad\qquad \langle k|\psi_k\rangle = \frac{1}{E^{(0)} \pm \hbar\omega - E_k}$$

$$\Rightarrow \qquad\qquad |\psi_k\rangle = \frac{|k\rangle}{E^{(0)} \pm \hbar\omega - E_k}$$

Inserting Eqn. C.20 into Eqn. C.19

$$\Rightarrow E^{(2)} = \sum_k \frac{\langle\psi_0^{(0)}|V_+|k\rangle\langle k|V_-|\psi_0^{(0)}\rangle}{E_0 - E_k - \hbar\omega} + \frac{\langle\psi_0^{(0)}|V_-|k\rangle\langle k|V_+|\psi_0^{(0)}\rangle}{E_0 - E_k + \hbar\omega} \qquad (C.21)$$

$$= \sum_k \frac{\left|\langle\psi_0^{(0)}|V_+|k\rangle\right|^2}{\hbar}\left(\frac{1}{\omega_0 - \omega} + \frac{1}{\omega_0 + \omega}\right) , \qquad (C.22)$$

where $\hbar\omega_0 = E_k - E_0$. Using Eqn. C.2 Eqn. C.22 can now be finally written as

$$E^{(2)} = \frac{\hbar\Omega^2}{4}\left(\frac{1}{\omega_0 - \omega} + \frac{1}{\omega_0 + \omega}\right) . \qquad (C.23)$$

For a red-detuned laser the first term in the brackets is negative and dominates as $\omega_0 - \omega < \omega_0 + \omega$. Thus the energy shift is negative and the effect is to lower the atomic states energy.

Appendix D

Examples of the Q–Matrix

This appendix includes the Q–matrices calculated for the $5P_{3/2}$ state of Rb, evaluated from Eqn. 6.39. For this level $J = 3/2$ and F ranges from 1 to 4. The form of the matrices are as shown in Fig. 6.6.

On the next pages are examples of the Q–matrix of Eqn. 6.39 for the $5P_{3/2}$ state of Rb for the laser field polarised along z, Eqn. D.1, and secondly x, Eqn. D.2.

$$
\begin{pmatrix}
1 & 0 & 0 & 0 & 0 & 0 & 0 & 0 & 0 & 0 & 0 & 0 & 0 & 0 & 0 & 0 & 0 & 0 & 0 & 0 & 0 & 0 & 0 & 0 \\
0 & \tfrac{1}{4} & \tfrac{-\sqrt{15}}{4} & 0 & 0 & 0 & 0 & 0 & 0 & 0 & 0 & 0 & 0 & 0 & 0 & 0 & 0 & 0 & 0 & 0 & 0 & 0 & 0 & 0 \\
0 & \tfrac{-\sqrt{15}}{4} & -\left(\tfrac{1}{4}\right) & 0 & 0 & 0 & 0 & 0 & 0 & 0 & 0 & 0 & 0 & 0 & 0 & 0 & 0 & 0 & 0 & 0 & 0 & 0 & 0 & 0 \\
0 & 0 & 0 & -\left(\tfrac{2}{7}\right) & -\sqrt{\tfrac{5}{7}} & \tfrac{\sqrt{10}}{7} & 0 & 0 & 0 & 0 & 0 & 0 & 0 & 0 & 0 & 0 & 0 & 0 & 0 & 0 & 0 & 0 & 0 & 0 \\
0 & 0 & 0 & -\sqrt{\tfrac{5}{7}} & 0 & -\sqrt{\tfrac{2}{7}} & 0 & 0 & 0 & 0 & 0 & 0 & 0 & 0 & 0 & 0 & 0 & 0 & 0 & 0 & 0 & 0 & 0 & 0 \\
0 & 0 & 0 & \tfrac{\sqrt{10}}{7} & -\sqrt{\tfrac{2}{7}} & -\left(\tfrac{5}{7}\right) & 0 & 0 & 0 & 0 & 0 & 0 & 0 & 0 & 0 & 0 & 0 & 0 & 0 & 0 & 0 & 0 & 0 & 0 \\
0 & 0 & 0 & 0 & 0 & 0 & -\left(\tfrac{17}{28}\right) & \tfrac{-5}{4\sqrt7} & \tfrac{2\sqrt5}{7} & 0 & 0 & 0 & 0 & 0 & 0 & 0 & 0 & 0 & 0 & 0 & 0 & 0 & 0 & 0 \\
0 & 0 & 0 & 0 & 0 & 0 & \tfrac{-5}{4\sqrt7} & \tfrac{3}{20} & \tfrac{-2}{\sqrt{35}} & \tfrac{4}{5} & 0 & 0 & 0 & 0 & 0 & 0 & 0 & 0 & 0 & 0 & 0 & 0 & 0 & 0 \\
0 & 0 & 0 & 0 & 0 & 0 & \tfrac{2\sqrt5}{7} & \tfrac{-2}{\sqrt{35}} & \tfrac{5}{14} & \tfrac{\sqrt{7/5}}{2} & 0 & 0 & 0 & 0 & 0 & 0 & 0 & 0 & 0 & 0 & 0 & 0 & 0 & 0 \\
0 & 0 & 0 & 0 & 0 & 0 & 0 & \tfrac{4}{5} & \tfrac{\sqrt{7/5}}{2} & \tfrac{1}{10} & 0 & 0 & 0 & 0 & 0 & 0 & 0 & 0 & 0 & 0 & 0 & 0 & 0 & 0 \\
0 & 0 & 0 & 0 & 0 & 0 & 0 & 0 & 0 & 0 & -\left(\tfrac{5}{7}\right) & 0 & \tfrac{2\sqrt6}{7} & 0 & 0 & 0 & 0 & 0 & 0 & 0 & 0 & 0 & 0 & 0 \\
0 & 0 & 0 & 0 & 0 & 0 & 0 & 0 & 0 & 0 & 0 & \tfrac{1}{5} & 0 & \tfrac{2\sqrt6}{5} & 0 & 0 & 0 & 0 & 0 & 0 & 0 & 0 & 0 & 0 \\
0 & 0 & 0 & 0 & 0 & 0 & 0 & 0 & 0 & 0 & \tfrac{2\sqrt6}{7} & 0 & \tfrac{5}{7} & 0 & 0 & 0 & 0 & 0 & 0 & 0 & 0 & 0 & 0 & 0 \\
0 & 0 & 0 & 0 & 0 & 0 & 0 & 0 & 0 & 0 & 0 & \tfrac{2\sqrt6}{5} & 0 & -\left(\tfrac{1}{5}\right) & 0 & 0 & 0 & 0 & 0 & 0 & 0 & 0 & 0 & 0 \\
0 & 0 & 0 & 0 & 0 & 0 & 0 & 0 & 0 & 0 & 0 & 0 & 0 & 0 & -\left(\tfrac{17}{28}\right) & \tfrac{5}{4\sqrt7} & \tfrac{2\sqrt5}{7} & 0 & 0 & 0 & 0 & 0 & 0 & 0 \\
0 & 0 & 0 & 0 & 0 & 0 & 0 & 0 & 0 & 0 & 0 & 0 & 0 & 0 & \tfrac{5}{4\sqrt7} & \tfrac{3}{20} & \tfrac{2}{\sqrt{35}} & \tfrac{4}{5} & 0 & 0 & 0 & 0 & 0 & 0 \\
0 & 0 & 0 & 0 & 0 & 0 & 0 & 0 & 0 & 0 & 0 & 0 & 0 & 0 & \tfrac{2\sqrt5}{7} & \tfrac{2}{\sqrt{35}} & \tfrac{5}{14} & \tfrac{-\sqrt{7/5}}{2} & 0 & 0 & 0 & 0 & 0 & 0 \\
0 & 0 & 0 & 0 & 0 & 0 & 0 & 0 & 0 & 0 & 0 & 0 & 0 & 0 & 0 & \tfrac{4}{5} & \tfrac{-\sqrt{7/5}}{2} & \tfrac{1}{10} & 0 & 0 & 0 & 0 & 0 & 0 \\
0 & 0 & 0 & 0 & 0 & 0 & 0 & 0 & 0 & 0 & 0 & 0 & 0 & 0 & 0 & 0 & 0 & 0 & -\left(\tfrac{2}{7}\right) & \sqrt{\tfrac{5}{7}} & \tfrac{\sqrt{10}}{7} & 0 & 0 & 0 \\
0 & 0 & 0 & 0 & 0 & 0 & 0 & 0 & 0 & 0 & 0 & 0 & 0 & 0 & 0 & 0 & 0 & 0 & \sqrt{\tfrac{5}{7}} & 0 & \sqrt{\tfrac{2}{7}} & 0 & 0 & 0 \\
0 & 0 & 0 & 0 & 0 & 0 & 0 & 0 & 0 & 0 & 0 & 0 & 0 & 0 & 0 & 0 & 0 & 0 & \tfrac{\sqrt{10}}{7} & \sqrt{\tfrac{2}{7}} & -\left(\tfrac{5}{7}\right) & 0 & 0 & 0 \\
0 & 0 & 0 & 0 & 0 & 0 & 0 & 0 & 0 & 0 & 0 & 0 & 0 & 0 & 0 & 0 & 0 & 0 & 0 & 0 & 0 & \tfrac{1}{4} & \tfrac{\sqrt{15}}{4} & 0 \\
0 & 0 & 0 & 0 & 0 & 0 & 0 & 0 & 0 & 0 & 0 & 0 & 0 & 0 & 0 & 0 & 0 & 0 & 0 & 0 & 0 & \tfrac{\sqrt{15}}{4} & -\left(\tfrac{1}{4}\right) & 0 \\
0 & 0 & 0 & 0 & 0 & 0 & 0 & 0 & 0 & 0 & 0 & 0 & 0 & 0 & 0 & 0 & 0 & 0 & 0 & 0 & 0 & 0 & 0 & 1
\end{pmatrix}
\tag{D.1}
$$

$$
\scriptsize
\left(
\begin{array}{cccccccccccccccccccccccc}
1 & 0 & 0 & 0 & 0 & 0 & 0 & 0 & 0 & 0 & 0 & 0 & 0 & 0 & 0 & 0 & 0 & 0 & 0 & 0 & 0 & 0 & 0 & 0\\[2pt]
-\tfrac12 & 0 & 0 & \tfrac{3}{4\sqrt7} & \tfrac{\sqrt5}{4} & \sqrt{\tfrac{5}{14}} & 0 & 0 & 0 & 0 & 0 & 0 & 0 & 0 & 0 & 0 & 0 & 0 & 0 & 0 & 0 & 0 & 0 & 0\\[2pt]
0 & -\tfrac18 & \tfrac{\sqrt{15}}{8} & 0 & 0 & 0 & \tfrac{9}{8\sqrt7} & \tfrac58 & \tfrac12\sqrt{\tfrac52} & 0 & 0 & 0 & 0 & 0 & 0 & 0 & 0 & 0 & 0 & 0 & 0 & 0 & 0 & 0\\[2pt]
0 & \tfrac{\sqrt{15}}{8} & \tfrac18 & 0 & 0 & 0 & -\tfrac18\sqrt{\tfrac{15}{7}} & -\tfrac18\sqrt{\tfrac35} & \tfrac12\sqrt{\tfrac32} & \sqrt{\tfrac35} & 0 & 0 & 0 & 0 & 0 & 0 & 0 & 0 & 0 & 0 & 0 & 0 & 0 & 0\\[2pt]
\tfrac{3}{4\sqrt7} & 0 & 0 & \tfrac17 & \tfrac12\sqrt{\tfrac52} & -\tfrac{\sqrt5}{7} & 0 & 0 & 0 & 0 & \tfrac{9}{28}\sqrt{\tfrac52} & \tfrac54\sqrt{\tfrac{3}{14}} & \tfrac{\sqrt{15}}{14} & 0 & 0 & 0 & 0 & 0 & 0 & 0 & 0 & 0 & 0 & 0\\[2pt]
\tfrac{\sqrt5}{4} & 0 & 0 & \tfrac12\sqrt{\tfrac52} & 0 & \tfrac{1}{\sqrt{14}} & 0 & 0 & 0 & 0 & -\tfrac{5}{4\sqrt{14}} & -\tfrac14\sqrt{\tfrac{3}{10}} & \tfrac12\sqrt{\tfrac32} & \tfrac{1}{\sqrt5} & 0 & 0 & 0 & 0 & 0 & 0 & 0 & 0 & 0 & 0\\[2pt]
\sqrt{\tfrac{5}{14}} & 0 & 0 & -\tfrac17\sqrt{\tfrac52} & \tfrac{1}{\sqrt{14}} & \tfrac{5}{14} & 0 & 0 & 0 & 0 & \tfrac{1}{14} & -\tfrac12\sqrt{\tfrac35} & -\tfrac{5}{14}\sqrt{\tfrac32} & \tfrac12\sqrt{\tfrac{7}{10}} & 0 & 0 & 0 & 0 & 0 & 0 & 0 & 0 & 0 & 0\\[2pt]
0 & \tfrac{9}{8\sqrt7} & -\tfrac{\sqrt{15}}{8} & 0 & 0 & 0 & \tfrac{17}{56} & \tfrac{5}{8\sqrt7} & -\tfrac{\sqrt5}{7} & 0 & 0 & 0 & 0 & 0 & \tfrac{15}{28} & \tfrac{5}{4\sqrt7} & \tfrac{\sqrt5}{14} & 0 & 0 & 0 & 0 & 0 & 0 & 0\\[2pt]
0 & \tfrac58 & -\tfrac18\sqrt{\tfrac35} & 0 & 0 & 0 & \tfrac{5}{8\sqrt7} & -\tfrac{3}{40} & \tfrac{1}{\sqrt{35}} & -\tfrac25 & 0 & 0 & 0 & 0 & -\tfrac{5}{4\sqrt7} & -\tfrac{3}{20} & \tfrac{3}{2\sqrt{35}} & \tfrac15 & 0 & 0 & 0 & 0 & 0 & 0\\[2pt]
0 & \tfrac12\sqrt{\tfrac52} & \tfrac12\sqrt{\tfrac32} & 0 & 0 & 0 & -\tfrac{\sqrt5}{7} & \tfrac{1}{\sqrt{35}} & -\tfrac{5}{28} & -\tfrac{\sqrt5}{4} & 0 & 0 & 0 & 0 & \tfrac{\sqrt5}{14} & -\tfrac{3}{2\sqrt{35}} & -\tfrac{15}{28} & -\tfrac14\sqrt{\tfrac75} & 0 & 0 & 0 & 0 & 0 & 0\\[2pt]
0 & 0 & \sqrt{\tfrac35} & 0 & 0 & 0 & 0 & -\tfrac25 & -\tfrac{\sqrt5}{4} & -\tfrac{1}{20} & 0 & 0 & 0 & 0 & 0 & \tfrac15 & \tfrac14\sqrt{\tfrac75} & \tfrac{3}{20} & 0 & 0 & 0 & 0 & 0 & 0\\[2pt]
0 & 0 & 0 & \tfrac{9}{28}\sqrt{\tfrac52} & -\tfrac{5}{4\sqrt{14}} & \tfrac{1}{14} & 0 & 0 & 0 & 0 & \tfrac{5}{14} & 0 & -\tfrac{\sqrt6}{7} & 0 & 0 & 0 & 0 & 0 & \tfrac{9}{28}\sqrt{\tfrac52} & \tfrac{5}{4\sqrt{14}} & \tfrac{1}{14} & 0 & 0 & 0\\[2pt]
0 & 0 & 0 & \tfrac54\sqrt{\tfrac{3}{14}} & -\tfrac14\sqrt{\tfrac{3}{10}} & \tfrac12\sqrt{\tfrac32} & 0 & 0 & 0 & 0 & 0 & -\tfrac{1}{10} & 0 & -\tfrac{\sqrt6}{5} & 0 & 0 & 0 & 0 & \tfrac54\sqrt{\tfrac{3}{14}} & -\tfrac14\sqrt{\tfrac{3}{10}} & -\tfrac12\sqrt{\tfrac32} & 0 & 0 & 0\\[2pt]
0 & 0 & 0 & \tfrac{\sqrt{15}}{14} & \tfrac12\sqrt{\tfrac32} & -\tfrac{5}{14}\sqrt{\tfrac32} & 0 & 0 & 0 & 0 & -\tfrac{\sqrt6}{7} & 0 & -\tfrac{5}{14} & 0 & 0 & 0 & 0 & 0 & \tfrac{\sqrt{15}}{14} & -\tfrac12\sqrt{\tfrac32} & -\tfrac{5}{14}\sqrt{\tfrac32} & 0 & 0 & 0\\[2pt]
0 & 0 & 0 & 0 & \tfrac{1}{\sqrt5} & -\tfrac12\sqrt{\tfrac{7}{10}} & 0 & 0 & 0 & 0 & 0 & -\tfrac{\sqrt6}{5} & 0 & \tfrac{1}{10} & 0 & 0 & 0 & 0 & 0 & \tfrac{1}{\sqrt5} & -\tfrac12\sqrt{\tfrac{7}{10}} & 0 & 0 & 0\\[2pt]
0 & 0 & 0 & 0 & 0 & 0 & \tfrac{15}{28} & -\tfrac{5}{4\sqrt7} & \tfrac{\sqrt5}{14} & 0 & 0 & 0 & 0 & 0 & \tfrac{17}{56} & -\tfrac{5}{8\sqrt7} & -\tfrac{\sqrt5}{7} & 0 & 0 & 0 & 0 & \tfrac{9}{8\sqrt7} & \tfrac{\sqrt{15}}{8} & 0\\[2pt]
0 & 0 & 0 & 0 & 0 & 0 & \tfrac{5}{4\sqrt7} & -\tfrac{3}{20} & -\tfrac{3}{2\sqrt{35}} & \tfrac15 & 0 & 0 & 0 & 0 & -\tfrac{5}{8\sqrt7} & -\tfrac{3}{40} & -\tfrac{1}{\sqrt{35}} & -\tfrac25 & 0 & 0 & 0 & -\tfrac58 & -\tfrac18\sqrt{\tfrac35} & 0\\[2pt]
0 & 0 & 0 & 0 & 0 & 0 & \tfrac{\sqrt5}{14} & \tfrac{3}{2\sqrt{35}} & -\tfrac{15}{28} & \tfrac14\sqrt{\tfrac75} & 0 & 0 & 0 & 0 & -\tfrac{\sqrt5}{7} & -\tfrac{1}{\sqrt{35}} & -\tfrac{5}{28} & \tfrac14\sqrt{\tfrac75} & 0 & 0 & 0 & \tfrac12\sqrt{\tfrac52} & -\tfrac12\sqrt{\tfrac32} & \sqrt{\tfrac35}\\[2pt]
0 & 0 & 0 & 0 & 0 & 0 & 0 & 0 & 0 & 0 & \tfrac{9}{28}\sqrt{\tfrac52} & -\tfrac54\sqrt{\tfrac{3}{14}} & \tfrac{\sqrt{15}}{14} & 0 & 0 & 0 & 0 & 0 & \tfrac17 & -\tfrac12\sqrt{\tfrac52} & -\tfrac{\sqrt5}{7} & 0 & 0 & \tfrac{3}{4\sqrt7}\\[2pt]
0 & 0 & 0 & 0 & 0 & 0 & 0 & 0 & 0 & 0 & \tfrac{5}{4\sqrt{14}} & -\tfrac14\sqrt{\tfrac{3}{10}} & -\tfrac12\sqrt{\tfrac32} & \tfrac{1}{\sqrt5} & 0 & 0 & 0 & 0 & -\tfrac12\sqrt{\tfrac52} & 0 & -\tfrac{1}{\sqrt{14}} & 0 & 0 & -\tfrac{\sqrt5}{4}\\[2pt]
0 & 0 & 0 & 0 & 0 & 0 & 0 & 0 & 0 & 0 & \tfrac{1}{14} & \tfrac12\sqrt{\tfrac35} & \tfrac{5}{14}\sqrt{\tfrac32} & \tfrac12\sqrt{\tfrac{7}{10}} & 0 & 0 & 0 & 0 & -\tfrac12\sqrt{\tfrac52} & -\tfrac{1}{\sqrt{14}} & \tfrac{5}{14} & 0 & 0 & \sqrt{\tfrac{5}{14}}\\[2pt]
0 & 0 & 0 & 0 & 0 & 0 & 0 & 0 & 0 & 0 & 0 & 0 & 0 & 0 & \tfrac{9}{8\sqrt7} & -\tfrac58 & \tfrac12\sqrt{\tfrac52} & 0 & 0 & 0 & 0 & -\tfrac18 & -\tfrac{\sqrt{15}}{8} & 0\\[2pt]
0 & 0 & 0 & 0 & 0 & 0 & 0 & 0 & 0 & 0 & 0 & 0 & 0 & 0 & \tfrac18\sqrt{\tfrac{15}{7}} & -\tfrac18\sqrt{\tfrac35} & -\tfrac12\sqrt{\tfrac32} & \sqrt{\tfrac35} & 0 & 0 & 0 & -\tfrac{\sqrt{15}}{8} & \tfrac18 & 0\\[2pt]
0 & 0 & 0 & 0 & 0 & 0 & 0 & 0 & 0 & 0 & 0 & 0 & 0 & 0 & 0 & 0 & 0 & 0 & \tfrac{3}{4\sqrt7} & -\tfrac{\sqrt5}{4} & \sqrt{\tfrac{5}{14}} & 0 & 0 & -\tfrac12
\end{array}
\right)
$$

$$(D.2)$$

Bibliography

[1] S. Chu, *The manipulation of neutral particles*, Rev. Mod. Phys. **70**, 685 (1998).

[2] C. N. Cohen-Tannoudji, *Manipulating atoms with photons*, Rev. Mod. Phys. **70**, 707 (1998).

[3] W. D. Phillips, *Laser cooling and trapping of neutral atoms*, Rev. Mod. Phys. **70**, 721 (1998).

[4] C. S. Adams and E. Riis, *Laser Cooling and Trapping of Neutral Atoms*, Prog. Quant. Electron. **21**, 1 (1997).

[5] C. Adams, M. Sigel, and J. Mlynek, *Atom optics*, Phys. Rep. **240**, 143 (1994).

[6] E. A. Hinds and I. G. Hughes, *Magnetic atom optics: mirrors, guides, traps and chips for atoms*, J. Phys. D **32**, R119 (1999).

[7] P. S. Jessen and I. H. Deutsch, *Optical Lattices*, Adv. Atom. Mol. Opt. Phys **37**, 95 (1996).

[8] C. Liu, Z. Dutton, C. H. Behroozi, and L. V. Hau, *Observation of coherent optical information storage in an atomic medium using halted light pulses*, Nature **409**, 490 (2001).

[9] M. Takamoto, F.-L. Hong, R. Higashi, and H. Katori, *An optical lattice clock*, Nature **435**, 321 (2005).

[10] M. H. Anderson, J. R. Ensher, M. R. Matthews, C. E. Wieman, and E. A. Cornell, *Observation of Bose–Einstein Condensation in a Dilute Atomic Vapor*, Science **269**, 198 (1995).

[11] K. B. Davis *et al.*, *Bose-Einstein Condensation in a Gas of Sodium Atoms*, Phys. Rev. Lett. **75**, 3969 (1995).

[12] C. C. Bradley, C. A. Sackett, J. J. Tollett, and R. G. Hulet, *Evidence of Bose-Einstein Condensation in an Atomic Gas with Attractive Interactions*, Phys. Rev. Lett. **75**, 1687 (1995).

[13] B. DeMarco and D. S. Jin, *Onset of Fermi Degeneracy in a Trapped Atomic Gas*, Science **285**, 1703 (1999).

[14] S. Chu, L. Hollberg, J. E. Bjorkholm, A. Cable, and A. Ashkin, *Three-dimensional viscous confinement and cooling of atoms by resonance radiation pressure*, Phys. Rev. Lett **55**, 48 (1985).

[15] E. L. Raab, M. Prentiss, A. Cable, S. Chu, and D. E. Pritchard, *Trapping of neutral sodium atoms with radiation pressure*, Phys. Rev. Lett. **59**, 2631 (1987).

[16] A. Ashkin, *Trapping of Atoms by Resonance Radiation Pressure*, Phys. Rev. Lett. **40**, 729 (1978).

[17] J. P. Gordon and A. Ashkin, *Motion of atoms in a radiation trap*, Phys. Rev. A **21**, 1606 (1980).

[18] R. Grimm, M. Weidemüller, and Y. B. Ovchinnikov, *Optical Dipole Traps for Neutral Atoms*, Adv. Atom. Mol. Opt. Phys **42**, 95 (2000).

[19] C. Cohen-Tannoudji, J. Dupont-Roc, and G. Grynberg, *Aton-Photon Interactions* (Wiley, 1998).

[20] J. R. P. Angel and P. G. H. Sanders, *The Hyperfine Structure Stark Effect; I. Theory*, Proc. Roy. Soc. A. **305**, 125 (1968).

[21] A. Ashkin and J. P. Gordon, *Cooling and trapping of atoms by resonance radiation pressure*, Opt. Lett. **4**, 161 (1979).

[22] J. D. Miller, R. A. Cline, and D. J. Heinzen, *Far-off-resonance optical trapping of atoms*, Phys. Rev. A **47**, R4567 (1993).

[23] T. Takekoshi, J. R. Yeh, and R. J. Knize, *Quasi-electrostatic trap for neutral atoms*, Opt. Comm. **114**, 421 (1995).

[24] T. Takekoshi and R. J. Knize, *Co_2 laser trap for cesium atoms*, Optics Lett. **21**, 77 (1996).

[25] A. Marte *et al.*, *Feshbach Resonances in Rubidium 87: Precision Measurement and Analysis*, Phys. Rev. Lett. **89**, 283202 (2002).

[26] A. Mosk, S. Kraft, and M. Mudrich, *Mixture of ultracold lithium and cesium atoms in an optical dipole trap*, Appl. Phys. B **73**, 791 (2001).

[27] M. Mudrich *et al.*, *Sympathetic Cooling with Two Atomic Species in an Optical Trap*, Phys. Rev. Lett. **88**, 253001 (2002).

[28] R. Scheunemann, F. S. Cataliotti, T. W. Hnsch, and M. Weitz, *Resolving and Addressing Atoms in Individual Sites of a CO_2-Laser Optical Lattice*, Phys. Rev. A **62**, 051801 (R) (2000).

[29] P. F. Griffin, K. J. Weatherill, S. G. MacLeod, R. M. Potvliege, and C. S. Adams, *Spatially selective loading of an optical lattice by light-shift engineering using an auxiliary laser field*, (2005), physics/0504113.

[30] K. B. MacAdam, A. Steinbach, and C. Wieman, *A narrow-band tunable diode-laser system with grating feedback, and a saturated absorption spectrometer for Cs and Rb*, Am. J. Phys. **60**, 1098 (1992).

[31] L. Ricci *et al.*, *A Compact Grating-Stabilized Diode Laser System for Atomic Physics*, Opt. Comm. **117**, 541 (1995).

[32] A. S. Arnold, J. S. Wilson, and M. G. Boshier, *A simple extended-cavity diode laser*, Rev. Sci. Instrum. **69**, 1236 (1998).

[33] K. Lindquist, M. Stephens, and C. Wieman, *Experimental and theoretical study of the vapor-cell Zeeman optical trap*, Phys. Rev. A **46**, 4082 (1992).

[34] C. Ye, *Tunable external cavity diode lasers* (World Scientific, Singapore, 2004).

[35] W. Demtröder, *Laser Spectroscopy 3rd Ed.* (Springer, 2003).

[36] Y.-C. Chen, W.-B. Lin, H.-C. Hsue, L. Hsu, and I. A. Yu, *Effect of trapping laser linewidth on the atom number in a magneto-optical trap*, Chinese Journal of Physics **38**, 920 (2000).

[37] C. E. Wieman and L. Hollberg, *Using diode lasers for atomic physics*, Rev. Sci. Instrum. **62**, 1 (1991).

[38] G. Brooker, *Modern Classical Optics* (Oxford University Press, 2003).

[39] Digi–Key Corporation 701 Brooks Avenue South Thief River Falls, MN 56701 USA.

[40] J. S. Rigden, *Hydrogen: The Essential Element* (Harvard University Press, 2003), pp. 209.

[41] K. L. Corwin, Z.-T. Lu, C. F. Hand, R. J. Epstein, and C. E. Wieman, *Frequency-Stabilized Diode Laser with the Zeeman Shift in an Atomic Vapor*, Appl. Optics. **37**, 3295 (1998).

[42] C. P. Pearman *et al.*, *Polarization Spectroscopy of a Closed Atomic Transition: Applications to Laser Frequency Locking*, J. Phys. B: At. Mol. Opt. Phys. **35**, 5141 (2002).

[43] G. P. T. Lancaster, R. S. Conroy, M. A. Clifford, J. Arlt, and K. Dholakia, *A polarisation spectrometer locked diode laser for trapping cold atoms*, Opt. Comm. **170**, 79 (1999).

[44] C. Pearman, *Ultra Stable Lasers for Atom Cooling*, Master's thesis, Durham University, 2002.

[45] M. L. Harris *et al.*, *Polarization spectroscopy in rubidium and cesium: experiment and theory*, submitted to Phys. Rev. A, 2005.

[46] D. Hansen and A. Hemmerich, *Doppler-free spectroscopy of metastable calcium in a discharge heat pipe*, Phys. Rev. A **72**, 022502 (2005).

[47] G. D. Rovera, G. Santarelli, and A. Clairon, *A laser diode system stabilized on the Caesium D_2 line*, Rev. Sci. Instrum. **65**, 1502 (1994).

[48] W. Ketterle, D. S. Durfee, and D. Stamper-Kurn, *Proceedings of the International School of Physics Enrico Fermi Course CXL* (IOS Press, Amsterdam, 1999), chap. Making, probing and understanding Bose–Einstein condensates, p. 67, cond-mat/9904034.

[49] M. D. Barrett, J. A. Sauer, and M. S. Chapman, *All-Optical Formation of an Atomic Bose–Einstein Condensate,* Phys. Rev. Lett. **87**, 010404 (2001).

[50] S. R. Granade, M. E. Gehm, K. M. O'Hara, and J. E. Thomas, *All-optical production of a degenerate Fermi gas,* Phys. Rev. Lett. **88**, 120405 (2002).

[51] R. Folman, P. Krüger, J. Schmiedmayer, J. Denschlag, and C. Henkel, *Microscopic Atom Optics: From Wires To An Atom Chip,* Adv. At. Mol. Opt. Phys. **48**, 263 (2002).

[52] N. Harris, *Modern Vacuum Pactice* (McGraw Hill, London, 1989), p. 181.

[53] N. Harris, *Modern Vacuum Pactice* (McGraw Hill, London, 1989), p. 184.

[54] E. A. Cornell, J. R. Ensher, and C. E. Wieman, *Proceedings of the International School of Physics Enrico Fermi Course CXL* (IOS Press, Amsterdam, 1999), chap. Experiments in Dilute atomic Bose–Einstein condensation, p. 15, cond-mat/9903109.

[55] C. Damerow and W. Erley, *A simple and versatile ultrahigh vacuum leak-tight infrared window assembly,* J. Vac. Sci. Technol. A **5**, 2974 (1987).

[56] C. H. Muller, M. W. Barrett, and D. D. Lowenthal, *High-temperature window seals for VUV experiments,* Rev. Sci. Instrum. **59**, 1425 (1988).

[57] H. Saeki, J. Ikeda, and H. Ishimaru, *Optical Window Sealed With Indium for Ultrahigh Vacuum,* Vacuum **6**, 563 (1989).

[58] A. Nobel and M. Kasevich, *UHV optical window seal to conflat knife edge,* Rev. Sci. Instrum. **65**, 3042 (1994).

[59] T. J. Manuccia, J. R. Peele, and C. E. Goesling, *High temperature ultra-high vacuum infrared window seal,* Rev. Sci. Instrum. **52**, 1857 (1981).

[60] S. G. Cox, P. F. Griffin, C. S. Adams, D. DeMille, and E. Riis, *Reusable ultrahigh vacuum viewport bakeable to 240° C,* Rev. Sci. Instrum. **74**, 3185 (2003).

[61] ALANOD Ltd., Chippenham Drive, Kingston, Milton Keynes, MK10 0AN UK.

[62] CMT Engineering, PO Box 36, Corngreaves Rd, Cradley Heath, West Midlands B64 7DQ, UK.

[63] IMS UK, Russell Road, Southport, Merseyside PR9 7SB, UK.

[64] M. Misakian, *Equations for the Magnetic Field Produced by One or More Rectangular Loops of Wire in the Same Plane*, J. Res. Natl. Inst. Stand. Technol. **105**, 557 (2000).

[65] W. M. Frix, G. G. Karady, and B. A. Venetz, *Comparison of Calibration Systems for Magnetic Field Measurement Equipment*, IEEE Trans. Power Delivery **9**, 100 (1994).

[66] H. J. Lewandowski, D. M. Harber, D. L. Whitaker, and E. A. Cornell, *Simplifed System for Creating a Bose-Einstein Condensate*, unpublished.

[67] D. J. Wineland, R. E. Drullinger, and F. L. Walls, *Radiation-Pressure Cooling of Bound Resonant Absorbers*, Phys. Rev. Lett. **40**, 1639 (1978).

[68] W. Neuhauser, M. Hohenstatt, P. Toschek, and H. Dehmelt, *Optical-Sideband Cooling of Visible Atom Cloud Confined in Parabolic Well*, Phys. Rev. Lett. **41**, 233 (1978).

[69] T. W. Hänsch and A. L. Schawlow, *Cooling of Gases by Laser Radiation*, Opt. Commun. **13**, 68 (1975).

[70] M. Gajda and J. Mostowski, *Three–dimensional theory of the magneto-optical trap: Doppler cooling in the low-intensity limit*, Phys. Rev. A **49**, 4864 (1994).

[71] H. J. Metcalf and P. van der Straten, *Laser Cooling and Trapping* (Springer, 1999).

[72] P. D. Lett *et al.*, *Observation of atoms laser cooled below the Doppler limit*, Phys. Rev. Lett. **61**, 169 (1988).

[73] J. Dalibard and C. Cohen-Tannoudji, *Laser cooling below the Doppler limit by polarization gradients: simple theoretical models*, J. Opt. Soc. Am. B **6**, 2023 (1989).

[74] P. J. Ungar, D. S. Weiss, E. Riis, and S. Chu, *Optical molasses and multilevel atoms: theory*, J. Opt. Soc. Am. B **6**, 2058 (1989).

[75] P. D. Lett *et al.*, *Optical molasses*, J. Opt. Soc. Am. B **6**, 2084 (1989).

[76] E. L. Raab, M. Prentiss, A. Cable, S. Chu, and D. E. Pritchard, *Trapping of Neutral Sodium Atoms with Radiation Pressure*, Phys. Rev. Lett. **59**, 2631 (1987).

[77] G. Orwell, *Animal Farm* (Harcourt Brace & Company, 1946).

[78] C. S. Adams, H. J. Lee, N. Davidson, M. Kasevich, and S. Chu, *Evaporative Cooling in a Crossed Dipole Trap*, Phys. Rev. Lett. **74**, 3577 (1995).

[79] J. Fortagh, A. Grossmann, T. W. Hänsch, and C. Zimmermann, *Fast loading of a magneto-optical trap from a pulsed thermal source*, J. Appl. Phys. **84**, 6499 (1988).

[80] U. D. Rapol, A. Wasan, and V. Natarajan, *Loading of a Rb magneto-optic trap from a getter source*, Phys. Rev. A **64**, 023402 (2001).

[81] C. Monroe, W. Swann, H. Robinson, and C. Wieman, *Very Cold Trapped Atoms in a Vapor Cell*, Phys. Rev. Lett **65**, 1571 (1990).

[82] A. S. Arnold and P. J. Manson, *Atomic density and temperature distributions in magneto-optical traps*, J. Opt. Soc. Am. B **17**, 497 (2000).

[83] C. J. Cooper *et al.*, *The temperature of atoms in a magneto–optical trap*, Europhys. Lett. **28**, 397 (1994).

[84] H. J. Davies, *An optically guided atomic fountain*, PhD thesis, University of Durham, 1999.

[85] M. Bass, *Physical Processes in Laser-Materials Interactions* (Plenium Press, New York, 1983), chap. CO_2 Laser Materials Processing, p. 143.

[86] A. G. Grigoryants, *Basics of Laser Material Processing* (Mir Publishers, Moscow, 1994).

[87] M. Bass, *Physical Processes in Laser-Materials Interactions* (Plenium Press, New York, 1983), chap. Laser Heating of Solids, p. 77.

[88] P. F. Griffin, K. J. Weatherill, and C. S. Adams, *Fast switching of alkali atom dispensers using laser induced heating*, Rev. Sci. Instrum. **76**, 093102 (2005).

[89] P. Horowitz and W. Hill, *The Art of Electronics, 2nd ed.* (Cambridge Uni. Press, Cambridge, 1993).

[90] K. Singer, S. Jochim, M. Mudrich, A. Mosk, and M. Weidemüller, *Low-cost mechanical shutter for light beams*, Rev. Sci. Instrum. **73**, 4402 (2002).

[91] M. A. Joffe, W. Ketterle, A. Martin, and D. E. Pritchard, *Transverse cooling and deflection of an atomic beam inside a Zeeman slower*, J. Opt. Soc. Am. B **10**, 2257 (1993).

[92] J. Jackson, *Classical Electrodynamics 3rd Ed.* (Wiley, 1999), pp. 165–167.

[93] R. M. Potvliege and R. Shakeshaft, *Atoms in Intense Fields* (Academic Press, San Diego, 1992), chap. Nonperturbative treatment of multiphoton ionization within the Floquet framework, p. 373.

[94] R. N. Zare, *Angular Momentum* (John Wiley & Sons, Inc., 1988), p. 180.

[95] D. A. Steck, *Rubidium 87 D Line Data*, revision 1.6. Source – http://steck.us/alkalidata, 2003.

[96] D. Suter, *The Physics of Laser–Atom Interactions* (Cambridge University Press, 1997), p. 159.

[97] R. Loudon, *The Quantum Theory of Light* (Oxford University Press, 2001), p. 171.

[98] R. Kurucz and B. Bell, *1995 Atomic Line Data*, Kurucz CD-ROM No. 23.

[99] B. Warner, *Atomic Oscillator Strengths - III, Alkali-Like Spectra*, Mon. Not. R. Astr. Soc **139**, 115 (1968).

[100] E. Caliebe and K. Niemax, *Oscillator strengths of the principal series lines of Rb*, J. Phys. B: At. Mol. Opt. Phys. **12**, L45 (1979).

[101] C. E. Moore, *Atomic energy levels as derived from the analyses of optical spectra*National Bureau of Standards Reference Data Series (U.S. Dept. of Commerce, Washington, 1958).

[102] S. Magnier and M. Aubert-Frécon, *Static Dipole Polarizabilities for Various Electronic States of Alkali Atoms*, J. Quant. Spect. Rad. Trans. **75**, 121 (2002).

[103] R. W. Schmieder, *Matrix Elements of the Quadratic Start Effect on Atoms with Hyperfine Structure*, Am. J. Phys. **40**, 297 (1972).

[104] C. Schwarz, *Theory of Hyperfine Structure*, Phys. Rev. **97**, 380 (1955).

[105] E. Arimondo, M. Inguscio, and P. Violino, *Experimental determinations of the hyperine structure in the alkali atoms*, Rev. Mod. Phys. **49**, 31 (1977).

[106] K. M. O'Hara *et al.*, *Ultrastable CO_2 Laser Trapping of Lithium Fermions*, Phys. Rev. Lett. **82**, 4204 (1999).

[107] J. E. Thomas, M. J. Kelly, J.-P. Monchalin, N. A. Kurnit, and A. Javan, *Stable CO_2 and N_2O laser design*, Rev. Sci. Instrum. **51**, 240 (1980).

[108] T. A. Savard, K. M. O'Hara, and J. E. Thomas, *Laser–noise–induced heating in far–off resonance optical traps*, Phys. Rev. A **56**, R1095 (1997).

[109] M. E. Gehm, K. M. O'Hara, T. A. Savard, and J. E. Thomas, *Dynamics of noise-induced heating in atom traps*, Phys. Rev. A **58**, 3914 (1998).

[110] K. M. O'Hara, *Optical Trapping and Evaporative Cooling of Fermionic Atoms*, PhD thesis, Duke University, 2000.

[111] M. E. Gehm, *Preparation of an Optically-Trapped Degenerate Fermi Gas of ^6Li - Finding the Route to Degeneracy*, PhD thesis, Duke University, 2003.

[112] A. E. Siegman, *Lasers* (University Science Books, California, 1986).

[113] P. Ahmadi, V. Ramareddy, and G. S. Summy, *Multiple micro-optical atom traps with a spherically aberrated laser beam*, New J. Phys. **7**, 4 (2005).

[114] S. R. Granade, *Preparation of an Optically-Trapped Degenerate Fermi Gas of ^6Li - Characterization of Degeneracy*, PhD thesis, Duke University, 2002.

[115] S. Friebel, R. Scheunemann, J.Walz, T. Hänsch, and M.Weitz, *Laser cooling in a CO_2-laser optical lattice*, Appl. Phys. B **67**, 699 (1998).

[116] D. Boiron *et al.*, *Cold and dense cesium clouds in far–detuned dipole traps*, Phys. Rev. A **57**, R4106 (1998).

[117] H. Engler, T. Weber, M. Mudrich, R. Grimm, and M. Weidemüller, *Very long storage times and evaporative cooling of cesium atoms in a quasielectrostatic dipole trap*, Phys. Rev. A **62**, 031402(R) (2000).

[118] M.-S. Chang, Q. Qin, W. Zhang, L. You, and M. S. Chapman, *Coherent spinor dynamics in a spin-1 Bose condensate*, (2005), cond-mat/0509341.

[119] T. Kinoshita, T. Wenger, and D. S. Weiss, *All-optical Bose-Einstein condensation using a compressible crossed dipole trap*, Phys. Rev. A **71**, 011602(R) (2005).

[120] J. Braat, *Analytical expressions for the wave-front aberration coefficients of a tilted plane-parallel plate*, Appl. Opt. **36**, 8459 (1997).

[121] Downloaded from `http://www.lambdares.com/products/oslo`.

[122] T. Weber, J. Herbig, M. Mark, H.-C. Nägerl, and R. Grimm, *Bose–Einstein Condensation of Cesium*, Science **299**, 232 (2003).

[123] W. Alt, *An objective lens for efficient fluorescence detection of single atoms*, Optik **113**, 142 (2002).

[124] C. S. Adams, S. G. Cox, E. Riis, and A. S. Arnold, *Laser cooling of calcium in a golden ratio quasi–electrostatic lattice*, J. Phys. B: At. Mol. Opt. Phys. **36**, 1933 (2003).

[125] R. M. Potvliege and R. Shakeshaft, *Nonperturbative calculation of partial differential rates for multiphoton ionization of a hydrogen atom in a strong laser field*, Phys. Rev. A **38**, 1098 (1998).